

## Separating glacial isostatic adjustment and ice-mass change signals in Antarctica using satellite data

Didova, Olga

**DOI**

[10.4233/uuid:58d2f768-20c2-48ea-9b54-efb94611cda6](https://doi.org/10.4233/uuid:58d2f768-20c2-48ea-9b54-efb94611cda6)

**Publication date**

2017

**Document Version**

Final published version

**Citation (APA)**

Didova, O. (2017). *Separating glacial isostatic adjustment and ice-mass change signals in Antarctica using satellite data*. [Dissertation (TU Delft), Delft University of Technology].  
<https://doi.org/10.4233/uuid:58d2f768-20c2-48ea-9b54-efb94611cda6>

**Important note**

To cite this publication, please use the final published version (if applicable).  
Please check the document version above.

**Copyright**

Other than for strictly personal use, it is not permitted to download, forward or distribute the text or part of it, without the consent of the author(s) and/or copyright holder(s), unless the work is under an open content license such as Creative Commons.

**Takedown policy**

Please contact us and provide details if you believe this document breaches copyrights.  
We will remove access to the work immediately and investigate your claim.

**SEPARATING GLACIAL ISOSTATIC ADJUSTMENT  
AND ICE-MASS CHANGE SIGNALS IN  
ANTARCTICA USING SATELLITE DATA**



# **SEPARATING GLACIAL ISOSTATIC ADJUSTMENT AND ICE-MASS CHANGE SIGNALS IN ANTARCTICA USING SATELLITE DATA**

## **Proefschrift**

ter verkrijging van de graad van doctor  
aan de Technische Universiteit Delft,  
op gezag van de Rector Magnificus prof. ir. K.C.A.M. Luyben,  
voorzitter van het College voor Promoties,  
in het openbaar te verdedigen op donderdag 7 december 2017 om 12:30 uur

door

**Olga Andriiwna Didova**

Master of Science in Geodesy and Geoinformation,  
University of Bonn, Germany  
geboren te Dnipropetrovsk, Ukraine.

This dissertation has been approved by the

promotor: Prof. Dr.-Ing. habil. R. Klees

Composition of the doctoral committee:

Rector Magnificus, chairman  
Prof. Dr.-Ing. habil. R. Klees, Delft University of Technology

*Independent members:*

Prof. Dr. ir. R. Hanssen, Delft University of Technology  
Prof. Dr. M. R. van den Broeke, Universiteit Utrecht  
Prof. Dr.-Ing. J. Kusche, Universität Bonn  
Prof. Dr.-Ing. M. Horwath, Technische Universität Dresden  
Prof. Dr. L. L. A. Vermeersen, Delft University of Technology, reserve member

*Other members:*

Dr. B. C. Gunter, Georgia Institute of Technology  
Dr. R. E. M. Riva, Delft University of Technology



Dr. B. C. Gunter from Georgia Institute of Technology, has as supervisor, contributed significantly to the preparation of this dissertation.

*Keywords:* GIA, GRACE, Antarctica, ice-mass changes, time-varying trend, patch approach, ICESat, SMB

*Printed by:* Optima Grafische Communicatie, Rotterdam

*Front & Back:* Antarctic patches. Design by N. Vtyurina.

Copyright © 2017 by O. Didova

ISBN 978-94-6361-039-1

An electronic version of this dissertation is available at

<http://repository.tudelft.nl/>.

*In memory, respect, and love of my dad and my grandmom*



# CONTENTS

<b>Summary</b>	<b>xi</b>
<b>Samenvatting</b>	<b>xv</b>
<b>1 Introduction</b>	<b>1</b>
1.1 Background and motivation . . . . .	1
1.2 Objectives . . . . .	2
1.3 Outline . . . . .	4
1.4 Non-public data sources . . . . .	5
<b>2 Empirical pointwise approach</b>	<b>7</b>
2.1 Introduction . . . . .	7
2.2 Methodology . . . . .	8
2.3 Data Sets . . . . .	9
2.3.1 Gravimetry . . . . .	9
2.3.2 Altimetry . . . . .	11
2.3.3 Climate data . . . . .	16
2.3.4 Vertical site-displacements . . . . .	19
2.4 GIA Bias Correction . . . . .	21
2.5 Combination results . . . . .	23
2.5.1 Uncertainty analysis . . . . .	25
2.5.2 Comparisons with GPS ground stations . . . . .	27
2.5.3 Discussion . . . . .	29
2.6 Conclusions . . . . .	34
<b>3 Empirical adjustment approach</b>	<b>37</b>
3.1 Introduction . . . . .	37
3.2 Data sets . . . . .	40
3.2.1 Gravimetry . . . . .	40
3.2.2 Altimetry . . . . .	40
3.2.3 Climate data . . . . .	41
3.2.4 GPS . . . . .	41
3.3 Methodology . . . . .	41
3.3.1 Patch approach . . . . .	42
3.3.2 Patch definition . . . . .	48
3.3.3 Dynamic patch approach . . . . .	52

3.4	Results . . . . .	55
3.4.1	GIA estimates . . . . .	55
3.4.2	Ice-mass change estimates. . . . .	57
3.4.3	Combination results . . . . .	61
3.4.4	Discussion . . . . .	68
3.5	Conclusions. . . . .	71
<b>4</b>	<b>Stochastic approach for time-series analysis</b>	<b>73</b>
4.1	Introduction . . . . .	73
4.2	Methodology . . . . .	74
4.2.1	Trend modelling . . . . .	74
4.2.2	State space model . . . . .	75
4.2.3	Kalman filter and smoother . . . . .	76
4.2.4	Estimation of hyperparameters . . . . .	77
4.2.5	GPS . . . . .	83
4.2.6	Summary of the developed framework. . . . .	86
4.3	Application to real data . . . . .	86
4.3.1	Data . . . . .	86
4.3.2	Results . . . . .	88
4.4	Conclusions. . . . .	94
<b>5</b>	<b>Comparing GRACE-, SMB-, and GPS-derived time-varying rates in Antarctica</b>	<b>97</b>
5.1	Introduction . . . . .	97
5.2	Data and Methodology . . . . .	98
5.3	Results . . . . .	101
5.3.1	GRACE - SMB . . . . .	101
5.3.2	GRACE - SMB - GPS . . . . .	104
5.4	Discussion . . . . .	118
5.4.1	GRACE - SMB . . . . .	118
5.4.2	GRACE - SMB - GPS . . . . .	121
5.5	Conclusions. . . . .	121
<b>6</b>	<b>Conclusions and recommendations</b>	<b>123</b>
6.1	Conclusions. . . . .	123
6.2	Recommendations . . . . .	125
	<b>References</b>	<b>129</b>
<b>A</b>	<b>Treatment of coloured noise in GPS time series</b>	<b>139</b>
A.1	Introduction . . . . .	139
A.2	ARMA model . . . . .	140
A.3	Generating $\frac{1}{f^\alpha}$ . . . . .	140
A.4	Detecting an appropriate order for ARMA( $p, q$ ) . . . . .	141
A.5	Random walk noise and ARMA( $p, q$ ) . . . . .	142
A.6	Flicker noise and ARMA( $p, q$ ) . . . . .	143
A.7	Discussion . . . . .	144

---

<b>Curriculum Vitæ</b>	<b>145</b>
<b>List of Publications</b>	<b>147</b>



# SUMMARY

The main goal of this thesis involves the development of a refined methodology to separate the mass change signals associated with glacial isostatic adjustment (GIA) from those of surface ice/firn by exploiting the strengths of independent data sets, such as those from gravimetry, altimetry, climate data, and others. To achieve this, various research efforts were conducted addressing specific aspects of the methodology and subsequent data processing. This led to a number of new contributions to the topic, summarized below.

## **Refining an empirical approach that simultaneously estimates Antarctic mass balance and GIA through the combination of satellite gravity and altimetry data by incorporating climate data.**

Antarctic ice mass loss estimates are contaminated by large uncertainties associated with uncertainties in existing GIA models. The impact of the ice loss on the global climate cycle is substantial, as the resulting change in sea level could have global environmental and societal consequences. The proposed combination approach simultaneously estimates Antarctic mass balance and GIA through the combination of satellite gravity, altimetry and climate data. The methodology improves upon earlier studies by including a range of reprocessed and extended data sets, incorporating a Regional Atmospheric Climate Model (RACMO2.1) and accompanying firn densification model, as well as by calibrating the results to a low-precipitation zone in East Antarctica. Through formal error propagation techniques, the uncertainties for both the GIA and ice mass change estimates are obtained. The empirically derived GIA models are compared to a set of Antarctic GNSS (Global Navigation Satellite System) site displacements, as well as to traditionally derived Antarctic GIA models. The main result is an empirically derived regional Antarctic GIA model with corresponding uncertainties, which suggests the presence of strong uplift in the Amundsen Sea and Philippi/Denman sectors, as well as subsidence in large parts of East Antarctica.

## **Improving the gravity data post-processing and incorporating them into the combination approach to separate the GIA signal from that of changes in ice mass by exploiting the strengths of independent datasets.**

The limited horizontal resolution represents a major challenge when combining Gravity Recovery and Climate Experiment (GRACE) data with data that feature higher spatial resolution, such as ICESat (Ice Cloud and land Elevation Satellite) altimeter and climate data. A so-called 'dynamic patch approach' is developed to consistently combine GRACE data with high resolution data from ICESat and RACMO. Independent GPS observations are used to define the spatial pattern of estimated present-day GIA. The spatial resolution of estimated ice-mass changes is determined using an ICESat-RACMO2.3 combination. To solve for GIA and ice-mass changes, a weighted least-squares adjustment is applied while taking into ac-

count the full noise covariance information of GRACE data, as well as the variances of other datasets involved in the combination, without using any additional constraints. The results suggest the capability of the developed approach to retrieve the complex spatial pattern of present-day GIA, such as a pronounced subsidence in the proximity of the Kamb Ice Stream. Furthermore, the suggested method recovers statistically significant high-resolution maps of mass loss for West Antarctica ( $-98 \pm 5$  Gt/yr) and the entire Antarctic Ice Sheet ( $-143 \pm 36$  Gt/yr) for the ICE-Sat mission period, from February 2003 to October 2009.

#### **Estimating time-variable rates from geodetic time series.**

Motivated by the 'stochastic nature' of Antarctic ice sheet variability, an approach for trend analysis from geodetic time series is presented which allows for physically natural variations of the various signal constituents over time. In other words, instead of using the traditional deterministic approach where seasonal signals are estimated with fixed amplitudes and phases, and the trend is assumed to be linear, these signals are modeled stochastically. To accomplish this, state-space models are defined and solved through the use of a Kalman filter. Since the appropriate choice of the noise parameters is at the heart of the proposed approach, a robust method for their estimation is developed. In this context, the use of inequality constraints is tested by directly verifying whether they are supported by the data. The suggested technique for time series analysis is expanded to classify and handle time-correlated observational noise within the state-space framework. The performance of the method is demonstrated using GRACE and GPS data at the CAS1 station located in East Antarctica and compared to commonly used least square adjustment. The results suggest that the outlined technique allows for more reliable trend estimates as well as for more physically valuable interpretations while validating independent observing systems.

#### **Deriving dynamically-induced mass changes through a validation of GRACE- and SMB-based time-varying trends at the level of drainage systems in Antarctica.**

The reliability of SMB (Surface Mass Balance) is crucial when used within space-based methods to derive Antarctic ice-mass changes. An accurate knowledge of temporal variations in SMB is especially important for correcting GPS-derived vertical displacement rates for elastic deformation before using GPS to constrain Antarctic GIA. To explore this, SMB modeled by RACMO2.3 is validated against GRACE observations over the entire AIS, integrated over drainage systems. To ensure a fair comparison between SMB and GRACE data in terms of spatial resolution, the 'dynamic patch approach' is again utilized. The stochastic approach for time-series analysis is then applied to model trends along with known periodicities from SMB and GRACE data at the level of drainage systems. This analysis reveals an excellent agreement (mean correlation of 0.7) between GRACE- and SMB-derived rates for 70% of the Antarctic drainage systems, thus highlighting the reliability of the modeled temporal variations in SMB from RACMO2.3. The difference between the GIA-corrected GRACE time-varying trends and those derived from SMB is attributed to ice dynamics yielding basin-wise estimates for dynamically-induced mass changes. Over the time period from February 2003 to December 2011, the

mean ice dynamic trend of  $-89 \pm 24$  Gt/yr is estimated.

### **Comparing GRACE-, SMB-, and GPS-derived time-varying rates in Antarctica.**

GPS measurements represent an independent and valuable constraint for GIA provided that it has been accounted for the elastic signal due to contemporaneous mass change. Therefore, accurately estimating elastic deformation rates is crucial for determining more accurate GIA, which in turn will improve ice-mass change estimates over Antarctica. To investigate the potential of GRACE data for the purpose of correcting GPS from the elastic uplift, an inter-comparison of time-varying rates derived from GRACE, SMB, and GPS data is performed at the locations of ten permanent GPS stations in Antarctica. For this, the patch approach and the stochastic approach for time-series analysis are utilized. At the locations of analyzed GPS stations, the comparison of GRACE- versus SMB-derived time-varying rates demonstrates the capability of GRACE data to resolve temporal variations in Antarctic SMB and increases confidence in RACMO-modeled fluctuations. The evolution of vertical deformations derived from GPS, GRACE, and SMB reveals a good agreement for five out of ten analyzed GPS stations, although the conclusions regarding the secular part of time-varying trend remain challenging. Nevertheless, the analysis of the derived temporal variations leads to two main results: it demonstrates the potential of GRACE data for the purpose of correcting GPS for the non-linear variations in elastic uplift, and it provides a better understanding of the limitations of GPS data as an explicit constraint for Antarctic GIA.

### **Principal innovations**

The primary contributions of this thesis are:

1. An approach to incorporate climate data into the combination of satellite gravity and altimetry data to simultaneously estimate Antarctic mass balance and present-day GIA (Ch. 2).
2. A method to cope with imprecisely known potential bias contributors to the derived Antarctic GIA signal (Ch. 2).
3. An approach to derive GIA and ice mass change in Antarctica with unprecedented high spatial resolution (Ch. 3).
4. An approach to improve the chance of finding the global minimum in the context of deriving time-varying trends from geodetic time series (Ch. 4).
5. Application of the derived time-varying trends to validate geodetic time series (Ch. 5).
6. An approach to derive dynamically-induced mass changes with corresponding uncertainties at the level of drainage systems in Antarctica (Ch. 5).



# SAMENVATTING

Het hoofddoel van dit proefschrift is om een verbeterde methode te ontwikkelen waarmee de massaveranderingssignalen geassocieerd met postglaciale ophefing (GIA) gescheiden kan worden van signalen afkomstig van oppervlakte-ijs en firn, door gebruik te maken van de individuele sterktes van onafhankelijke datasets, waaronder gravimetrie, altimetrie en data van klimaatmodellen. Om dit te bereiken zijn diverse specifieke aspecten van de methodologie en de bijbehorende dataverwerking onderzocht. Dit heeft geleid tot een aantal nieuwe inzichten over dit onderwerp, die hieronder zijn samengevat.

## **Het verbeteren van de empirische methode om tegelijkertijd zowel de massabalans als GIA op Antarctica te schatten uit gravimetrie- en altimetriedata en data van klimaatmodellen.**

Schattingen van het verlies van ijsmassa op Antarctica zijn onnauwkeurig, omdat bestaande GIA-modellen nog steeds grote onzekerheden bevatten. De impact van het verlies van ijsmassa op de wereldwijde klimaatcyclus is groot, omdat de bijbehorende zeespiegelveranderingen een grote impact hebben op het milieu en de maatschappij. De voorgestelde combinatie-methode schat tegelijkertijd de massabalans en GIA uit satellietzwaartekrachtmetingen, altimetrie en klimaatdata. De methode gaat verder dan eerdere studies door het toevoegen van een reeks verbeterde en uitgebreide datasets, het gebruik van regionaal klimaatmodel RACMO2.1 en bijbehorend firnverdikkingsmodel, en door het kalibreren van de resultaten in een regio met weinig neerslag in Oost-Antarctica. Met behulp van formele foutpropagatie zijn betrouwbaarheidsintervallen voor de GIA- en ijsmassaschattingen verkregen. De empirisch bepaalde GIA-modellen zijn vergeleken met door GNSS (Global Navigation Satellite System) gemeten bewegingen, en met bestaande GIA-modellen van Antarctica. Met deze methode is een empirisch regionaal GIA-model van Antarctica met bijbehorende onzekerheden verkregen. Dit model geeft aan dat de vaste aarde onder de Amundsenzee en Philippinen Denman-sectoren snel omhoogkomt en dat de bodem in grote delen van Oost-Antarctica verzakt.

## **Verbeteringen in de verwerking van zwaartekrachtsdata en het toepassen van deze data in de combinatie-aanpak om het GIA-signaal te scheiden van het massasignaal met gebruik van de individuele kwaliteiten van de onafhankelijke datasets.**

Het is lastig om GRACE-data (Gravity Recovery And Climate Experiment) met zijn beperkte horizontale resolutie te combineren met hogeresolutiedata, zoals ICESat-altimetriedata (Ice Cloud en land Elevation Satellite) en data van klimaatmodellen. De zogenaamde 'dynamic patch approach' is ontwikkeld om data van GRACE op een consistente manier te combineren met hogeresolutiedata van ICESat en RACMO. Onafhankelijke GPS-metingen zijn gebruikt om het ruimtelijke patroon te

bepalen van het geschatte hedendaagse GIA-signaal. De resolutie van de geschatte ijsmassaveranderingen is bepaald uit de combinatie van ICESat- en RACMO2.3-data. Om tegelijkertijd GIA en ijsmassaveranderingen schatten is de gewogen kleinste-kwadratenschatter toegepast, waardoor de volledige covariantie-matrix van de GRACE-residuen en de variantie van de andere datasets zonder extra beperkingen kunnen worden meegenomen. De resultaten suggereren dat de methode in staat is om het complexe GIA-patroon te bepalen, waaronder de opvallende bodemdaling vlak bij Kamb Ice Stream. Ook produceert de voorgestelde methode over de gehele ICESat-missieperiode (februari 2003-oktober 2009) statistisch significante hogeresolutiekaarten van het massaverlies voor West-Antarctica ( $-98 \pm 5$  Gt/j) en voor heel Antarctica ( $-143 \pm 36$  Gt/j).

#### **Het schatten van tijdsvariërende snelheden uit geodetische tijdreeksen.**

Gemotiveerd door het stochastische karakter van de variabiliteit van de Antarctische ijskap, wordt een aanpak voor het schatten van trends uit geodetische data voorgesteld waarbij de verschillende signaalcomponenten kunnen variëren in de tijd. Met andere woorden, de trend en cycli worden stochastisch verondersteld, in tegenstelling tot de deterministische benadering waarbij de trend linear is en de seizoenscycli een constante amplitude en fase hebben. Om dit te doen zijn state-space-modellen gedefinieerd, die met een Kalman-filter worden opgelost. Omdat de juiste keuze van de ruis-parameters cruciaal is voor deze aanpak, is een robuuste methode ontwikkeld om deze parameters te schatten. De ongelijkheids-eis is getest door te controleren of deze door meetgegevens wordt ondersteund. De methode is uitgebreid zodat tijdsgecorrleerde observatieruis geanalyseerd en geschat kan worden. De methode is gebruikt om GRACE- en GPS-data op het CAS1-station in Oost-Antarctica te analyseren, en de resultaten zijn vergeleken met de traditionele kleinste-kwadraten-schattingen. De resultaten suggereren dat de state-space-methode betrouwbaardere trendschattingen produceert en fysisch consistentere interpretaties mogelijk maakt, waarmee onafhankelijke observatiesystemen gevalideerd kunnen worden.

#### **Bepaling van massaveranderingen veroorzaakt door ijsdynamica met behulp van tijdsvariërende trends in GRACE- en SMB-data op de schaal van individuele drainagebassins.**

Betrouwbaar SMB-modellen (Surface Mass Balance) zijn van groot belang om ijsmassaveranderingen in Antarctica te bepalen met behulp van ruimte-observaties. Accurate schattingen van tijdsvariëtes in de SMB zijn vooral belangrijk om GPS-metingen te corrigeren voor elastische deformatie voordat ze gebruikt kunnen worden om GIA op Antarctica te bepalen. Om dit te onderzoeken, is de SMB, gemodelleerd met RACMO2.3, gevalideerd met GRACE-metingen over zowel de gehele ijskap als voor elk afzonderlijk drainagebassin. Om een consistente vergelijking tussen de SMB en de GRACE-data in termen van resolutie te waarborgen, is de 'dynamic patch approach' ook hier toegepast. De stochastische benadering voor tijdreeksanalyse is toegepast voor elk drainagebassin op de modeltrends, samen met de bekende cycli in de SMB- en GRACE-data. De analyse laat een uitstekende overeenkomst zien (gemiddelde correlatie van 0.7) tussen de GRACE- en SMB-gebaseerde trends voor 70% van de drainagesystemen, wat de hoge betrouwbaar-

heid van de gemodelleerde SMB-variaties in RACMO2.3 aantoon. Het verschil tussen de GIA-gecorrigeerde tijdsvariërende GRACE-trends en de trends afgeleid uit de SMB kan worden toegeschreven aan de dynamische contributie, waarmee schattingen zijn verkregen voor dynamisch geïnduceerde massaveranderingen in elk basin. Over de periode van februari 2003 tot december 2011 is een gemiddelde trend in de ijsdynamica gelijk aan  $-89 \pm 24$  Gt/j geschat.

### **Een vergelijking tussen de tijdsvariërende trends in GRACE-, SMB- en GPS-data op Antarctica.**

Wanneer rekening gehouden wordt met elastische vervorming door hedendaagse massaveranderingen vormen GPS-metingen een onafhankelijke en waardevolle randvoorwaarde voor GIA-schattingen. Daarom is het nauwkeurig schatten van elastische deformatie van cruciaal belang voor het bepalen om het GIA-signaal. Met dit verkregen GIA-signaal kan vervolgens de schatting van de ijsmassaverandering op Antarctica kan worden verbeterd. Om het potentieel van GRACE-gegevens te onderzoeken om GPS voor elastische deformatie te corrigeren, is een vergelijking tussen tijdsvariërende snelheden, bepaald uit GRACE-, SMB- en GPS-data uitgevoerd ter hoogte van 10 permanente GPS-stations op Antarctica. Hiervoor zijn zowel de patchbenadering als het state-space-model gebruikt. Op de locaties van de GPS-stations toont de vergelijking tussen de GRACE- SMB-trends aan dat GRACE-data gebruikt kan worden om SMB-veranderingen op Antarctica te bepalen. De vergelijking verhoogt bovendien het vertrouwen in de RACMO2.3-modelresultaten. Voor vijf van de tien geanalyseerde GPS-stations laten de metingen van verticale landbewegingen met GRACE, GPS en de SMB een consistent beeld zien, hoewel de resultaten van het lineaire deel van de tijdvariabele trend nog steeds onduidelijk zijn. Desondanks leidt de analyse van de geschatte tijdsvariaties tot twee belangrijke conclusies: het toont het potentieel van GRACE-metingen om GPS-metingen te corrigeren voor tijdsvariërende elastische deformatie, en het geeft een beter inzicht in de limieten van het gebruik van GPS-gegevens om het GIA-signaal in Antarctica te bepalen.

### **Belangrijkste innovaties**

De belangrijkste innovaties van dit proefschrift zijn:

1. Een methode om data van klimaatmodellen mee te nemen bij het simultaan schatten van de ijsmassabalans en het GIA-signaal op Antarctica uit gravimetrie en altimetrie (hoofdstuk 2).
2. Een methode om om te gaan met de invloed van mogelijke afwijkingen, waarvan de grootte niet nauwkeurig is bepaald, op het geschatte GIA-signaal in Antarctica (hoofdstuk 2).
3. Een aanpak om het GIA-signaal en ijsmassaverandering in Antarctica te schatten met een ongekend hoge ruimtelijke resolutie (hoofdstuk 3).
4. Een methode om de kans te verhogen dat het globale minimum gevonden wordt in het kader van het afleiden van tijdsvariërende trends uit geodetische tijdreeksen (hoofdstuk 4).

5. Het toepassen van de afgeleide tijdsvariërende trends om geodetische tijdreeksen te valideren (hoofdstuk 5).
6. Een aanpak om massaveranderingen en bijbehorende betrouwbaarheidsintervallen af te leiden die het gevolg zijn van ijsdynamica op het niveau van individuele drainagesystemen in Antarctica (hoofdstuk 5).

# 1

## INTRODUCTION

### 1.1. BACKGROUND AND MOTIVATION

Rising global temperatures undoubtedly affect mass loss rates of Antarctica. The world's largest ice sheet contains enough ice to raise the world's ocean by ca. 57 m if completely melted (Lemke et al, 2007). Its mass contribution to sea-level rise is a subject of ongoing intense study (e.g., Chen et al, 2006; Rignot et al, 2008; Shepherd et al, 2012; Velicogna et al, 2014; Zwally et al, 2015; Martín-Español et al, 2016b). To understand the present-day response of the largest reservoir of fresh water on Earth to the changing climate, and to be able to make realistic projections for the future, is of great societal importance.

There are three main space-based methods currently used to derive Antarctic ice-mass changes: (i) repeated elevation measurements, (ii) the mass budget method, and (iii) repeated gravity measurements (Shepherd et al, 2012). Each of them has its advantages and disadvantages. Repeated elevation measurements are conducted by radar (e.g., EnviSat, Cryosat-2) or laser (ICESat) altimeters. The key challenge of this method is converting elevation changes into mass changes, as there are large uncertainties associated with the densities involved. The mass budget method compares difference between the surface mass balance (SMB) and ice discharge. The largest uncertainties of this method are associated with the models of SMB that are validated using sparse ice core data, with an inaccurate knowledge of ice depth, grounding line position, and firn depth correction. Repeated gravity measurements are conducted by the Gravity Recovery and Climate Experiment (GRACE) satellite mission. GRACE measures the inter-satellite ranges, from which mass changes have been inferred since its launch in 2002.

Although GRACE observations directly provide mass changes, they also have their limitations, one of which is a limited vertical resolution, i.e., they represent a sum of signals originating from different sources. For Antarctica, present-day ice-mass changes and glacial isostatic adjustment (GIA) are the main sources contributing to the total GRACE signal. GIA is the ongoing response of the solid-earth

to changing ice loads and should be removed from GRACE observations as accurately as possible prior to deriving ice-mass changes. Unfortunately, the spatial distribution as well as the magnitude of the GIA signal are still poorly known, representing the largest source of uncertainty for Antarctic ice-mass change estimates derived from GRACE (Velicogna and Wahr, 2006). Shepherd et al (2012) noted that this source of uncertainty could reach up to 130 Gt/yr (equivalent to 0.36 mm/yr in terms of global sea level rise), which emphasizes why improvements on either aspect (ice-mass changes or GIA) would help make sea-level projections more accurate.

A number of strategies have been developed to assess Antarctic GIA and are here arranged in four categories. First, forward modeling of GIA based on Antarctic ice load history and Earth properties (Peltier, 2004; Ivins and James, 2005). Second, forward modeling of GIA while constraining it using geodetic observations such as GPS (Whitehouse et al, 2012; Ivins et al, 2013; Peltier et al, 2015) or GRACE and GPS (Sasgen et al, 2013). Third, estimating GIA by using complementary geodetic observations while constraining it using forward models (e.g., Schoen et al, 2015; Zammit-Mangion et al, 2015; Martín-Español et al, 2016b). And finally, estimating GIA using complementary geodetic observations that are completely independent from forward-modeled GIA (Riva et al, 2009; Groh et al, 2012). Independency is a very important aspect as it allows forward-modeled and empirically estimated GIA to be validated, providing insights into the underlying geophysics.

While Wahr et al (2000) introduced the concept of deriving Antarctic GIA through the combination of altimetry and gravimetry, the first real-data implementation was achieved by Riva et al (2009). As a joint estimation problem, the corresponding ice mass change trend was simultaneously computed, demonstrating that the two processes could indeed be separated. While the results were encouraging, the study also highlighted the need for additional improvements to the methodology and data sets involved in order to improve our understanding of mass transport processes of Antarctica (both GIA and ice-mass changes). The main goal of this thesis is therefore developing a refined methodology to separate the GIA signal from that of changes in ice mass by exploiting the strengths of independent improved data sets, such as those from GRACE, ICESat, and others. Section 1.2 details the specific problems that are addressed in this thesis to achieve the main goal. Section 1.3 represents the structure of the thesis. Section 1.4 lists contributions to the work described in this thesis from collaborative researchers.

## 1.2. OBJECTIVES

The main objective of this thesis is to estimate GIA and ice-mass change rates in Antarctica along with realistic uncertainties using complementary geodetic observations. Note that GIA encompasses a range of observables including solid-earth deformation and deformation of the shape of the geoid (Farrell and Clark, 1976). In this thesis, rates of surface deformation associated with GIA are derived. As Riva et al (2009) laid the foundation for the current work, the principle behind their methodology is summarized here. It relies on the conservation of mass, and the fact that the rock and surface (ice/snow) layers have different density and thick-

ness change rates. The combination, therefore, was based on four datasets: two trends from satellite measurements (satellite gravimetry, altimetry) and two density maps (for rock and surface layer). The key limitation of this approach was the use of a static surface density map to convert ICESat-derived volume changes into mass, which did not account for variations in firn density and compaction. In the time since the work by [Riva et al \(2009\)](#) was carried out, additional data from a regional climate model RACMO2/ANT, representing improved knowledge of firn density and compaction rates across the Antarctic ice sheet were made available to the scientific community, yielding the first specific objective of this thesis:

*Objective 1: Incorporating firn density and compaction information into the gravimetry / altimetry combination approach.*

The primary results of an improved estimate of surface processes by incorporating RACMO data suggest a significant underestimation of the firn contribution in earlier work, and highlight new regions of strong uplift such as the Amundsen Sea sector ([Gunter et al, 2014](#)). The derived GIA consistently outperforms forward-modeled results when compared to GPS displacements, as was shown in [Gunter et al \(2014\)](#) and [Wolstencroft et al \(2015\)](#).

Altimetry and climate data, used to compute surface processes in the combination, are given as point values over Antarctica, whereas gravity data are usually represented by truncated spherical harmonics. That means that different data types involved in the combination approach exhibit different representations and spatial resolutions. To ensure that all data used in the combination were at the same spatial resolution and to help reduce GRACE-specific noise, a common 400 km half width Gaussian filter was applied to all components following [Riva et al \(2009\)](#). Since the smoothing operation redistributes the signal over the 400km radius, it undoubtedly attenuates the signal magnitude of the derived GIA and ice-mass changes. Although the total mass changes remained the same if integrated over the 400 km extended area, the spatial resolution of the derived GIA and ice-mass changes was considerably reduced potentially masking important geophysical features. This motivates the next objective of this thesis:

*Objective 2: Improving the spatial resolution of the estimated GIA and ice-mass change maps in Antarctica.*

As a result, the estimated GIA and ice-mass change signals exhibit considerably higher spatial resolution compared to previous estimates. Entirely new in the empirical GIA solution is a pronounced subsidence in the proximity of Kamb Ice Stream likely as a response to the Late Holocene loading related to stagnation and reactivation of ice streams in this area as reported in ([Nield et al, 2016](#)).

The empirical approach combines linear trends derived from gravimetry, altimetry, and climate data computed over the ICESat mission time that spans ca. 6.5 years. Besides the fact that a constant trend is a valid assumption for the derived GIA, only constant trends can be inferred from ICESat campaign measurements with high certainty. However, a constant trend assumption for ice-mass change rates, as it is usually made for Antarctica, might yield erroneous trend estimates, especially because of large inter-annual variations in the Antarctic climate

(Ligtenberg et al, 2012). Wouters et al (2013) found that the 'stochastic nature' of the Antarctic ice sheet weather strongly affects estimates of mass loss trends and, in particular, accelerations. Therefore, it is reasonable to apply a stochastic approach for analyzing Antarctic surface mass changes, which led to the next objective:

*Objective 3: Developing a robust tool for estimating time-varying trends from geodesic time series.*

The performance of the developed tool is demonstrated using GRACE and GPS data at the CAS1 station located in East Antarctica and compared to commonly used least-squares adjustment. The results suggest that potential changes in rates may yield significantly different trends when post-processed compared to the deterministic linear trend. Indeed, the longer the time series, the more deviations can be expected from the deterministic linear trend assumption as well as from the constant seasonal amplitudes and phases. Moreover, any change in the trend term reflects an acceleration, making the stochastic approach much more flexible than the deterministic one. It is therefore reasonable to consider signal as a stochastic process, particularly when analyzing climatological data. This is exactly what is done next when validating SMB (surface mass balance) modeled by a regional climate model RACMO2.3 with GRACE data:

*Objective 4: Deriving dynamically-induced mass changes through a validation of GRACE- and SMB-based time-varying trends at the level of drainage systems in Antarctica*

Since independent GPS measurements gain importance in constraining Antarctic GIA, they must be first accurately corrected for the elastic signal due to contemporaneous mass change. To investigate the potential of GRACE data for the purpose of correcting GPS for elastic uplift, an inter-comparison of time-varying rates derived from GRACE, SMB, and GPS data is performed at the locations of ten permanent GPS stations in Antarctica. This provides insight into the regional variations derived from the three independent techniques, the similarities between them, as well as their limitations, defining the final objective from this thesis:

*Objective 5: Comparing GRACE-, SMB-, and GPS-derived time-varying rates in Antarctica.*

### 1.3. OUTLINE

Chapters 2 - 5 detail the work undertaken for each of the objectives mentioned in Section 1.2. The work contained in Ch. 2 and Ch. 4 has been published in Gunter et al (2014) and Didova et al (2016), respectively. In Ch. 2, the approach developed by Riva et al (2009) is reformulated by incorporating RACMO data. For this, the combination of different data types takes place at each point defined over Antarctica. Consequently, Ch. 2 details 'empirical pointwise approach'. Chapter 3 combines the 'empirical pointwise approach' with an approach that estimates GIA and

ice-mass changes by means of a weighted least-squares adjustment. A sophisticated time series analysis is subject of Chapter 4. Chapter 5 utilizes the methodologies developed and tested in Chapter 3 and 4 to perform a sophisticated comparison of time series used in the combination. Finally, Chapter 6 comprises the main conclusions and some recommendations for potential future work.

#### 1.4. NON-PUBLIC DATA SOURCES

This section contains all the contributions to the work summarized in this thesis that have been provided directly by collaborative researches and are not publically available.

Two releases of surface height changes using ICESat altimetry data were derived by Brian Gunter, who is now at the Georgia Institute of Technology, but still formally affiliated with Delft University of Technology. Two versions of regional atmospheric climate model for Antarctica (RACMO2.0 and 2.3) were provided by Jan Lenarts, Stephan Ligtenberg and Michiel van den Broeke from Utrecht University. The model includes a dataset for surface mass balance and a firn densification model. Reprocessed GPS time series were provided by Matt King from University from Tasmania. Pavel Ditmar and Hassan Hashemi Farahani, from Delft University of Technology, provided unconstrained monthly DMT1 and DMT2 solutions with full noise covariance matrices. Himanshu Save, from University of Texas, provided CSR regularized solutions. Load love numbers in Center-of-Mass were provided by Riccardo Riva from Delft University of Technology.



# 2

## EMPIRICAL POINTWISE APPROACH

### 2.1. INTRODUCTION

In this Chapter, present-day GIA and ice-mass changes are estimated using an empirical pointwise approach by exploiting the strengths of independent satellite gravimetry and altimetry data. The addition of the altimetry products to the GRACE observations is particularly important because they track absolute *volume* changes, as opposed to the absolute *mass* change measured by GRACE. While these are two completely different observables, they are complimentary and permit the separation of the GIA and ice mass loss, given knowledge of ice/rock densities. This is possible because the large density contrast between rock and ice, as well as the large differences in their respective volume changes, allows the altimetry products to better isolate the volume/mass changes associated with surface processes, e.g., glacial thinning. For example, if a given region has decimeter-level annual glacial thinning in addition to mm/yr uplift in the solid-earth due to GIA, the altimetry would predominately observe the height changes due to the glacial thinning; however, the corresponding (large) mass change from the small solid-earth uplift would be clearly observable from GRACE. Previous studies have demonstrated the feasibility of this approach (Wahr et al, 2000; Velicogna and Wahr, 2002), with the first real-data combination presented by Riva et al (2009). As a joint estimation problem, GIA and ice mass change trends are simultaneously computed, creating a self-consistent set of estimates. In addition, as a data-driven approach, the errors of the input data sets can be used to generate realistic and spatially varying uncertainties of the resulting GIA and mass change estimates through standard error propagation techniques. In the time since the first real-data combination

---

*This chapter is based on B. C. Gunter, O. Didova, R. E. M. Riva, S. R. M. Ligtenberg, J. T. M. Lenaerts, M. A. King, M. R. van den Broeke, and T. Urban (2014). Empirical estimation of present-day Antarctic glacial isostatic adjustment and ice mass change. The Cryosphere, 8(2):743-760.*

was achieved, several major improvements to the methodology and data sets have taken place, resulting in new estimates of Antarctic GIA and ice sheet mass balance that will be highlighted in this Chapter.

New contributions of this work include the use of updated data from GRACE and the Ice Cloud and land Elevation Satellite (ICESat) mission, which have both undergone a complete reprocessing that has noticeably improved the data quality compared to previous releases. For the GRACE data, a range of both unconstrained and regularized solutions are evaluated to better categorize the impact that different processing strategies can have on the results. The ICESat data was processed using a recently developed technique involving the use of overlapping footprints (OFPs). The approach was first developed by [Slobbe et al \(2008\)](#) for a study of the Greenland ice sheet, but has not been applied previously to Antarctica. The OFP approach was expanded and improved for this study, and made use of the latest release of ICESat data (R633). The OFP method has many benefits over standard repeat-track and cross-over techniques, and is particularly well-suited for Antarctica due to the high density of laser shots available. The technique also allows for the independent determination of the systematic campaign biases which are present in the ICESat surface height rates, a critical item when considering long-term ice sheet volume changes.

Another important contribution of this chapter is the use of a firn densification model (FDM) that estimates spatial and temporal variations in firn layer temperature, depth and mass, and which also accounts for penetration, retention and refreezing of meltwater. Most similar studies to date have relied on a simplified density assumption to convert altimetric heights to mass, often just a constant value (e.g., [Forsberg et al, 2017](#)). For many regions which experience highly variable accumulation rates, as well as glacial thinning and high GIA rates, a constant surface density assumption significantly misrepresents the true surface characteristics. Finally, the GIA component of the data combination was compared against vertical height displacement measurements collected from a network of dozens of permanent GPS ground stations. Such comparisons allowed the various data combinations to be evaluated, both with each other, as well as against state-of-the-art GIA models.

In this Chapter, the impact of these new developments on the GIA and ice mass change estimates of Antarctica will be assessed. As will be shown later, the resulting GIA models compare favorably with other modelled estimates, but do suggest some areas, such as the Amundsen Sea Sector, may be experiencing much higher uplift rates than previously predicted.

## 2.2. METHODOLOGY

The underlying methodology used to combine the altimetric and gravimetric data sets is adapted from the earlier work by [Riva et al \(2009\)](#), summarized here for convenience. In short, the technique relies on the fact that satellite altimetry measurements primarily observe surface processes, such as accumulation and ablation, whereas the mass change measurements from satellite gravimetry are sensitive to the mass change of both GIA and surface processes. By exploiting the difference in

density between ice/snow,  $\rho_{\text{surf}}$ , and the solid earth,  $\rho_{\text{rock}}$ , the following relationship can be established which relates the vertical height rates of GIA,  $\dot{h}_{\text{rock}}$ , to the mass, height, and density values for a given location.

$$\dot{h}_{\text{rock}} = \frac{\dot{m}_{\text{GRACE}} - \rho_{\text{surf}} \cdot \dot{h}_{\text{ICESat}}}{\rho_{\text{rock}} - \rho_{\text{surf}}} \quad (2.1)$$

A 400 km Gaussian smoothing is applied to ensure the various components in Eq. (2.1) have the same spatial resolution, but this is only done after elements with equivalent resolution are first combined (including terms in both the numerator and denominator). For example, the multiplication of the surface density and ICESat height rates is done before applying the smoothing, since these two grids have approximately the same spatial resolution. The smoothing of the GRACE data helps reducing the noisiness of the solutions, but undoubtedly attenuates the signal magnitude. That said, the geolocation of the peak signals should not be significantly affected, and the total mass change should remain the same after smoothing, since the Gaussian filter simply redistributes the signal and conserves the total mass. This redistribution is also why a buffer zone of the same width as the Gaussian correlation length (400 km) was used when computing total mass change estimates. How the surface and rock densities are treated will be covered in the next section, as well as the consideration of elastic effects.

## 2.3. DATA SETS

Several data sets are used to perform the combination, as well as validate the results. For this chapter, the total mass change estimates were derived from GRACE and the surface height trends derived from ICESat. The properties of the surface, i.e., surface mass balance (SMB) and firn layer changes, were taken from Antarctic climate and firn densification models. The solid earth densities were assumed to be 4000 kg/m<sup>3</sup> for land, transitioning to 3400 kg/m<sup>3</sup> under the ice-shelves, consistent with [Riva et al \(2009\)](#). The physical reason for the lower density value in the coastal areas (in particular under the largest ice shelves) is two-fold. First, GIA also induces sea level changes, meaning that geoid changes over the ocean will be due to the movement of both rock and water masses. Second, ocean loading will affect the evolution of GIA itself, where the latter has been extensively discussed by [Simon et al \(2010\)](#). Only the surface heights and surface processes over the grounded ice sheet were used, since these changes do not contribute to mass change over the ice shelves, while the GRACE data were used over both land and ocean regions. The time period under investigation covers the entire ICESat mission period, from February 2003 to October 2009.

### 2.3.1. GRAVIMETRY

The GRACE mission has collected data on the time-variable nature of Earth's gravity field since its launch in March 2002. A number of research centers produce monthly gravity field models, using different processing methodologies. A range of gravity models are examined in this chapter, including those generated by the Uni-

versity of Texas at Austin Center for Space Research (CSR), the GeoForschungsZentrum (GFZ), and Delft University of Technology (TUD). Both RL04 and RL05 solutions were evaluated when available, as well as regularized solutions, i.e., those solutions applying additional spatial filtering or other processing methods to the standard L1 or L2 data products released by the GRACE Science Data System (SDS). Future references to GRACE "unconstrained solutions" refer to the standard monthly gravity field models provided to the public by the CSR and GFZ that have not had such regularization applied. Degree one coefficients were added to all solutions using values generated from the approach of [Swenson et al \(2008\)](#) (using RL05 GRACE data), and the  $C_{2,0}$  harmonics were replaced with those derived from satellite laser ranging ([Cheng and Tapley, 2004](#)). For the RL04 models, the secular trends that are removed from select zonal coefficients were restored (see [Bettadpur \(2007\)](#) for more details), as these rates are believed to mostly represent the effects of GIA ([Cheng and Tapley, 2004](#)). These zonal rates are not removed in the RL05 data processing scheme, so no adjustments were needed for the RL05 models.

For all solutions except the Delft Mass Transport (DMT-1b) models produced at TUD ([Liu et al, 2010](#)), which use a specialized method for the trend estimation ([Siemes et al, 2013](#)), a linear trend was estimated using least squares for each harmonic coefficient across the entire time series of monthly models (again, covering only the time period from February 2003 to October 2009). The trend was co-estimated with a bias, annual periodic, and tidal S2 (161 day) periodic terms. Earlier studies ([Seo et al, 2008](#)) indicated that additional aliasing may occur at other tidal frequencies, e.g., K2 (1362.7 dy); however, an investigation into these revealed that only S2 showed a noticeable influence on the long-term trends over Antarctica, particularly for the newer RL05 solutions. Evidence for this is provided in [Fig. 2.1](#), which shows the amplitude of the estimated K2 periodic signal in units of equivalent water height (EWH) computed from both a representative GRACE solution (CSR RL04 DDK3 in this case) and the 330 km Gaussian smoothed surface mass balance (SMB) estimates from the RACMO2 climate model (see [Sec. 2.3.3](#)). The fact that the majority of the areas with larger amplitudes in the GRACE solution ([Fig. 2.1a](#)) are spatially correlated with those seen in the SMB estimates ([Fig. 2.1b](#)), suggests that the signal seen in the GRACE data is genuine mass variability at this frequency.

For the unconstrained CSR and GFZ solutions, the estimated long-term trend was then de-striped using an approach similar to that outlined by [Swenson and Wahr \(2006\)](#), but with the filtering parameters described by [Chambers and Bonin \(2012\)](#). Even though these parameters were created with ocean applications in mind, the choice of polynomial degree (5th order for RL04, 4th order for RL05) and starting degree and order (12 for RL04, 15 for RL05) were found to perform better than other alternative parameters tested, and were therefore used in this chapter. No de-striping was applied to any of the regularized solutions, or to any of the other data sets (altimetry, climate, etc.) used in the combinations.

Several sets of regularized solutions were included in the analysis, to examine the potential impact that different spatial filtering techniques may have on the final results. This included the Wiener-type filter described by [Kusche \(2007\)](#),

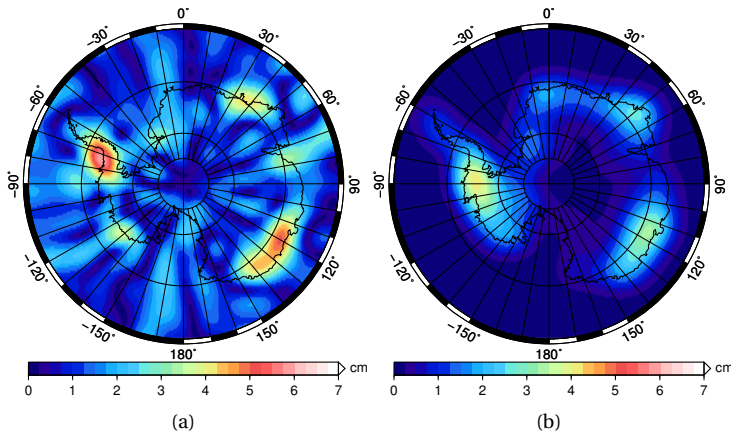


Figure 2.1: Magnitude of K2-periodic signal in EWH for a) GRACE CSR RL04 DDK3 and b) RACMO2 SMB.

which was applied to the RL04 (DDK3) and RL05 (DDK5) solutions for both the CSR and GFZ. A recently developed set of filtered solutions developed by [Save et al \(2012\)](#), utilizing an L-curve method with Tikhonov regularization, were also evaluated (named here "CSR Reg"). Finally, for the DMT1-b solutions, the anisotropic filtering method developed by [Klees et al \(2008\)](#) is applied after the long-term coefficient trend is estimated (along with bias, annual, and S2 terms). In total, 10 different GRACE solutions were evaluated, with the geographical plots shown in Fig. 2.2. As can be seen, the trends for nearly all solutions are quite similar; however, some variations can be seen in terms of magnitude and resolution of finer features. As will be seen later, these variations will have an important influence of the outcome of the estimated GIA and ice mass change values from the data combinations.

### 2.3.2. ALTIMETRY

The ICESat mission was the first Earth-orbiting laser altimeter. While no longer operational, it was able to collect valuable information on the long-term (multi-year) surface height change of Antarctica over a period which directly coincides with when the gravity data from GRACE was collected. The surface height change trends used in this chapter were computed using the release (R633) of ICESat data ([Zwally et al, 2011](#)), and were computed using an approach involving OFPs, similar to that described by [Slobbe et al \(2008\)](#) for Greenland. This is the first time the OFP approach has been applied to Antarctica. The technique is well suited for observing long term trends at a high spatial resolution, since the co-location of the laser shots used in the height change estimates do not rely on interpolation and/or surface approximations inherent in other techniques, such as cross-over and repeat-track analysis ([Felikson et al, 2017](#)). The technique is particularly useful for height change studies in Antarctica due to the high density of laser shots from the near-

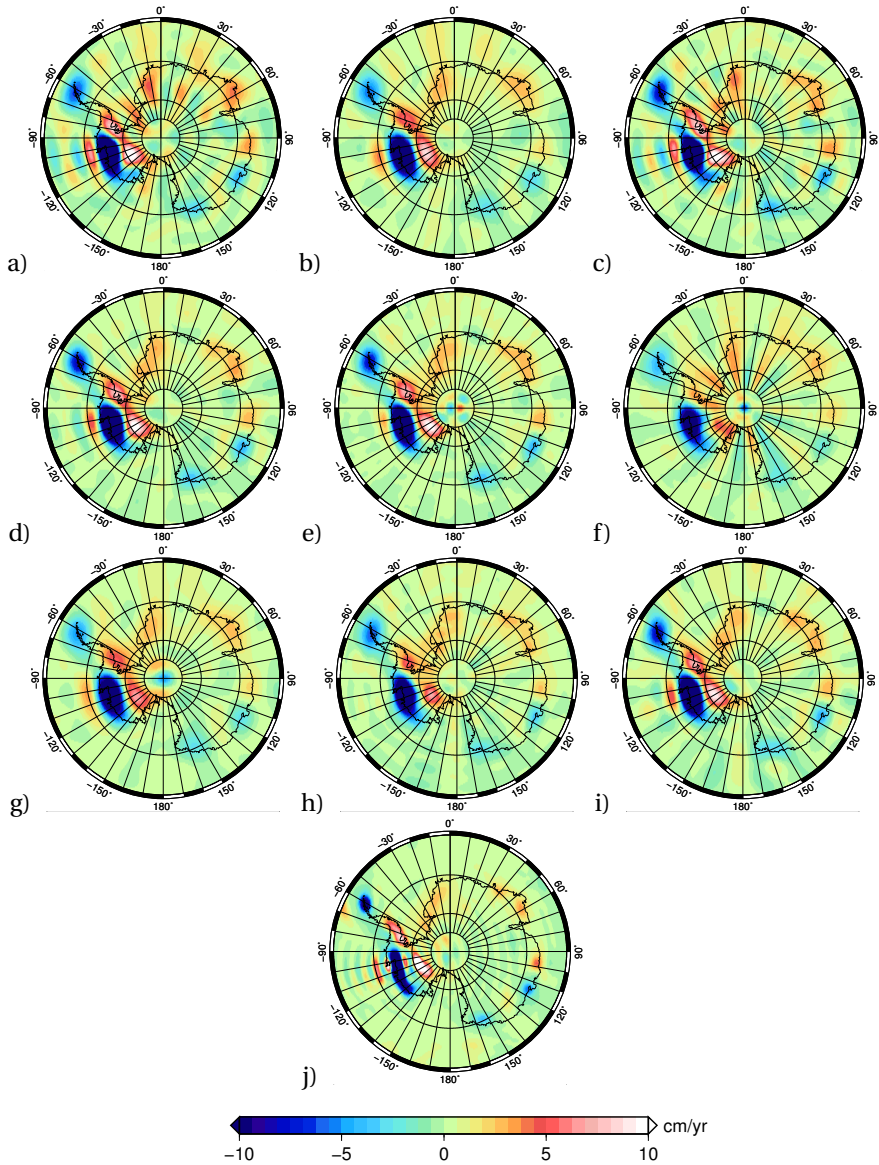


Figure 2.2: Long-term mass change trends in units of EWH computed from the following GRACE solutions: a) CSR RL04, b) CSR RL04 DDK3, c) CSR RL05, d) CSR RL05 DDK3, e) CSR RL05 Regularized, f) GFZ RL04, g) GFZ RL04 DDK3, h) GFZ RL05, i) GFZ RL05 DDK5, j) DMT-1b. For the plots shown, the unconstrained solutions (a, c, f, h) were de-stripped before trend-fitting, and only the GFZ fields (f, h) have had an additional 200km Gaussian smoothing applied to improve visualization.

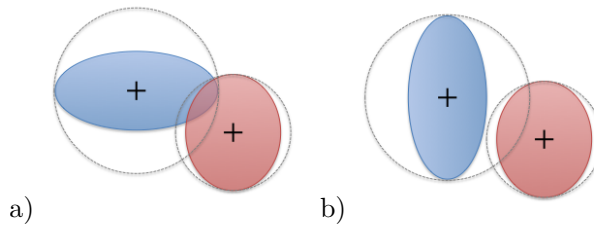


Figure 2.3: Illustration of a) an ICESat overlapping footprint (OFP) pair, and b) near-neighboring shots.

polar orbit of ICESat. The data processing uses a set of editing criteria to remove outliers, and estimates a custom set of inter-campaign biases, the details of which are outlined below.

#### OVERLAPPING FOOTPRINT APPROACH

The basic principle of the OFP approach is illustrated in Fig. 2.3a, where an overlapping footprint pair is defined as any two individual ICESat laser shots whose ground footprint have at least some overlapping area. The technique described by [Hughes and Chraibi \(2011\)](#) was used to determine if the ellipses characterizing any two laser shots physically overlapped, as well as the percentage of overlap. The two laser shots can come from any two ICESat campaigns and are not restricted to ascending or descending tracks; however, OFPs within the same campaign are excluded in this study due to the higher uncertainties they introduce. The height change ( $dh$ ) from an OFP pair is divided by the time difference ( $dt$ ) of the two shots to compute a height change rate ( $dh/dt$ ). To reduce the impact of slope effects, the degree of overlap can be used as an editing criterium so that the center of the two footprint ellipses is closer than some prescribed threshold value. This option will be used in the next section when estimating the inter-campaign biases.

To find potential OFPs, the maximum radius for each campaign (the footprint radius is not constant over time) is first determined based on all available shots. Any two shots whose centers are closer than the total sum of their respective campaign radii were considered OFP candidates. Depending on the shape and orientation of the two laser footprints, it is possible that two footprints can be close enough that their circumscribing circles overlap without the actual footprint ellipses overlapping, as illustrated in Fig. 2.3b. These neighboring shots in Fig. 2.3b offer the same information content as those in Fig. 2.3a, since the shot centers are still within twice the (maximum) semi-major axis distance from each other in both scenarios. As such, the ICESat-derived surface height trends used later include these neighboring shots, termed here "near-neighboring" (NNs) shots, to distinguish them from the physically overlapping OFPs. Approximately 151 million total OFP/NN shots were used, of which 76 million were NNs. Unless otherwise noted, future references to OFPs will imply that both OFP and NN pairs are included.

The original full set of R633 laser shots used in the analysis was edited using

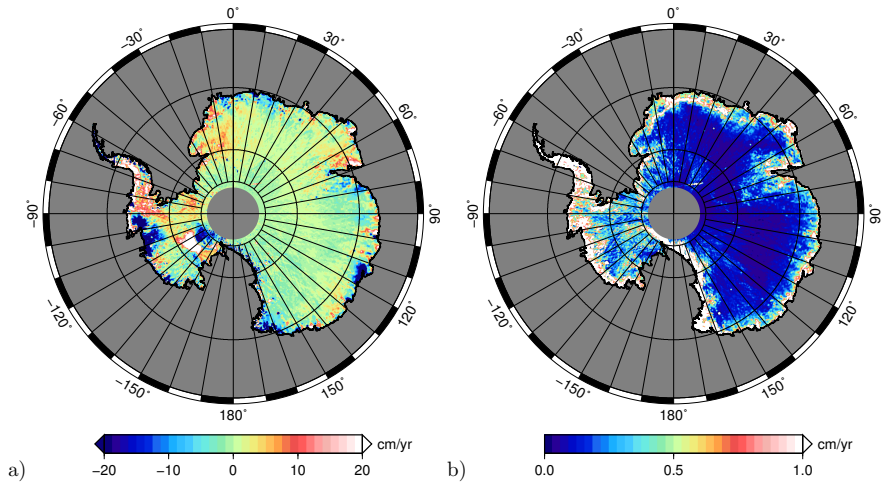


Figure 2.4: a) ICESat  $dh/dt$  estimates from the OFP approach and, b) corresponding uncertainties.

standard quality flags, as well as other criteria such as the use of only single peak shots, a maximum gain value of 150, and a maximum co-elevation angle of  $0.45^\circ$ . In addition, any  $dh/dt$  values computed from individual OFP/NN pairs greater than 12 m/yr were excluded, as this is assumed larger than most known glacial thinning or ablation processes (Pritchard et al, 2009). A linear trend in time (without annual terms) was fit using least squares across all ( $dh$ ,  $dt$ ) pairs satisfying the editing criteria within  $20 \times 20$  km area blocks, with the uncertainties determined by scaling the formal error from the least squares regression by the estimated variance of unit weight (EVUW) computed from the post-fit residuals (Strang and Borre, 1997). This EVUW scaling also helps to account for errors due to any seasonal variations that might be present. The estimated  $dh/dt$  values from this process are shown in Fig. 2.4a, with the corresponding uncertainties in Fig. 2.4b. When integrated only over the grounded ice sheet, using the boundaries defined by Zwally et al (2012), the total volume change is approximately  $-109 \pm 68 \text{ km}^3/\text{yr}$ . Most of the largest uncertainties are located in areas of steep topography, frequent cloud cover, and/or poor measurement sampling, and include regions such as the Transantarctic Mountains, Amundsen Sea Sector, and the Antarctic Peninsula, among others.

#### ESTIMATION OF CAMPAIGN BIASES

The ICESat laser shots are known to have a systematic bias in them that can introduce cm-level errors if neglected (Gunter et al, 2009). To minimize the effect of these campaign-specific biases, an approach to estimate their magnitude was adopted using a low-precipitation zone (LPZ) in East Antarctica, in line with Gunter et al (2010) and Riva et al (2009). While other techniques exist in the literature to estimate these campaign biases (Urban and Schutz, 2005; Siegfried et al, 2011; Ewert et al, 2012; Borsa et al, 2013), use of the LPZ offers several advantages as a calibra-

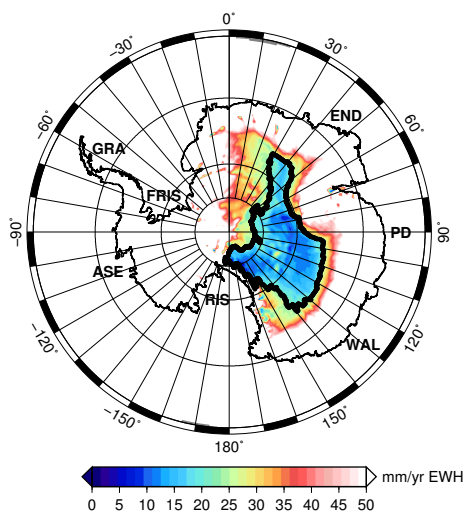


Figure 2.5: Outline of the low-precipitation zone (LPZ; black line) overlaid onto estimates of average yearly solid precipitative flux in units  $\text{mm} \cdot \text{yr}^{-1}$ , together with the following location indicators: Amundsen Sea (ASE), Graham Land (GRA), Filchner Ronne Ice Shelf (FRIS), Enderby Land (END), Philippi/Denman (PD), Wilkes/Adelie Land (WA), Ross Ice Shelf (RIS).

tion zone. First, the LPZ is one of the driest places on Earth, and gets very little precipitation and, hence, surface height change. Second, it is a large area, which helps improve the reliability of the results. The region is also local to Antarctica, whereas many other techniques are based on regions in other parts of the world. Finally, the density of ICESat groundtracks is highest in the polar regions, meaning many more observations can go into the estimation of the biases. The exact region used to estimate the campaign biases is shown in Fig. 2.5, and was derived using output from the regional climate model to be discussed in Section 2.3.3. In particular, the region corresponds to an area that is estimated to have less than 21.9 mm EWH/yr of average yearly solid precipitative flux, a value chosen by trial-and-error to create a continuous low-precipitation zone that is sufficiently isolated from areas of steep topography.

Using this LPZ, a selected set of ICESat measurements were used to estimate the biases. One of the advantages of the OFP approach is that the degree of overlap between two laser shots can be tuned to a specific range. With a higher overlap criterion, the shots have more coincident ground coverage, but at the expense of reducing the number of OFPs used, since fewer shots will satisfy the criterion. For the determination of the campaign bias, it was important that the shots involved in the OFPs have high levels of overlap, to reduce any potential errors caused by changes in the surface topography within the footprint area. As such, the OFPs used for the bias estimates were required to have at least an 80 % overlap with one or both of the laser shots. In addition, all dh values greater than 1m were considered outliers and excluded (this overlap and dh editing criteria were only used for

the determination of the campaign biases). A time series of the least median of squares of the remaining dh values were created, using each campaign as a reference, for a total of 18 different bias profiles (gray lines in Fig. 2.6). For example, the bias profile using campaign 3b would consist of dh values from the OFP combinations 1a-3b, 2a-3b, 2b-3b, etc. The mean of each profile was removed before taking the median value at each time step (dark blue). To investigate the influence of possible accumulation or compaction in the LPZ, the firn densification model (Section 2.3.3) was used to predict any surface change of the firn. The model did suggest a small surface lowering over the LPZ, on the order of  $-0.15$  cm/yr (magenta), and this value was removed from the median values to arrive at the final campaign bias estimates (cyan) shown in Table 2.1. Standard deviations for each campaign bias is also provided in the table. There is a small amount of variation in the biases from campaign to campaign, but the overall trend on the bias estimates is  $1.58 \pm 0.08$  cm/yr. The earlier 2.0 cm/yr bias estimates were computed using mean sea surface comparisons (Gunter et al, 2009). Other estimates are also available (Urban and Schutz, 2005; Siegfried et al, 2011; Ewert et al, 2012); however, these previous bias estimates used earlier ICESat data releases, so are not directly comparable to the estimates of this study. The G-C corrections to the ICESat data described by Borsa et al (2013) were not applied, as this is a relatively new development, but since the biases computed for this study are calibrated to the LPZ, this should not have a significant influence on the results assuming the G-C corrections essentially manifest themselves as campaign dependent biases (e.g., as shown in Table 1 of Borsa et al (2013)). Also note that because the mean was removed from the individual profiles, the values represent the bias offset with respect to the mid-point of the ICESat mission lifetime. The estimated biases were removed from the individual laser shots involved in the height change calculation for each OFP, i.e., before the trend-fitting by blocked area discussed in the previous section.

### 2.3.3. CLIMATE DATA

In order to separate the deformation caused by surface processes (ice, firn) from those of the solid-earth (GIA), both the volume and mass change of the ice sheet needs to be known. There are many complex processes at work that complicate the determination of these quantities, including regional variations in temperature, accumulation, and firn compaction. To account for them, the output of the RACMO2 regional atmospheric climate model is used, which is driven by ERA-Interim atmospheric reanalyses for the period 1979-2010 and run at a horizontal resolution of 27 km (Lenaerts et al, 2012). In conjunction with the time-varying estimates of SMB from RACMO2, which is the sum of mass gains (precipitation) and mass losses (surface runoff, sublimation and drifting snow erosion) at the ice sheet surface, a firn densification model (FDM; Ligtenberg et al (2011)) is also used, which is forced at the surface with the 6 hourly climate output of RACMO2. The FDM provides temporal surface height changes due to SMB variations, liquid water processes (snowmelt, percolation, refreezing and runoff) and firn compaction. Fig. 2.7 shows the total surface height rate, and associated uncertainties, as derived from the FDM model over the study period. It is important to note that the FDM

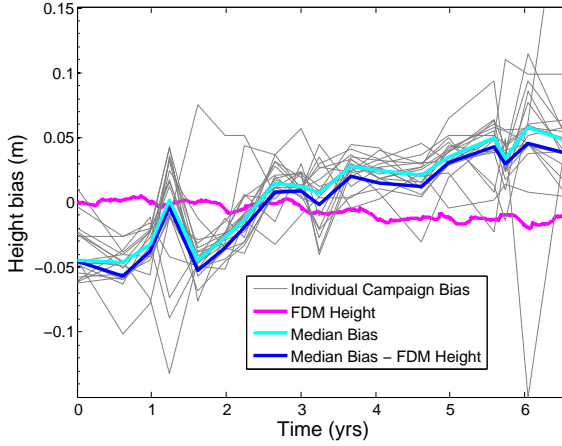


Figure 2.6: Illustration of the ICESat campaign biases determined over the LPZ for each individual campaign (grey), the mean value (cyan), and the mean minus the surface deformation (blue) predicted from the Firn Densification Model (FDM; magenta).

of Fig. 2.7 only represents the surface height changes of the firn, and does not reflect changes due to either the solid earth or ice dynamics. Furthermore, the mass change of the firn over time,  $\dot{m}_{\text{firn}}$ , is derived from the SMB, which is a separate product generated from RACMO2, although both the FDM and SMB estimates are inherently linked.

Two basic assumptions were made to account for height differences that were found to exist between the altimetry measurements and the FDM. First, the uncertainties of the height estimates derived from the ICESat and FDM data sets were defined over each approximately 20km x 20km grid cell as

$$\sigma_h = \sqrt{\sigma_{\text{ICESat}}^2 + \sigma_{\text{FDM}}^2} \quad (2.2)$$

using the standard deviations shown in Figs. 2.4 and 2.7. In order to convert the volume changes derived from the ICESat data into mass, the density of the material inside the volume needs to be known. Because RACMO2 only models firn processes, any negative differences between the ICESat and FDM surfaces that was greater than  $2\sigma_h$  for any given grid cell were assumed to be the result of ice dynamics (glacier thinning), and the density assigned to this volume loss was that of ice ( $917 \text{ kg/m}^3$ ). Similarly, any positive height differences beyond the  $2\sigma_h$  level were attributed to an underestimation of SMB by RACMO2, and given a density closer to that of snow using a static density profile similar to that of (Kaspers et al, 2004). The spatial variability of this density profile is illustrated in Fig. 2.8. The justification for the densities assigned to positive height differences is shown in Fig. 2.9. This plot shows the derived density (Fig. 2.9c) computed from those regions where the (GRACE - SMB) differences were greater than  $20 \text{ kg/m}^2/\text{yr}$ , and the (ICESat -

Table 2.1: Estimated ICESat R33 campaign biases and uncertainties by campaign.

Campaign	Start Date	End Date	# Days	Bias (m)	$\sigma$ (m)
1a/b	2003-02-20	2003-03-29	38	-0.046	0.017
2a	2003-09-25	2003-11-19	55	-0.057	0.015
2b	2004-02-17	2004-03-21	34	-0.038	0.017
2c	2004-05-18	2004-06-21	35	-0.004	0.047
3a	2004-10-03	2004-11-08	37	-0.053	0.034
3b	2005-02-17	2005-03-24	36	-0.035	0.023
3c	2005-05-20	2005-06-23	35	-0.019	0.024
3d	2005-10-21	2005-11-24	35	0.008	0.020
3e	2006-02-22	2006-03-28	34	0.009	0.013
3f	2006-05-24	2006-06-26	33	-0.002	0.026
3g	2006-10-25	2006-11-27	34	0.020	0.014
3h	2007-03-12	2007-04-14	34	0.015	0.010
3i	2007-10-02	2007-11-05	37	0.012	0.014
3j	2008-02-17	2008-03-21	34	0.031	0.013
3k	2008-10-04	2008-10-19	16	0.043	0.029
2d	2008-11-25	2008-12-17	23	0.029	0.025
2e	2009-03-09	2009-04-11	34	0.045	0.056
2f	2009-09-30	2009-10-11	12	0.037	0.055

FDM) were greater than 6 cm/yr. The resulting densities in Fig. 2.9c are predominantly in the 350-600 kg/m<sup>3</sup> range, with a mean value of 381 kg/m<sup>3</sup>, suggesting that the use of snow densities for these positive height anomalies is reasonable. Note that the Kamb Ice Stream region in West Antarctica was not included in the comparisons of Fig. 2.9. The Kamb Ice Stream is a special area where no ice discharge takes place, and the positive height change is assumed to be a build-up of ice (glacier thickening). For this reason, the (positive) height differences in this area were assigned a density of 917 kg/m<sup>3</sup>. This was the only location where the default density rules of positive or negative height differences were not applied. If the height differences between ICESat and the FDM fell within the  $2\sigma_h$ , the height measurements were considered to be within the uncertainty of the data sets, and the volume/mass of the difference was neglected. It is important to note that these assumptions only deal with potential residual signal observed between ICESat and the FDM. The majority of the surface mass changes comes directly from the SMB estimates (i.e.,  $\dot{m}_{\text{firn}}$ ) derived from RACMO2. As such, the utilization of the SMB and FDM in the combination approach required a modification of Eq. (2.1),

$$\dot{h}_{\text{rock}} = \frac{\dot{m}_{\text{GRACE}} - [(\dot{h}_{\text{ICESat}} - \dot{h}_{\text{firn}}) \cdot \rho_{\alpha} + \dot{m}_{\text{firn}}]}{\rho_{\text{rock}} - \rho_{\alpha}} \quad (2.3)$$

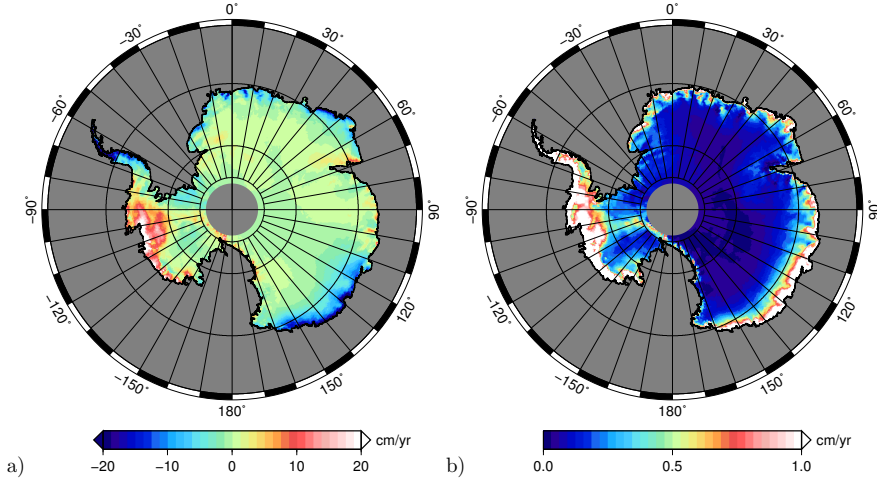


Figure 2.7: a) Firm Densification Model (FDM) surface height velocities and, b) corresponding uncertainties.

where

$$\rho_{\alpha} = \begin{cases} 917 \text{ kg/m}^3, & \text{if } \dot{h}_{\text{ICESat}} - \dot{h}_{\text{firn}} < 0 \\ & \text{and } |\dot{h}_{\text{ICESat}} - \dot{h}_{\text{firn}}| > 2\sigma_h \\ \rho_{\text{surf}}, & \text{if } \dot{h}_{\text{ICESat}} - \dot{h}_{\text{firn}} > 0 \\ & \text{and } |\dot{h}_{\text{ICESat}} - \dot{h}_{\text{firn}}| > 2\sigma_h \\ 0, & \text{otherwise.} \end{cases} \quad (2.4)$$

In words, this equation essentially takes the mass change associated with surface processes and subtracts this from the total mass change signal observed from GRACE. The remainder represents mass change due to GIA, which is converted to uplift using the assumed rock density (or density difference between rock and ice/firn, if applicable). The altimetry data, combined with the surface height changes from the FDM, primarily accounts for the changes due to ice dynamics, and the SMB model mostly accounts for the mass changes of the firn, with additional contributions from the altimetry when the observed/predicted surface heights from the ICESat and FDM data are sufficiently different (i.e.,  $> 2\sigma_h$ ).

It should be noted that, in the combination, an elastic correction is made for the load represented by the right-hand-side of the numerator in Eq. (2.3), i.e., from the surface mass variations computed from ICESat and the SMB data. This correction ultimately has a negligibly small influence on the final results, but is done merely for completeness.

#### 2.3.4. VERTICAL SITE-DISPLACEMENTS

The output from the combination represented by Eq. (2.3) is a vertical rate associated with GIA over Antarctica, hereafter referred to as the empirical rates. In par-

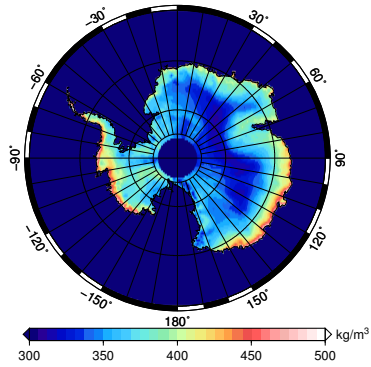


Figure 2.8: Surface density profile used to compute mass changes associated with differences between the FDM and altimetry surface heights.

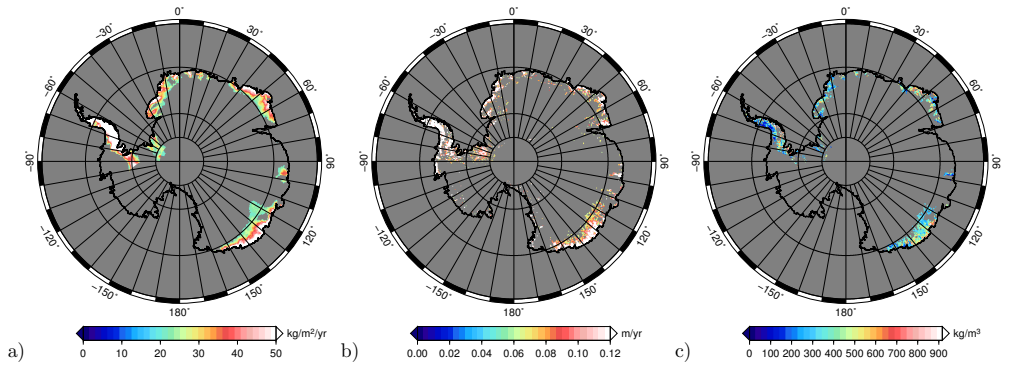


Figure 2.9: a)  $(\text{GRACE} - \text{SMB}) > 20 \text{ kg/m}^2/\text{yr}$ , b)  $(\text{ICESat} - \text{FDM}) > 6 \text{ cm/yr}$ , c) Derived density (mean  $396 \text{ kg/m}^3$ ).

particular, this rate refers to the rate of solid-earth uplift due to GIA, as opposed to the change in the geoid also associated with GIA, with future use of the term "GIA rate" implying only this solid-earth uplift. While a map of these values can be compared against other GIA models in an attempt to assess its accuracy, an alternative approach is to compare the empirical rates with those observed by ground-based GPS stations. For this chapter, vertical displacement rates for up to 35 GPS stations were used for the comparisons to be shown later. The processing of the GPS data followed the approach of [Thomas et al \(2011\)](#), and includes data from both campaign and permanent stations. Elastic deformation effects were accounted for using the model of [Thomas et al \(2011\)](#) based on ice mass flux observations ([Rignot et al, 2008](#)) with the exception of sites in the northern Antarctic Peninsula where the elastic model does not accurately reproduce near-field displacements. In this region, we therefore followed [Thomas et al \(2011\)](#) in adopting velocities for the period before 2002 as upper bounds on millennial-scale GIA. At the remaining sites the elastic corrections are generally small (typically  $< 0.3$  mm/yr) due to their location in the far field of the dominant ice mass changes within the Amundsen Sea Coast and the northern Antarctic Peninsula. Ice mass loading varied non-linearly over the GPS data period and this is not reflected in the elastic model. However, for sites outside the northern Antarctic Peninsula this is largely due to accumulation fluctuations. These fluctuations generally induce small and largely site-specific biases in the elastic model.

Following a similar approach as [Whitehouse et al \(2012\)](#), comparisons with the GPS data were done by computing the weighted root-mean-square of the residuals (WRMS) between the empirical or modelled vertical rates and those observed from the GPS stations ( $i$ ),

$$WRMS = \sqrt{\frac{\sum w_i \cdot (\dot{h}_{\text{rock}} - \dot{h}_{\text{GPS}})^2}{\sum w_i}} \quad (2.5)$$

where the weight,

$$w_i = \frac{1}{\sigma_{\text{GPS}}^2 + \sigma_{\text{rock}}^2} \quad (2.6)$$

incorporates both the uncertainty of the individual GPS stations ( $\sigma_{\text{GPS}}$ ) as well as the uncertainty of the GIA estimate ( $\sigma_{\text{rock}}$ , described later in [Sec. 2.5.1](#)) at the station location. The uncertainties for the GPS stations range from  $< 0.3$  mm (indicated by large symbols in [Fig. 2.14](#)), 0.3 to 1.5 mm (medium symbols), and  $> 1.5$  mm (small symbols). Additional details of the comparisons to the GPS displacements will be discussed in [Section 2.5](#).

## 2.4. GIA BIAS CORRECTION

One of the early observations from the combination results was the presence of a mm-level bias in the empirically derived GIA rates. Earlier investigations into this suggested that the cause of this bias could come from several sources ([Gunter et al, 2010](#)). For example, if there exists a secular trend in the geocenter motion (degree 1 coefficients), then any Z-component rate would be unaccounted for in this analysis. The uncertainty in the determination of  $C_{2,0}$  (related to Earth's oblateness)

from GRACE has been recognized for some time, and is the reason why values from satellite laser ranging are still recommended to be used in place of those found in the official data products. Any trend or other inconsistency in the coefficient values used for  $C_{2,0}$  would translate into a rate bias for Antarctica. Errors in the ICESat campaign bias could also contribute to the differences seen, as would any inconsistency in reference frames underlying the various data sets. It is important to note that every 1 mm of offset in the GIA rates over the entire continent would translate into approximately 50 Gt/yr of solid-earth mass change. Therefore, while the magnitude of the offset is small, its impact on the solution can be significant.

To address the issue of potential offsets in the solutions, use was made again of the LPZ shown in Fig. 2.5. The rate of GIA in this region is expected to be very small, i.e., significantly less than the unknown bias offset caused by the various sources discussed above. As such, the LPZ is used as a calibration area, where both the mean surface height change (Section 2.3.2) and subsequent GIA is assumed to be zero in that region. In terms of a practical implementation, this is accomplished by computing the mean value over the LPZ of the smoothed  $\dot{h}_{\text{rock}}$  values generated from Eq. (2.3). This mean value, termed the "LPZ GIA bias", is then subtracted from all GIA values uniformly. The magnitude of the LPZ GIA bias for each case investigated is shown in Table 2.2. Future references to the empirical GIA rates derived from the combination approach imply that this LPZ GIA bias has been removed.

Calibrating the solutions to the LPZ provides a simple but effective way to deal with the range of bias contributors (i.e., geocenter, reference frame, campaign bias, etc.) that are currently not known at the mm-level or less. Taking geocenter as an example, it was earlier mentioned that the degree one coefficients from Swenson et al (2008) were added to the GRACE data, although there exist many alternative estimates for these coefficients, such as those from Cheng et al (2011) and others, which often produce estimates of different phase and amplitude. As an illustration, the spatial variability in the estimated trends between the Swenson et al (2008) and Cheng et al (2011) coefficients can be seen in Fig. 2.10, expressed in units of cm/yr EWH. When either of these degree one solutions is used in the combination approach and calibrated over the LPZ (i.e., subtracting the LPZ GIA bias), the end results change by only a few Gt/yr, as shown in Table 2.3, even when considering the difference between EA and WA. This provides evidence that the LPZ GIA bias correction successfully removes the mm/yr level biases present in the degree one coefficients, regardless of which set of coefficients are used.

The LPZ bias correction also allows each solution to be compared more equivalently, since the bias contributors which are removed may be different for each case. The primary consequence for using the LPZ in this way is that the GIA solutions created become regional to Antarctica, and therefore cannot be used to estimate global GIA effects, such as the far-field GIA signal from the northern hemisphere. Second, if any genuine GIA over the LPZ does exist, then this would erroneously bias the empirically derived rates from the combination approach; however, as mentioned already, any error of this kind is believed to be much lower than that introduced by the various other (imprecisely known) bias contributors.

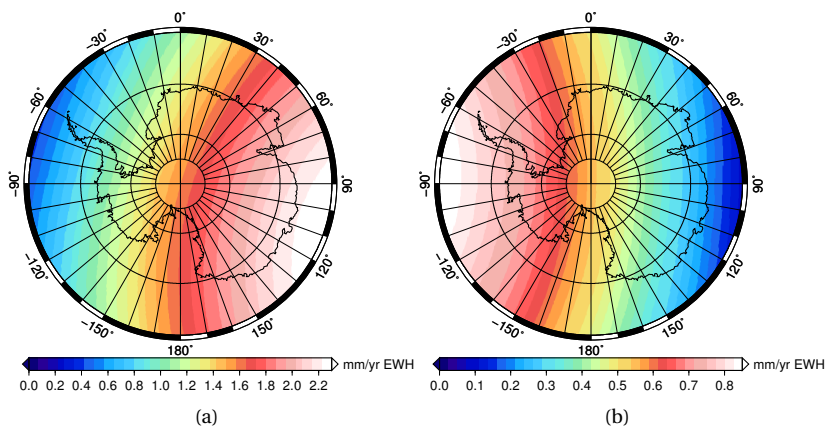


Figure 2.10: Comparison of degree one trends, in units of EWH, for two different sets of degree one coefficients: a) from Cheng et al (2011), and b) from Swenson et al (2008).

## 2.5. COMBINATION RESULTS

The geographical plots of the full set of the resulting GIA models created from the LPZ calibration approach are shown in Fig. 2.11. The corresponding mass change values are provided in Table 2.2, expressed in total gigatons per year (Gt/yr) and divided into regions representing East Antarctica (EA), West Antarctica (WA), and the total Antarctic Ice Sheet (AIS), following the grounding lines defined by Zwally et al (2012) (extended outwards by 400km to account for the smoothing). By multiplying the uplift rates derived from Eq. (2.3) by the density of rock, the resulting empirical GIA mass change rates were then subtracted from the total mass change estimated from GRACE to derive a corresponding ice mass change value, also shown in Table 2.2. Since the earlier LPZ GIA bias was estimated using all components in Eq. (2.3) (i.e., including SMB, surface heights, and GRACE), in order to compute the ice mass change estimates in a consistent manner, a separate LPZ bias was estimated for only GRACE, i.e., the "LPZ GRACE bias", the values of which are shown in Table 2.2 in units of EWH. Again, this is done to ensure that the mean value of mass change over the LPZ is set to zero.

As mentioned earlier, the altimetry and climate data were only used over the grounded ice sheet since the hydrostatic equilibrium assumed for the floating ice shelves would not introduce any mass changes over these regions. This means that the GRACE data is primarily responsible for estimating the GIA signal over the ice shelves. In addition, the ocean mass change over the ice shelves was assumed small compared to the mass changes associated with the solid earth uplift, so these effects were not directly treated in this study. To verify this claim, the ocean mass change over the entire 400km extended integration area was computed using the ocean mass change predictions from Bamber and Riva (2010), which includes the effects of self-gravitation. The total mass change over the entire Antarctic coastal region (i.e., within the 400km zone) was only 4.5 Gt/yr, confirming that the impact

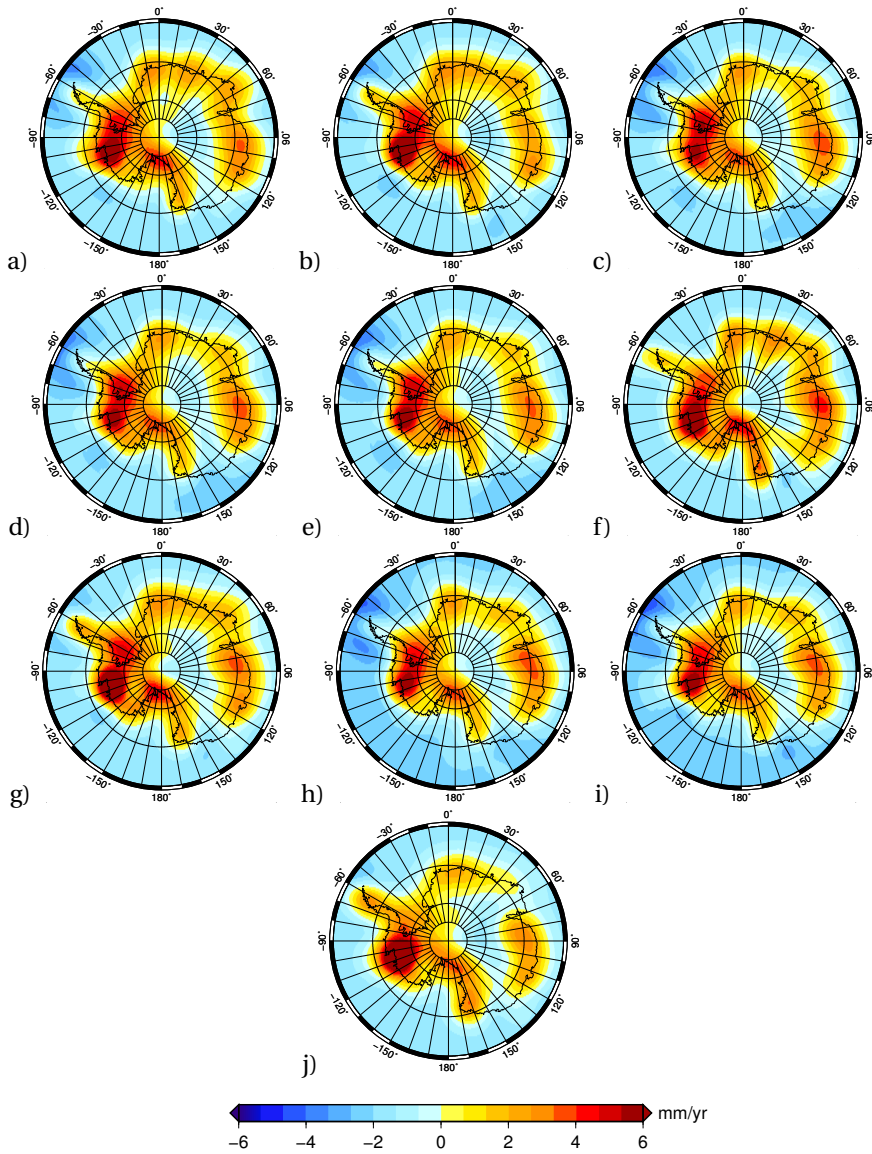


Figure 2.11: Estimated GIA vertical rates computed from the following GRACE solutions: a) CSR RL04, b) CSR RL04 DDK3, c) CSR RL05, d) CSR RL05 DDK5, e) CSR RL05 Regularized, f) GFZ RL04, g) GFZ RL04 DDK3, h) GFZ RL05, i) GFZ RL05 DDK5, j) DMT-1b

Table 2.2: Estimates of the mass change components derived from the data-driven approach. Uncertainties are  $1\sigma$ .

Solution	Max	LPZ bias		Total Est. Mass Change			Est. GIA			Ice mass change		
	Sph. Harm. deg $\times$ ord	GIA mm/yr	GRACE mm/yr EWH	from GRACE (Gt/yr)			(Gt/yr)			GRACE - GIA (Gt/yr)		
				EA	WA	AIS	EA	WA	AIS	EA	WA	AIS
CSR RL04	60	1.8	1.4	57	-71	-13	52	34	87	5	-105	-100
CSR RL04 DDK3	60	1.7	1.0	53	-66	-13	48	40	87	5	-105	-100
CSR RL05	60	1.9	1.7	42	-77	-35	37	28	65	5	-105	-100
CSR RL05 DDK5	60	1.9	1.7	42	-78	-36	37	27	64	5	-105	-100
CSR RL05 Reg	120	1.9	1.7	42	-78	-36	36	27	63	5	-105	-100
GFZ RL04	120	1.7	0.9	64	-62	2	60	43	103	4	-105	-101
GFZ RL04 DDK3	120	1.6	0.6	58	-59	-1	53	46	100	5	-105	-101
GFZ RL05	90	2.1	2.3	41	-86	-45	36	18	54	5	-104	-99
GFZ RL05 DDK5	90	2.1	2.4	39	-85	-47	33	19	53	5	-104	-99
DMT-1b	120	1.6	0.6	41	-58	-17	35	48	82	6	-106	-100
IJ05							33	41	74			
ICE-5G							53	48	101			
W12a							5	46	51			
Riva09							59	33	92			
$1\sigma$				18	6	19	34	21	40	38	22	44

2

Table 2.3: Influence of the two sets of degree one coefficients on the final solution estimates.

Solution	LPZ bias		Total Est. Mass Change			Estimated GIA			Ice mass change		
	GIA mm/yr	GRACE mm/yr EWH	from GRACE (Gt/yr)			(Gt/yr)			GRACE - GIA (Gt/yr)		
			EA	WA	AIS	EA	WA	AIS	EA	WA	AIS
CSR RL05 DDK5, deg1SW05	1.9	1.7	42	-78	-36	37	27	64	5	-105	-100
CSR RL05 DDK5, deg1SLR05	2.3	3.0	40	-83	-43	35	22	58	5	-105	-100

is small.

### 2.5.1. UNCERTAINTY ANALYSIS

Errors in the empirical GIA and ice mass change estimates from the combination approach were computed using formal error propagation techniques, resulting in what are believed to be realistic error uncertainties. Where possible, uncertainties provided for the individual input sources were used, while for other sources certain assumptions were made, the details of which are outlined below.

For the GRACE data, the uncertainties were derived using formal error propagation techniques and the publicly available calibrated errors provided by the CSR for each monthly solution, along with the uncertainties provided with the degree 1 and  $C_{2,0}$  coefficients. The calibrated errors were first propagated into equivalent water height (EWH) using the functional model described by Wahr et al (1998). These errors were in turn propagated into the trend component, using the same parameterization described earlier in Sec. 2.3.1. Though not shown, the GRACE errors do have a latitudinal dependency, but for Antarctica they are relatively uniform at approximately 1-1.5 mm/yr EWH. It is important to note that the formal errors for GRACE in this chapter are assumed to be the same for all solutions evaluated. This is improved later in Ch. 3 and 5 by incorporating the monthly full error variance-covariance matrices from the evaluated GRACE solutions.

The errors for the ICESat trends made use of the EVUW-scaled uncertainties discussed in Sec. 2.3.2, which are shown in Fig. 2.4b. Note that neither the GRACE

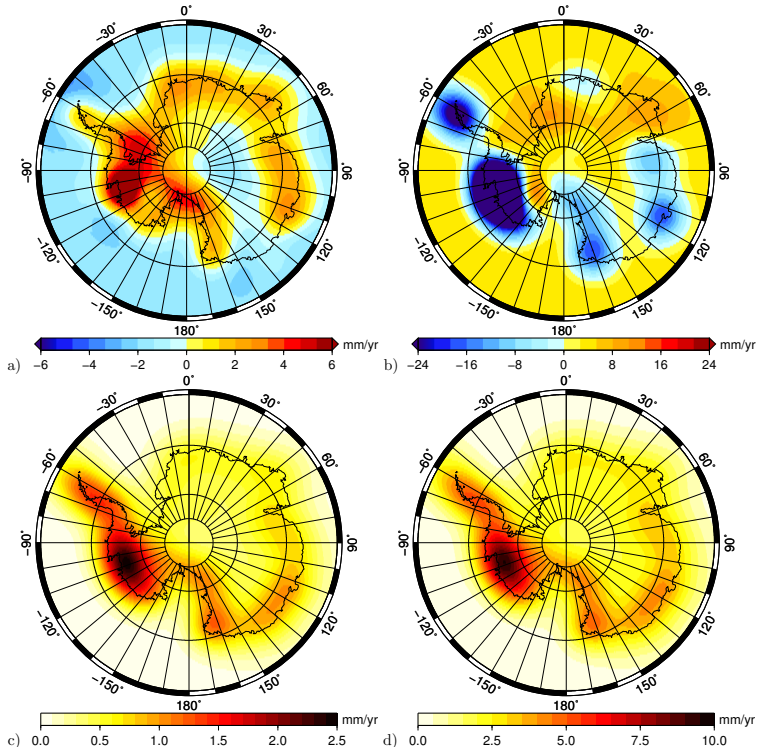


Figure 2.12: Estimates (a,b) and uncertainties (c,d) for the empirically derived GIA rates (a,c) in  $\text{mm}\cdot\text{yr}^{-1}$  and ice mass change rates (b,d) in  $\text{mm EWH}\cdot\text{yr}^{-1}$ , using the representative case CSR RL04 DDK3.

nor ICESat trends account for autocorrelation in their time series (Ferguson et al, 2004; Williams et al, 2014), so the uncertainties used here can be considered as lower bounds. The FDM has associated uncertainties, as shown in Fig 2.7b; however, the SMB information used to determine  $\dot{m}_{\text{firm}}$  in Eq. (2.3) do not have estimated uncertainties, so a standard deviation of 10% of the value for each grid point was used as a conservative estimate, similar to that employed by Rignot et al (2008). For the rock densities, a standard deviation representing  $100 \text{ kg}/\text{m}^3$  of the value for each grid point was assumed, representing a 33% uncertainty in the difference between the  $4000 \text{ kg}/\text{m}^3$  upper range used and the average value of  $3700 \text{ kg}/\text{m}^3$  proposed by Wahr et al (2000). Likewise, for the surface density value used when treating the differences between ICESat and the FDM, a 10% standard deviation was also used per grid point.

The aforementioned input data uncertainties were then formally propagated using Eq. (2.3) to generate total uncertainties for the three major mass change quantities (total mass change, GIA-related mass change, and ice mass change) for EA, WA, and the AIS. The uncertainties for the AIS were computed by taking the square-root of the sum-of-squares of the EA and WA uncertainties. This is con-

sistent with the analysis done as part of the recent Ice Sheet Mass Balance Inter-comparison Exercise (IMBIE) (Shepherd et al, 2012). And this is justified by the fact that the primary signals in EA and WA are sufficiently separated that their errors can be treated as independent of each other. These results are summarized in the last row of Table 2.2, with the geographical variation of the uncertainties shown in Fig. 2.12. The GIA uncertainties ( $1\sigma$ ) over the AIS are 40 Gt/yr, with the regions of higher uncertainties located in the areas most expected, such as the Amundsen Sea Sector (ASE) and Wilkes/Adelie Land (WA), correlating to the regions of highest uncertainty in the SMB and altimetry data sets. The ice mass change estimates are relatively well defined for WA at 22 Gt/yr, with more uncertainty over EA, due primarily to the much larger surface area involved. In general, the ice mass change uncertainties match those of the IMBIE study, as well as other recent studies (King et al, 2012; Jacob et al, 2012). Determining uncertainty levels for GIA uplift rates is inherently difficult to quantify with current modeling techniques, and is therefore one of the strengths of the data-driven approach. A more detailed discussion on the implications of these uncertainties on the results will be provided in the next sections.

### 2.5.2. COMPARISONS WITH GPS GROUND STATIONS

To gain more insight into the performance of the estimated GIA rates, as well as to ensure a fair comparison with existing GIA models, the GPS rates were compared to several variants of the estimated GIA uplift rates. The first approach uses the same WRMS calculation described by Eqs. (2.5) and 2.6, using the empirical rates corrected with the LPZ GIA bias described earlier, along with the estimated GPS and GIA uncertainties. Both the full 35-station set of GPS stations were used, as well as a smaller subset of 29 stations. The 29-station subset was chosen to remove the influence that stations on Graham Land (GRA) might have on the WRMS calculations, as well as two other stations which showed vertical rates with large differences ( $> 5\text{mm/yr}$ ), or were opposite in sign, to neighbouring GPS sites. GRA is a particularly dynamic region, and there are many factors that could impact the comparison of the GPS and derived GIA rates (Scambos et al, 2004; Thomas et al, 2011). Examples include potentially strong elastic effects on the GPS stations, the fact that the area is poorly covered with ICESat data, and the ability of GRACE to resolve the mass change of narrow North-South oriented features. The WRMS comparisons for both sets of GPS stations are shown in Table 2.4, with the stations excluded in the 29-station subset designated by square symbols in Fig. 2.14.

The results shown in Table 2.4 are useful for evaluating the performance of the various individual cases computed from the combination approach, primarily because the uncertainty of the resulting GIA rates can be used in the WRMS calculation. For comparisons of the empirically derived GIA rates to those from existing GIA models, the uncertainties of these models are not always available. Therefore, the comparisons with the GIA models were handled slightly differently, with the intention of making the comparisons fair. The individual assumptions and choice of Earth model parameters for each of the models is different, and again may result in a bias offset with the observed GPS rates. To account for these, a bias term

Table 2.4: Comparison of estimated GIA rates with GPS vertical rates, using the uncertainties for the both the GPS and GIA uplift rates in the WRMS calculations

Solution	WRMS	
	29 GPS station set	35 GPS station set
	mm/yr	mm/yr
CSR RL04	1.9	2.1
CSR RL04 DDK3	1.9	2.1
CSR RL05	1.8	2.1
CSR RL05 DDK5	1.8	2.1
CSR RL05 Reg	1.8	2.1
GFZ RL04	2.1	2.2
GFZ RL04 DDK3	2.0	2.1
GFZ RL05	1.9	2.2
GFZ RL05 DDK5	1.8	2.1
DMT-1b	1.8	2.0

was estimated and subtracted between the GPS and modelled-GIA rates before the WRMS was computed. This bias was estimated using non-uniform weights based on the GPS station uncertainties discussed in Sec. 2.3.4. A similar systematic bias term was also estimated for the empirical rates from the combination approach, and was removed in addition to the LPZ-bias term discussed previously. As shown in Table 2.5, the average systematic bias magnitude is approximately 1 mm/yr, and has an estimated uncertainty of  $\sim 0.3$  mm/yr, demonstrating the bias to be statistically significant. The removal of the GPS bias serves to reduce all solutions to the same frame as the GPS network, and ideally allows the WRMS values to reflect the spatial correlation with the station displacements and not additional systematic differences such as global reference frame differences or far-field model assumptions. In addition to the systematic bias correction, because model uncertainties are not provided for all models, only the uncertainties of the GPS stations were used in the WRMS calculations. This is equivalent to setting  $\sigma_{\text{rock}}$  to zero in Eq. (2.6). The empirical rates were compared to the rates predicted from three recent GIA models: the ICE-5G model (Peltier, 2004)<sup>1</sup>, the IJ05 model (Ivins and James, 2005), and the W12a model (Whitehouse et al, 2012)<sup>2</sup>. The Simon et al (2010) revision of the IJ05 model was used (full sea-level equation and global ocean loading) with no Antarctic continent load change since 800 years BP. Also included in the comparisons were the results from the earlier study by Riva et al (2009) (Riva09). As before, comparisons were made using both the full 35 and 29-station data sets, respectively. The results are listed in Table 2.5, and show both the original WRMS and bias-corrected WRMS values. For the GIA rates derived from traditional modeling techniques, it is recognized that the choice of different earth, ice-loading, or other parameters will result in more than just a uniform bias correction, and the errors involved may have some spatial variability; however, with-

<sup>1</sup>[www.psmml.org/train\\_and\\_info/geo\\_signals/gia/peltier/](http://www.psmml.org/train_and_info/geo_signals/gia/peltier/) [Last accessed on 2017-02-08]

<sup>2</sup>[www.dur.ac.uk/pippa.whitehouse/](http://www.dur.ac.uk/pippa.whitehouse/) [Last accessed on 2017-02-08]

Table 2.5: Comparison of estimated GIA rates with GPS vertical rates, using only uncertainties for the GPS uplift rates in the WRMS calculations.

Solution	29 GPS station set			35 GPS station set		
	WRMS	Systematic bias	bias-corr. WRMS	WRMS	Systematic bias	bias-corr. WRMS
CSR RL04	1.7	1.3	1.2	1.9	1.2	1.5
CSR RL04 DDK3	1.7	1.3	1.1	1.9	1.2	1.4
CSR RL05	1.6	0.9	1.4	1.8	0.8	1.6
CSR RL05 DDK5	1.6	0.9	1.3	1.8	0.8	1.6
CSR RL05 Reg	1.6	0.9	1.3	1.8	0.8	1.6
GFZ RL04	2.1	1.5	1.4	2.1	1.4	1.6
GFZ RL04 DDK3	1.8	1.4	1.2	1.9	1.3	1.4
GFZ RL05	1.6	0.8	1.4	1.9	0.6	1.7
GFZ RL05 DDK5	1.6	0.8	1.4	1.8	0.6	1.7
DMT-1b	1.7	0.9	1.4	1.8	0.9	1.6
IJ05	3.4	2.5	2.2	3.4	2.4	2.4
ICE-5G	3.0	1.2	2.8	3.0	1.1	2.8
W12a	2.2	1.4	1.7	2.3	1.3	1.8
Riva09	2.1	1.6	1.4	2.2	1.5	1.7

out more detailed knowledge of these variations, it was felt that removing these first order effects with a bias correction was more appropriate than not correcting for any systematic differences at all. Note also that the WRMS values shown for Riva09, IJ05 and ICE-5G are corrections to the values shown in [Thomas et al \(2011\)](#), and partially repeated in [Whitehouse et al \(2012\)](#), due to an error in their WRMS calculations (the updated values do not affect the ranking of these models in these earlier works). To visually examine the differences, a selection of three empirical solutions representing the various GRACE processing variations (CSR RL04 DDK5, CSR RL05 Reg, and DMT1-b) are plotted in [Fig. 2.14](#) alongside the three GIA models, with all figures representing the 35-station case after adjustment for the systematic bias. For reference, plots of the original unadjusted GIA models can be found in [Fig. 2.13](#).

### 2.5.3. DISCUSSION

Several observations can be made when examining the results of the combinations and the comparisons with the GPS vertical displacements. First, the spatial pattern of the empirically derived rates is mostly similar across all solutions, with most of the variations involving differences in magnitude. For example all solutions indicate sizeable uplift in WA, and a slight subsidence for most of the EA interior. Similar patterns of subsidence are also observed in the W12a and IJ05 models. The same can be said for the uplift beneath the Filchner Ronne Ice Shelf (FRIS) and Ross Ice Shelf (RIS). The magnitude of this uplift varies depending on the solution considered (including models), but in general the geographical location of the signal is common to all cases. It is worth noting here again that any height changes over the ice shelves were ignored since the hydrostatic equilibrium of the floating ice would not result in changes to the total column mass. Therefore, the empiri-

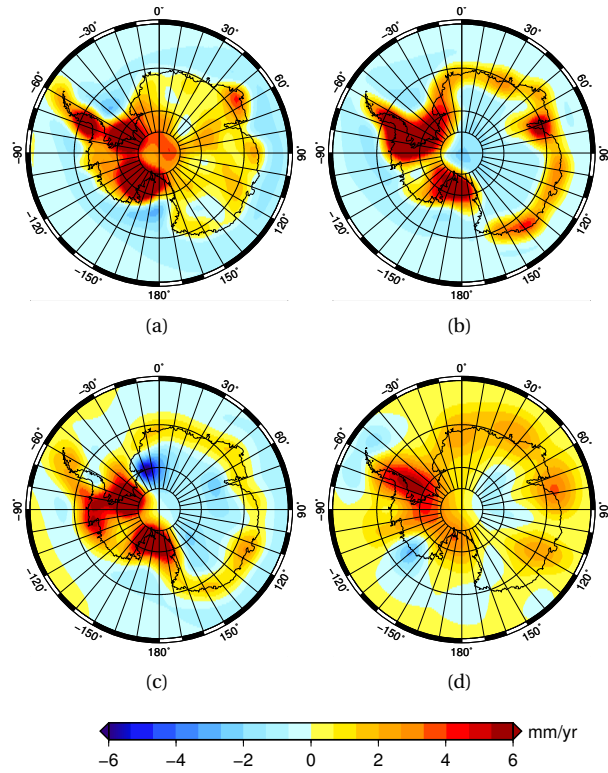


Figure 2.13: Original GIA uplift rates for a) ICE-5G, b) IJ05, and c) W12a, d) Riva09.

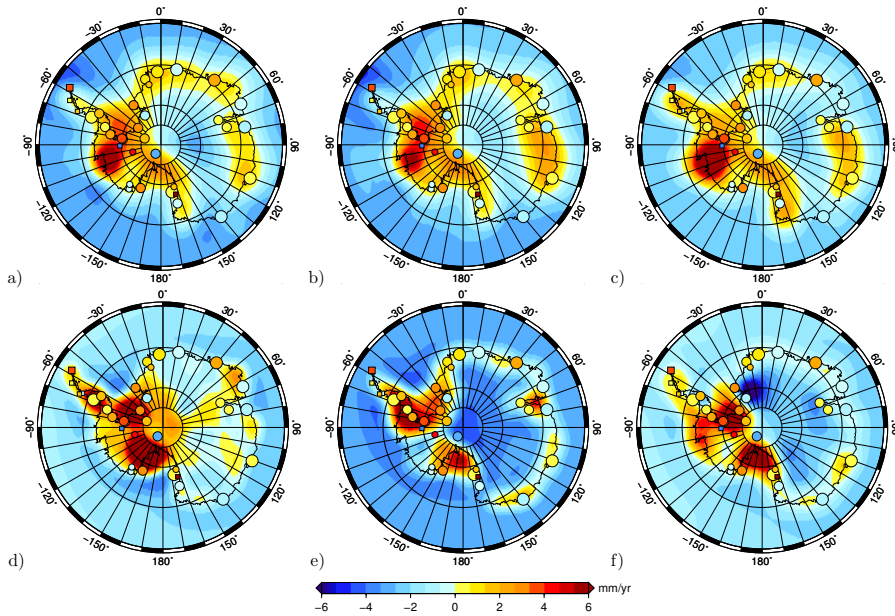


Figure 2.14: Comparison of the 35-station WRMS of the residuals between the vertical rates from the GPS stations and the uplift rates derived from the following empirical/modelled cases: a) CSR RL04 DDK3, b) CSR RL05 Reg, c) DMT-1b, d) ICE-5G, e) IJ05, and f) W12a. Note that, for these comparisons, a systematic bias is removed from the empirical/modelled rates with respect to the GPS network (see text for details).

cal GIA rates under the ice shelves were estimated almost entirely from the GRACE data, under the assumption that ocean mass changes in the region were negligible.

In the ASE, the empirical models indicate higher rates of uplift than those typically predicted in this area by the other models based on ice history reconstruction. There are several plausible reasons that might explain this signal. The first is that genuine GIA uplift is taking place in this area, as suggested in a recent study by [Groh et al \(2012\)](#); however, the in-situ data used to validate the results of this study were derived from only two seasonal GPS campaigns, so these data have large uncertainty and need to be confirmed by additional long-term GPS measurements. The error analysis for the combination approach, shown in [Fig. 2.12c](#) produced a  $1\sigma$  uncertainty level of approximately 2 mm/yr for the ASE, making the 6+ mm/yr uplift rates shown by all of the empirical rates in [Fig. 2.11](#) statistically significant (at the 95% level of confidence), providing additional evidence that the observed uplift is real. The earlier results obtained by [Riva et al \(2009\)](#) do not show the same degree of uplift in the ASE (see [Fig. 2.11](#)), even though a similar technique was employed. The difference can be explained by the fact that the new approach presented here considers firn compaction and surface processes via the FDM and SMB estimates from RACMO2. The [Riva et al \(2009\)](#) study did not account for any surface height or density change caused by the sizeable amount of accumulation ( $> 10$  cm/yr, see [Fig. 2.7](#)) that takes place in the ASE, and assigned all volume loss the density of ice. Doing so generates a lower mass loss rate for the region; however, now that these surface processes are taken into account, the altimetry-derived mass loss is greater for the ASE, resulting in a positive mass offset when compared to GRACE that is interpreted as GIA uplift in the inversion.

That the traditional models based on ice history reconstruction do not show the same magnitude of signals as those estimated from the empirical approach may be largely due to the fact that these models do not typically consider ice load changes that have occurred in the past 1000 years or so. [Nield et al \(2012\)](#) showed that large, present-day changes in ice loading can have a noticeable impact on GIA uplift rates, particularly in regions of low viscosity, such as the Antarctic Peninsula.

Naturally, there are other plausible explanations for the observed uplift in the ASE. It is possible that the gridded ICESat height change maps may overestimate the total volume loss in the ASE, or that GRACE is underestimating the mass loss. In either of these cases, the resulting positive difference would be interpreted as GIA uplift in the combination. Alternatively, the SMB estimates could overestimate the amount of accumulation in the region, again causing the positive mass differential with what GRACE observes to be treated as GIA uplift. While no long-term GPS vertical rates are currently available in the ASE, there are a handful of permanent stations recently installed which will help validate these claims<sup>3</sup>. These future GPS measurements should also help to clarify the magnitude and spatial extent of the uplift, as some of the GIA solutions predict more widespread uplift than others. In particular, the RL04-based solutions tend to produce a larger extent of GIA uplift over the ASE than the RL05-based solutions, while the RL05 solutions indicate more uplift over the FRIS.

---

<sup>3</sup>[www.polenet.org](http://www.polenet.org) [Last accessed on 2017-02-08]

In the Philippi/Denman (PD) sectors, the empirical GIA rates show a stronger uplift pattern than those found in the GIA models (Figs. 2.11 and 2.13). It is not believed that the estimated uplift is the result of any unmodelled accumulation, as the ICESat and FDM results agree well in this region. The positive mass anomaly in the area is also consistently observed in the GRACE solutions (Fig. 2.2), in particular in the regularized solutions, which tend to have higher spatial resolution. Also, the uncertainty analysis does not suggest any unusual circumstances in the area. Unfortunately, the comparisons with the GPS rates are inconclusive, since the few stations in the area are located on the perimeter of the region in question. As such, the presence of genuine GIA uplift in the region will require more investigation before this can be confirmed.

As the methodology and comparisons described earlier make use of a number of different biases, it is useful to review these again for clarification. The first of the biases computed was for the ICESat data, to correct for known systematic rate offsets in the height measurements. It was computed over the LPZ under the assumption that very little surface height change takes place there. The LPZ is used again as a calibration zone to estimate an offset observed in the empirical GIA rates estimated from the combination approach. The presence of this offset is likely due to factors inherent in the data sets used, e.g., geocenter motion,  $C_{2,0}$ , etc. Each of them can introduce mm-level errors. The mean GIA uplift rate (emphasis on "mean") over the LPZ was assumed to be much smaller than these errors, so an empirical LPZ GIA bias was computed over this region for every empirical GIA solution and subtracted. Therefore, any reference to the empirical GIA solutions, including those in the tables and figures, imply that this LPZ GIA bias has already been removed. A LPZ GIA bias was not computed or removed from any of the modeled GIA data sets, as the reasoning behind the bias calculation was only relevant to the empirically-derived GIA uplift estimates; however, a separate offset correction was applied for the GPS comparisons. This was because a systematic offset was observed between the modeled/empirical GIA rates and those observed from the GPS stations, which was presumably due to differences in processing, e.g., reference frames and other effects. For this systematic offset, all GPS stations were used, and a unique bias was computed for each comparison made, with the intention of making the WRMS comparisons as equivalent as possible. For the empirical GIA rates, this systematic bias was applied in addition to the LPZ GIA bias, while for the modeled GIA data sets, only the systematic bias was used.

Looking at the WRMS values in Table 2.4, most solutions compare well with each other, with differences only at the 0.1-0.2 mm/yr level. Again, these were computed using only the LPZ GIA bias calibration and considering the uncertainty of both the GIA and GPS stations. When examining Table 2.5, which only considers GPS station uncertainties and removed an additional systematic bias term, more variation in the results can be seen. The CSR RL04 DDK3 solution showed the lowest WRMS after the systematic bias is removed at 1.1 mm/yr, but the results of the other regularized solutions for both RL04 and RL05 are comparable, particularly for the 35-station set. It is interesting to note that the RL04 solutions have a larger systematic bias correction than the RL05 solutions, which is likely due to the

difference in reference frames used in the GPS and RL04 GRACE data processing. In nearly all cases, the 29-station results are lower than the 35-station set. When comparing the empirical results to the model results, either with or without the systematic bias removed, the empirical rates show consistently lower values, with the IJ05 model having the closest similarity in terms of WRMS and spatial distribution of GIA uplift.

Regarding the ice mass change estimates, the values for all cases were relatively consistent. This is primarily a consequence of the fact that the surface height change information was fixed to that determined by the altimetry and FDM data sets. In the combination, this essentially determines the variability of the firn and ice layers, forcing any variation in mass change seen by GRACE to go into the GIA estimates. The empirically derived ice mass change rate of  $-100 \pm 44$  Gt/yr (EA:  $5 \pm 38$ , WA:  $-105 \pm 22$ ) from this study falls within the  $1\sigma$  range of predictions over the entire AIS from the recent IMBIE study (Shepherd et al, 2012) for a similar time frame ( $-57 \pm 50$ , Oct. '03 - Dec. '08, using W12a and IJ05\_R2;  $-137 \pm 49$  Gt/yr using ICE-5G), as well as recent studies by Sasgen et al (2013) ( $-114 \pm 23$ , 2003-2012) and Jacob et al (2012) ( $-165 \pm 36$ ,  $1\sigma$ , using ICE-5G). The empirical AIS estimates show more ice mass loss than recent results by King et al (2012) ( $-68.7 \pm 17.5$ , using W12a), with much of the difference occurring in EA ( $60 \pm 12.8$ ). In EA, the empirical results were closest to Sasgen et al (2013) ( $26 \pm 13$ ), but still within  $1\sigma$  of Shepherd et al (2012) ( $35 \pm 40$ ). Similarly, for the WAIS, the empirical GIA results were still within the  $1\sigma$  range of Shepherd et al (2012) ( $-68 \pm 23$ ), but were more similar to those from King et al (2012) ( $-117 \pm 9.2$ ) and Sasgen et al (2013) ( $-116 \pm 15$ ).

## 2.6. CONCLUSIONS

This chapter revisited the approach developed by Riva et al (2009) for estimating present-day GIA and ice mass change using a combination of satellite altimetry and gravimetry. An updated and extended ICESat surface height change map was combined with a range of different GRACE solutions, along with an advanced regional atmospheric climate model and associated firn densification model (FDM). New ICESat surface trends were computed, for the first time over Antarctica, using an overlapping footprint approach, complemented by a custom set of campaign biases. The FDM and surface mass balance (SMB) estimates derived from RACMO2 addressed a key limitation in the earlier study, and enabled the combination approach to treat variations in surface height and density due to firn compaction and other surface processes. Another key element of the analysis was the calibration of the results to a low-precipitation zone in East Antarctica, which helped reduce the impact of the mm-level (unknown) biases inherent to the satellite input data sets. Lastly, knowledge of the uncertainties for the various input data sources provided the opportunity to generate realistic error assessments of both the GIA and ice mass change estimates through formal error propagation methods. The total empirical GIA mass change estimates for the AIS ranged from 53 to 100 Gt/yr (EA: 31 to 53 Gt/yr; WA: 19 to 48 Gt/yr), depending on the GRACE solution used, with an estimated uncertainty of  $\pm 40$  Gt/yr (EA:  $\pm 34$ ; WA:  $\pm 21$ ). Over the time frame February 2003 to October 2009, the corresponding ice mass change aver-

aged  $-100 \pm 44$  Gt/yr (EA:  $5 \pm 38$  Gt/yr, WA:  $-105 \pm 22$  Gt/yr) across all solutions. This makes the total Antarctic mass change (ice and solid earth) over this 2003-2009 timeframe range from 0 Gt/yr to  $-47$  Gt/yr. Furthermore, the mean total Antarctic mass change for the RL04-based solutions is  $-9.6 \pm 7$  Gt/yr, and for RL05 is  $-39.8 \pm 5$  Gt/yr, highlighting the differences between the two data releases. The empirically derived GIA rates show some noticeable differences to other recent GIA models derived using the more traditional ice history reconstruction approach. The differences are found in the Amundsen Sea (ASE) sector and the Philippi/Denman (PD) sectors. They are also many similarities, such as the general subsidence in East Antarctica and uplift beneath the Ross and Filchner Ronne Ice Shelf. Some of the disagreement between forward-modelled and empirically-derived uplift rates may be due to the fact the forward GIA models do not typically consider ice-load changes during the last 1000 years, and this signal may be significant. The empirical GIA rates generated from this approach showed good overall agreement to an independent set of GPS-derived vertical rates. Although, there are no long-term GPS records in some of the suspected uplift zones, such as the ASE and PD sectors. The estimated vertical rates in these areas therefore cannot currently be verified. Nonetheless, the results from the combination approach demonstrate that the technique has the potential to reduce the uncertainty surrounding both Antarctic GIA and ice mass change estimates, and provide new insights into the impact that recent ice-load changes may have on present-day uplift rates.



# 3

## EMPIRICAL ADJUSTMENT APPROACH

### 3.1. INTRODUCTION

The focus of this chapter is on improving the gravity data post-processing and incorporating them into the combination approach to separate the GIA signal from that of changes in ice mass by exploiting the strengths of independent datasets. Although in Ch. 2 developed methodology allows forward modeled GIA to be independently validated, providing insights into the underlying geophysics, it may mask the complex spatial pattern of the estimated GIA and ice-mass changes. This is because of the way how the limited horizontal resolution of GRACE data used in the combination is dealt with (note that the 400 km half width Gaussian filter is applied to all datasets in the combination in Ch. 2 to ensure the same spatial resolution with GRACE-derived mass changes).

The limited horizontal resolution represents a major challenge when dealing with GRACE data. It is a result of (i) truncating the spherical harmonic coefficients during the processing of GRACE solutions and (ii) separating noise from the signal during the post-processing step. Noise in GRACE data (so-called 'stripes') is caused by the mission geometry in connection with limitations of current data processing strategies, instrument errors and uncertainties in background models (Teixeira Encarnação, 2015). Filtering and/or 'destriping' is the usual approach for suppressing noise in GRACE data, which causes spatial leakage and in turn, attenuation of signal and reduction of spatial resolution (Siemes et al, 2013). Spatial leakage prevents GRACE data from being fully exploited as it introduces an artificial re-distribution of mass e.g., mixing between signals in the coastal area or mixing between a strong positive with neighboring negative signal in the interior of a continent.

Different filtering techniques have been developed for GRACE solutions ranging from a simple isotropic Gaussian filter proposed by Swenson and Wahr (2006)

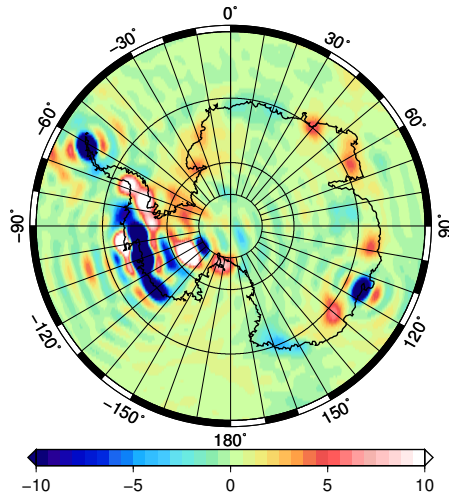


Figure 3.1: Optimally filtered long-term trend in cm/yr ewh generated using the approach from [Siemes et al \(2013\)](#) along with monthly GRACE solutions and their full error variance-covariance matrices as in [Farahani et al \(2016\)](#). The trend was co-estimated with bias, annual periodic, and tidal S2 (161 day) periodic term for the time period from Feb. 2003 to Dec. 2008, excluding June 2003.

to more sophisticated anisotropic filters (e.g., [Kusche, 2007](#); [Klees et al, 2008](#)). Following [Klees et al \(2008\)](#), a spatially varying Wiener-type filter, which is based on signal and noise covariance matrices, reduces leakage, and suppresses noise depending on the signal strength. In a recent study by [Farahani et al \(2016\)](#), the Wiener-type filter is applied to a linear trend following an approach developed by [Siemes et al \(2013\)](#). Their results suggest high spatial resolution for Antarctica when compared with the ICESat-RACMO-based results derived in Ch. 2. The detected high spatial resolution was attributed to an accurate computation of monthly noise covariance matrices and to the fact that the Wiener-type filter was applied to a trend yielding less aggressive filtering than on a monthly basis. However, in this way obtained high spatial resolution trend still suffers from ringing artifacts characterized by high spatial frequencies in the vicinity of strong mass variations ([Farahani et al, 2016](#)) as can be seen in Fig. 3.1.

There have been other studies aiming at an accurate spatial localization of mass changes. [Chen et al \(2015\)](#) used a forward modeling algorithm to reduce leakage between land and ocean due to the limited range of SH coefficients and commonly used Gaussian filtering. Using synthetic data, they demonstrated effectiveness of restricting signal to predefined regions, given knowledge about GIA, but did not examine whether this algorithm can cope with leakage between adjacent basins containing strong positive with neighboring negative signal as it applies for West Antarctica (WA). An alternative to the spherical harmonic representation of surface mass changes are mascons (i.e., single layer densities), which is an approach designed to reduce leakage and therefore, increase signal recovery. The mascon basis functions are directly related to GRACE Level 1B tracking data and

are represented by a finite truncated spherical harmonic expansion (e.g., [Luthcke et al, 2013](#)) or by an analytical expression (e.g., [Watkins et al, 2015](#)). Unfortunately, the recent mascon solutions still suffer from spatial leakage due to mascon shapes (discs) which are not based on geophysical boundaries, especially in the coastal regions ([Watkins et al, 2015](#)) and/or from leakage between the adjacent mascons due to signal covariance used that contains constraints regarding characteristic length and time (e.g., [Luthcke et al, 2013](#)). To obtain high-resolution spatial mass variation patterns while avoiding filtering of GRACE data, [Baur and Sneeuw \(2011\)](#) related gravity observations at the satellite altitude to point-mass variations on the Earth's surface interpreting each point as a small drainage basin. However, among all parameterizations used (point masses, SH coefficients, mascons), the parameterization of the real time-varying gravity field by single layer densities is the closest to the physical processes causing mass anomalies (e.g., [Wong et al, 1971](#)).

The aim of the work described in this chapter, is to fully exploit GRACE data for deriving the highest spatial resolution possible for GIA and ice-mass changes over Antarctica with the least possible noise content. For this, an approach developed by [Ran \(2017\)](#) is modified and used here in conjunction with the combination approach described in Ch. 2. This approach is hereafter termed the 'patch approach'. A patch is a bounded region on the Earth's surface with a constant mass layer. Akin to [Baur and Sneeuw \(2011\)](#), gravity disturbances at the satellite altitude are related in the functional model to the points on the Earth's surface, but here the surface mass layer representation of the Earth's gravitational field is used instead of a point-mass approximation (Sec. 3.3.1). This mass layer represents mass variations that occur over the patch, similar to mascons in e.g., [Luthcke et al \(2013\)](#); [Watkins et al \(2015\)](#). The patches are defined based on geophysical boundaries, i.e. by restricting ice-mass variations to the Antarctic Ice Sheet (AIS) by taking into account the grounding line position, identical to [Chen et al \(2015\)](#). Close-loop simulations are performed to demonstrate the capability of the patch-approach to recover a synthesized (noise-free) gravitational signal (Sec. 3.3.1). No destriping/filtering of GRACE data is required, because patches act as an inherent smoother on the data. Choosing patches too small is critical to the stability of the solution. Choosing patches too large, might lead to an oversmoothing and hence, to a loss of information. That means that patch definition is essentially a regularization by parameterization and must be performed carefully.

An important new contribution of this chapter is the development of the dynamic patch approach (Sec. 3.3.2) that adapts the parameterization to the signal. To help decide on a sufficient parameterization for estimated GIA, use is made of independent GPS observations (Sec. 3.4.1). The spatial resolution of estimated ice-mass changes is determined using an ICESat-RACMO combination (Sec. 3.4.2). To solve for GIA and ice-mass changes, weighted least-squares adjustment is applied while taking into account the full noise covariance matrix of monthly GRACE gravity models as well as the variances of other datasets involved in the combination without using any additional constraints. The key advantages of using the dynamic patch approach in the combination are twofold: (1) it allows a consistent combination of GRACE data with data that feature higher spatial resolution with-

out yielding attenuation of their signal magnitude, and (2) it allows the derived GIA and ice-mass change signals to be more localized compared to the results derived in Ch. 2.

## 3.2. DATA SETS

In the time since the work described in Ch. 2 was conducted, the data sets used in the combination have undergone important improvements. The improved data from GRACE, ICESat and RACMO will be utilized in this chapter. Instead of using GPS data solely for the validation of the empirically derived GIA rates as it was done in Ch. 2, they will be used to define the pattern of estimated present-day GIA and are therefore implicitly incorporated into the combination. The time period under investigation is still restricted by the ICESat data and covers its entire mission period, from February 2003 to October 2009.

### 3.2.1. GRAVIMETRY

A relatively new GRACE gravity solution set has been developed at TU Delft (Farahani et al, 2016), called DMT2 (Delft Mass Transport model, release 2). These new DMT2 monthly solutions and their noise covariance matrices are complete to spherical harmonic degree 120. Modeling stochastic properties of the noise is essential especially when combining GRACE-derived data with data from other observational techniques. For DMT2, an accurate computation and incorporation of stochastic properties of colored noise was performed when processing K-Band Ranging (KBR) data that were in turn used to produce monthly solutions with corresponding noise covariance matrices (Farahani et al, 2016). The high accuracy and reliability of monthly noise covariance matrices of DMT2 was verified when DMT2-based optimally filtered linear trends were compared with other solutions in the literature to independent data and was found to outperform them in terms of spatial resolution (Farahani et al, 2016). Therefore, in this study DMT2 monthly solutions along with corresponding noise covariance matrices are used. For the combination approach, a linear trend based on unconstrained monthly DMT2 solutions is co-estimated along with bias, annual and S2 harmonic terms. Full covariance information was propagated into the trend. Degree one coefficients were added using values generated from the approach of Swenson et al (2008) (using RL05 GRACE data), and the  $C_{2,0}$  harmonics were replaced with those derived from satellite laser ranging (Cheng and Tapley, 2004).

### 3.2.2. ALTIMETRY

The latest release of ICESat data (R634) is used in this study, which includes the full ICESat timespan and the Gaussian correction (Borsa et al, 2013). Similar to the processing performed in Ch. 2, OFP shots that had a  $dh/dt$  greater than 12 m/yr were excluded, the campaign biases were computed using the LPZ in EA, a linear trend was estimated within 20x20 km area blocks, with the uncertainties determined by scaling the formal error from the least squares regression by the EVUW computed from the post-fit residuals. The EVUW scaled standard deviations were

computed here based on the number of independent shots (i.e. excluding individual shots that may be a part of more than one OFP) per cell (see [Felixson et al \(2017\)](#) for details of the new ICESat processing).

### 3.2.3. CLIMATE DATA

Surface mass balance estimates from RACMO2 with accompanying firn densification model (FDM) have been updated from version 2.1 to 2.3 by improving model physics ([Van Wessem et al, 2014](#)). RACMO2.3 estimates considerably wetter conditions in the interior of East Antarctica while WA remains almost unchanged from v2.1. When using the improved SMB and FDM data in the combination described in Ch. 2, the mass changes associated with GIA and in turn, ice-mass loss are estimated to be 20 Gt/yr larger in EA and almost unchanged in WA with 1 Gt/yr difference to previous estimates.

### 3.2.4. GPS

GPS observed uplift rates and corresponding uncertainties have been taken from [Thomas et al \(2011\)](#); [Groh et al \(2012\)](#); [Argus et al \(2014\)](#) and [Wolstencroft et al \(2015\)](#). If data at a GPS station were analyzed by more than one team, the uplift rates of the most recent study are used as they are expected to be reprocessed with state-of-the-art techniques. This yields 79 uplift rates for Antarctica.

To use GPS-derived uplift rates for defining the pattern of estimated present-day GIA, two important assumptions will be made. The first assumption is that GIA evolves at constant rates over decades meaning the time frames for the GPS trend analysis do not necessarily have to overlap with ICESat data, if elastic effects are accounted for (note that ICESat data determines the time span used for the combination). Elastic deformation is a response of the solid Earth to contemporary surface load variations. Before using GPS observations to constrain the estimated GIA pattern, they need to be corrected for elastic deformation. Elastic corrections are derived from the ICESat-RACMO combination to be consistent with data used in this analysis. The second assumption implies therefore that the linear trend based on the ICESat-RACMO combination is a sufficient approximation of the true variations in surface load over the time span considered here.

## 3.3. METHODOLOGY

In this section, a brief derivation of the patch approach ([Ran, 2017](#)) is introduced for completeness sake. To demonstrate the capability of the patch approach to recover a synthesized (noise-free) gravitational signal, a closed-loop simulation is performed. Different tuning parameters involved in the computation are described and established. Establishing them is important, since they might differ depending on the target area. An algorithm used for flexible patch definition is then introduced and its effectiveness is demonstrated by a simulation. Finally, the patch approach is combined with the empirical pointwise approach described in Ch. 2.

### 3.3.1. PATCH APPROACH

A patch is a bounded region on the Earth's surface with a uniform mass layer. Akin to [Baur and Sneeuw \(2011\)](#), gravity disturbances at satellite altitude are related in the functional model to the points on the Earth's surface, but here the surface mass layer representation of Earth's gravitational field is used instead of a point-mass approximation. This mass layer represents mass variations that occur over the patch (similar to mascons).

The potential anomaly  $V(\mathbf{p})$  caused by the surface density (i.e., mass per unit of area),  $q(\mathbf{p}')$ , distributed at the surface of the sphere  $S$  of radius  $r$ , is

$$V(\mathbf{p}) = G \iint_S \frac{q(\mathbf{p}')}{|\mathbf{p} - \mathbf{p}'|} dS(\mathbf{p}'), \quad (3.1)$$

where  $\mathbf{p}$  is an observation point,  $\mathbf{p}'$  is a source point, and  $G$  denotes the universal gravitational constant. Limiting to the space of piecewise constant single layer densities, where  $q_k$  is the layer density over patch  $S_k$ , yields

$$V(\mathbf{p}) \approx G \sum_{k=1}^K q_k \iint_{S_k} \frac{1}{|\mathbf{p} - \mathbf{p}'|} dS(\mathbf{p}'). \quad (3.2)$$

When approximating the integral in Eq. (3.2) by the weighted sum of the source points  $\mathbf{p}'$  within the integration domain

$$\iint_{S_k} \frac{1}{|\mathbf{p} - \mathbf{p}'|} dS(\mathbf{p}') \approx \sum_{j=1}^{J_k} \frac{1}{|\mathbf{p} - \mathbf{p}'_{kj}|} \Delta s_{kj}, \quad (3.3)$$

where the area elements  $\Delta s_{kj}$  serve as weights, the following expression can be used for the disturbing potential

$$V(\mathbf{p}) \approx G \sum_{k=1}^K q_k \sum_{j=1}^{J_k} \frac{1}{|\mathbf{p} - \mathbf{p}'_{kj}|} \Delta s_{kj} \quad (3.4)$$

with  $j = 1 \dots J_k$  and  $k = 1 \dots K$ . The area element  $\Delta s_{kj}$  is assigned to a node  $\mathbf{p}'_{kj}$ . For each patch,  $J_k$  can be different. It also follows that the sum of  $\Delta s_{kj}$  must be equal to the area of  $S_k$ .

Gravity disturbances,  $\delta g$ , can be expressed as the first derivative of the disturbing potential

$$\delta g(\mathbf{p}) \approx -\frac{\partial V}{\partial |\mathbf{p}|}(\mathbf{p}). \quad (3.5)$$

Since

$$-\frac{\partial}{\partial |\mathbf{p}|} \left( \frac{1}{|\mathbf{p} - \mathbf{p}'|} \right) = \frac{1}{|\mathbf{p} - \mathbf{p}'|^2} \frac{\partial}{\partial |\mathbf{p}|} |\mathbf{p} - \mathbf{p}'| = \frac{|\mathbf{p}| - |\mathbf{p}'| \hat{\mathbf{p}}^T \hat{\mathbf{p}}'}{|\mathbf{p} - \mathbf{p}'|^3} \quad (3.6)$$

with unit vectors  $\hat{\mathbf{p}}^T = \frac{\mathbf{p}}{|\mathbf{p}|}$  and  $\hat{\mathbf{p}}' = \frac{\mathbf{p}'}{|\mathbf{p}'|}$ , inserting Eq. (3.4) and Eq. (3.6) into Eq. (3.5) leads to

$$\delta g(\mathbf{p}) \approx G \sum_{k=1}^K q_k \sum_{j=1}^{J_k} \Delta s_{kj} \frac{|\mathbf{p}| - |\mathbf{p}'_{kj}| \hat{\mathbf{p}}^T \hat{\mathbf{p}}'_{kj}}{|\mathbf{p} - \mathbf{p}'_{kj}|^3}. \quad (3.7)$$

Expressed in spherical coordinates  $\mathbf{p}(r_i, \lambda_i, \varphi_i)$  and  $\mathbf{p}'(r, \lambda_j, \varphi_j)$ , Eq. (3.7) reads

$$\delta g_i \approx \sum_{k=1}^K \underbrace{q_k}_{x_k} G \underbrace{\sum_{j=1}^{J_k} \Delta s_{kj} \frac{r_i - r_{kj} \cos \psi_{kj,i}}{(r_{kj}^2 + r_i^2 - 2r_{kj}r_i \cos \psi_{kj,i})^{3/2}}}_{A_{ik}} \quad (3.8)$$

with angular distance  $\cos \psi_{kj,i} = \sin \varphi_{kj} \sin \varphi_i + \cos \varphi_{kj} \cos \varphi_i \cos(\lambda_i - \lambda_{kj})$ .

Finally, the gravity disturbances can be represented through the time-varying part of the spherical harmonic coefficients  $C_{nm}$  and  $S_{nm}$

$$\delta g_i = \frac{GM}{r_i^2} \sum_{n=2}^{n_{max}} \frac{n+1}{1+k_n} \left(\frac{a}{r_i}\right)^n \sum_{m=0}^n \bar{P}_{nm}(\sin \varphi_i) \cdot [C_{nm} \cos(m\lambda_i) + S_{nm} \sin(m\lambda_i)] \quad (3.9)$$

with  $GM$  being geocentric constant;  $a$  is the major semi-axis of a reference ellipsoid (WGS84 is used in this study);  $n$  and  $m$  is the spherical harmonic degree and order, respectively, with  $n_{max} = 120$ .  $\bar{P}_{nm}$  are normalized associated Legendre functions. The load Love numbers  $k_n$  account for the apparent mass change induced by Earth's elastic response to the loading of a surface mass. The spherical harmonic coefficients are GRACE Level-2 data products and are usually used to describe monthly gravity field solutions.

Equation (3.9) together with Eq. (3.8) represents the functional model for the patch-approach

$$y = Ax + e, \quad (3.10)$$

where gravity disturbances computed using Eq. (3.9) are stored in the vector of observations  $y$ . The right-hand side of Eq. (3.8) contains the design matrix  $A$  and the unknown surface densities  $q_k$  stored in parameter vector  $x$  in Eq. (3.10). As can be seen from Eq. (3.8), the design matrix  $A$  contains information regarding the geometry, e.g., data area, area of interest, shape and size of patches, as it relates the source points (with index  $k$ ) to the points at satellite altitude (with index  $i$ ). The vector of residuals is denoted as  $e$ . It is important to mention that each column of the design matrix needs to be filtered to ensure spectral consistency between the right and the left-hand side of the Eq. (3.10). This is necessary, since the gravity disturbances stored in  $y$  in Eq. (3.10) and corresponding variance-covariance information are spectrally limited up to a maximum degree, whereas the spectrum of the design matrix containing information regarding the geometry is unlimited (Ran, 2017). Filtering of the design matrix involves spherical harmonic analysis and synthesis that is described in more detail in the next section.

### SYNTHETIC CASE

To demonstrate the capability of the patch-approach, a synthetic case is computed. Surface densities (simulation input) are assigned per patch. This represents the true signal. This true signal is expanded in spherical harmonics (SHs). The SHs are evaluated by numerical integration. SH coefficients complete to degree 120 are then transformed to represent synthetic gravitational signal at satellite

altitude. The proposed methodology is used to recover the simulation input from the generated gravitational signal. To evaluate the performance of the patch approach, RMSE (root mean square error) is used, which is here the squared average difference between the simulated input and recovered output.

The major steps of the simulation are summarized in the flow diagram shown in Fig. 4.3 and are here described in detail. Each of the 27 basins defined by Zwally et al (2012) represents a patch. A GRACE-derived optimally filtered long-term trend (Siemes et al, 2013) in mm ewh is averaged over the 27 patches as shown in Fig. 3.3a. The resulting 27 values serve as input for the experiment. They represent the 'true' signal  $q_k$  with  $k = 27$  (Eq. 3.8). In the next step (Step 1 in Fig. 4.3), SH coefficients are computed as if they were GRACE Level-2 data products that will be used later. The conversion from spatial into spectral domain is called Spherical Harmonic Analysis (SHA) and is performed here using Gauss-Legendre Quadrature (GLQ) as described in Sneeuw (1994). The special feature of the Gauss-Legendre quadrature is the fact that it requires only  $L$  number of latitudes to perform an accurate global spherical harmonic analysis up to degree  $L - 1$ . For this, a global so-called 'Gauss-Neumann' (GN) grid is defined according to Sneeuw (1994), where latitude circles coincide with zeros of the Legendre polynomial of degree  $L + 1$  and meridians feature equiangular spacing with

$$\lambda_j = j\Delta\lambda \quad \text{with} \quad j = 0, 1, \dots, 2L - 1 \quad \text{and} \quad \Delta\lambda = \frac{\pi}{L}. \quad (3.11)$$

Applying GLQ yields more accurate zonal coefficients compared to an ordinary 2-D integration on a regular grid (Colombo, 1981). This is of particular importance in Antarctica which is located around the South Pole.

A global 0.01-degree GN grid is used in this experiment determining the amount of  $j$ -points in Eq. 3.8. If grid points lie within the boundaries of a particular patch, they get a corresponding surface density  $q_k$  assigned. Since a global grid is required, the values outside the AIS are set to zero (Fig. 3.3a). In this way generated global grid (longitude, latitude, surface density) is converted into Stokes coefficients  $C_{nm}^q$  and  $S_{nm}^q$  (Step 1 in Fig. 4.3). In Step 2 of Fig. 4.3,  $C_{nm}^q$  and  $S_{nm}^q$  representing surface density are converted into dimensionless SHs following Wahr et al (1998):

$$\left\{ \begin{array}{c} C_{nm} \\ S_{nm} \end{array} \right\} = \frac{3(1 + k_n)}{(2n + 1)a\rho_e} \left\{ \begin{array}{c} C_{nm}^q \\ S_{nm}^q \end{array} \right\} \quad (3.12)$$

using the density of Earth,  $\rho_e = \frac{3GM}{4\pi a^3 G}$ . The SH model is truncated at the degree 120 to be consistent with GRACE solutions produced at TU Delft (Farahani et al, 2016) that will be used later for the real-data case.

The dimensionless coefficients are then converted into pseudo-observations, i.e., gravity disturbances in space (see Eq. 3.9). The gravity disturbances are computed on a 1-degree GN grid (this determines the amount of  $i$ -points in Eq. 3.8) at 500 km altitude over the AIS including a buffer zone of 300 km width.

In the next step, the design matrix  $A$  is computed using Eq. (3.8). To ensure a spectral consistency between the data and the functional model, a lowpass filter is applied to the  $A$  matrix. For this, each column of the  $A$ -matrix can be treated as a

global set of gravity disturbances caused by one patch of unit surface density. In this experiment,  $k = 27$ . Therefore, for each of the 27 columns of the design matrix, SHA using GLQ is computed. SH model is truncated at the degree 120 ensuring spectral consistency with pseudo-observations  $\delta g$ . Spherical Harmonic Synthesis (SHS), i.e., conversion from the spectral to spatial domain, is then performed for each column of the  $A$ -matrix at the same point locations at which gravity disturbances are computed (Step 5 in Fig. 4.3).

In the final step, surface density per patch  $\hat{q}_k$  is estimated by means of a least-squares adjustment. Fig. 3.3b outlines the difference between the input  $q_k$  (shown in Fig. 3.3a) and the estimated output  $\hat{q}_k$ . As can be seen in Fig. 3.3b, comparison with the simulation input quantifies the error to be less than 0.1%. There are two main contributors to this error: cubature error and an error due to truncation of the SH expansion of a single patch at degree 120. Cubature is used to numerically compute the surface integral of the reciprocal distance contained in the functional model (Sec. 3.3.1). The higher the number of nodes  $J_k$  of a patch (Eq. 3.8) the smaller is the cubature error. Here the nodes were defined by the 0.01-degree GN grid to control this error. To minimize the error due to truncation of the SH expansion, the 'true' signal could have been generated to be smoother instead of featuring partially large differences between the signal over the AIS and the zero-signal behind the ice sheet. However, the SH expansion (Step 1 in Fig. 4.3) will not be applied to the real data, as GRACE Level-2 data products will be used. Moreover, a maximum error of less than 0.1% (Fig. 3.3b) is much smaller than the effect of data noise, hence, is negligible.

This experiment demonstrated that when using the patch approach to convert noise-free spherical harmonics into the spatial domain (Step 3-6), no leakage occurs. Note that surface densities have been recovered correctly despite the heterogeneity of the simulated input in West Antarctica. (To simplify the interpretation of surface density variations  $q_k$ , they are usually expressed in terms of equivalent water heights as e.g., in Fig. 3.3:  $h_k = \frac{q_k}{\rho_w}$  with  $\rho_w = 1000 \text{ kg/m}^3$  being the density of water).

### TUNING PARAMETERS

Depending on the grid used to define the nodes of the cubature formula and/or the locations of the data at satellite altitude, the performance of the patch approach may vary significantly and thus, needs to be investigated on a case-by-case basis. Worth investigating is also the size of data area (at satellite altitude) compared to the area of interest (on the Earth's surface). In the next experiments, these issues are addressed.

**Cubature error** Based on the above described experiment, the cubature error of less than 0.1% is considered to be negligibly small. Therefore, the corresponding design matrix is used to compute 'perfect' observations at satellite altitude according to Eq. (3.10). As this design matrix was computed using a 0.01-degree GN grid to define the nodes of the cubature formula and a 1-degree GN grid to define the locations of the data,  $A_{0,01}^1$  is used as shortened notation. The observa-

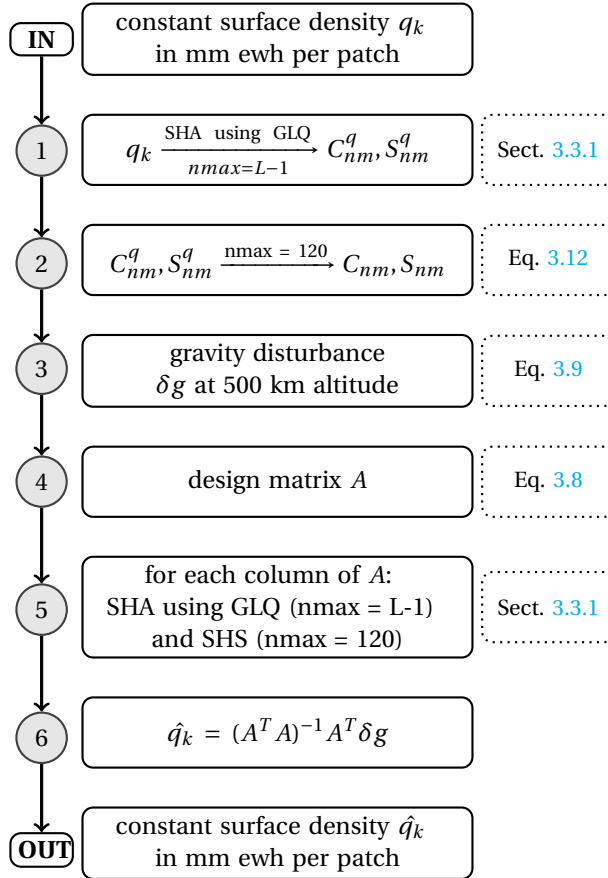


Figure 3.2: Flow diagram to summarize the major steps of the performed experimental setup.

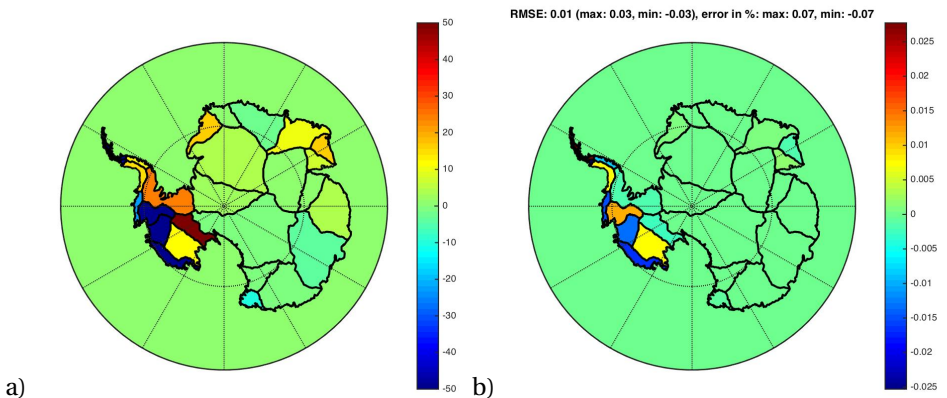


Figure 3.3: a) GRACE-trend in mm ewh averaged over the 27 basins defined by Zwally et al (2012) b) difference between the input (a) and the estimates in mm ewh. RMSE (root mean square error in mm ewh) is here the average difference between two vectors (input and output parameter vectors).



Figure 3.4: Antarctic drainage systems defined by Zwally et al (2012)

tions at satellite altitude are generated according to  $y_{0.01}^1 = A_{0.01}^1 q_k$  with  $q_k$  shown in Fig. 3.3a. In the next step, the design matrix is computed using different grids (0.02 and 0.05-degree GN grids) to define the nodes of the cubature formula. These design matrices ( $A_{0.02}^1$  and  $A_{0.05}^1$ ) are then used to estimate  $\hat{q}_k$  from  $y_{0.01}^1$ . The comparison with the simulation input quantifies the maximum error to be up to 0.9% and 1.1% when using 0.02 and 0.05-degree GN grids, respectively. These errors become smaller if the patches are made larger. Since a 1% error is still small, and the 0.05-degree case requires significantly less computational effort to generate, unless otherwise stated, any results presented in this manuscript going forward should be assumed to be defined on a 0.05-degree GN grid. However, one should keep in mind that the maximum cubature error can reach up to 1.1% when the minimum patch used for parameterization is ca. 30000 km<sup>2</sup> as it applies for basin 25 in Fig. 3.4.

**Resolution at the satellite altitude** Different grid resolution at satellite altitude was used (0.5, 1 and 1.5-degree GN grid) to investigate its impact on the solution. For all three experiments, spherical harmonics produced in Step 2 in Fig. 4.3 were used to generate the observations in space. The 0.05-degree GN grid is used to define the nodes of the cubature formula. The error between the estimate and simulation input for all cases does not differ significantly and reaches up to 1.1%. The error of 1.1% is the cubature error quantified above. Since the result indicate the independence of the spatial resolution of observations in space, the 1-degree grid is used to define the locations of the data in the further course of the manuscript.

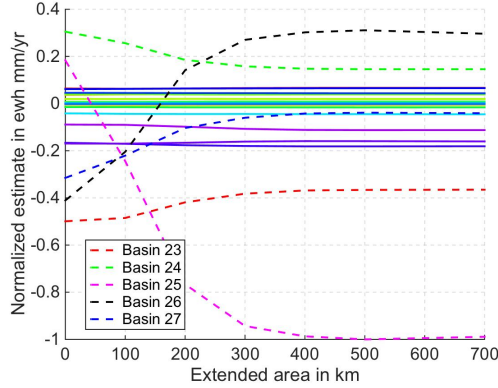


Figure 3.5: Dependence of estimated surface densities on the size of the data area. X-axis shows how much the data area extends beyond the area of interest. Surface densities are estimated for 27 basins defined by Zwally et al (2012) using unconstrained GRACE-derived trend and full noise covariance information produced at TU Delft. Solid lines represent normalized estimated surface densities for basins 1-22.

**Size of the data area** To obtain a sufficient estimate about how much the data area has to extend beyond the area of interest, real GRACE data with full noise covariances matrices were used. For this, a trend was co-estimated along with bias, annual and S2 harmonic terms over the ICESat time span (Feb. 2003 - Oct. 2009) using the DMT2 release produced at TU Delft. The colored noise of monthly GRACE solutions was propagated into the estimated trend. Both, the trend and the corresponding covariance matrix were first computed in the spectral domain and then propagated into the spatial domain in terms of gravity disturbance. Using the design matrix  $A_{0,05}^1$ , 27 single layer densities were estimated using different size of the data area. The result of this experiment is that the data area compared to the area of interest is always chosen to be 300 km larger. This is identified based on Fig. 3.5 which shows estimated surface densities for each of the 27 basins defined by Zwally et al (2012) depending on how much the data area was extended beyond the area of interest. Two conclusions can be made when analyzing Fig. 3.5. First, the estimates for larger basins (1- 22) seem to be independent of the size of the data area as they remain constant for all analyzed cases. Second, the surface density estimates for smaller basins 23-27 do not change significantly as soon the data area is chosen to be 300 km larger than the area of interest.

In the following sections, definition of patches, i.e., their shape and size, will be discussed as this is a critical factor in the proposed methodology.

### 3.3.2. PATCH DEFINITION

According to experiments performed above, it is evident that the performance of the patch approach is dependent on the geometry of the patches, or more specifically, on their size. Patches act as an inherent smoother on the data. Choosing a patch too small, will be critical to the stability of the solution. Choosing patches too

large might lead to a loss of information (oversmoothing). That means that patch definition is nothing else but a regularization by parameterization and therefore, must be performed carefully.

In this study, the focus is on separating GIA and ice-mass changes in Antarctica, so it seems obvious to incorporate geophysical information about mass changes associated with different processes into the patch definition. While the RACMO and altimetry data sets provide reliable evidence for the heterogeneity of the surface processes over the AIS, especially in the coastal areas, the spatial pattern of GIA signal over Antarctica is still not well understood. Antarctic GIA is believed to occur at large spatial scales (for instance, the GIA length scale was fixed to 1800 km in the data-driven inversion described in [Schoen et al \(2015\)](#)). This might be correct when considering GIA as a time-delayed response of the solid Earth to the Late-Pleistocene deglaciation, in the presence of a thick lithosphere and a high-viscosity mantle, as it should be the case of East Antarctica (EA). The problem is that West Antarctica (WA) is believed to have a thinner lithosphere and a lower mantle viscosity than EA ([van der Wal et al, 2015](#)) meaning that the solid Earth might respond much faster to ice-mass changes. Consequently, late Holocene ice-mass changes may dominate present-day GIA rates in such regions ([Nield et al, 2014, 2016](#)) yielding shorter spatial scales of GIA patterns. For the patch-definition algorithm this means that (1) it should be able to incorporate geophysical information about boundaries of the target regions, (2) the algorithm should be flexible in the way that patches of different sizes can be easily produced, and (3) no overlaps or gaps between the patches should occur. An algorithm encompassing these features is described in the next section.

#### VORONOI DECOMPOSITION (VD)

Voronoi decomposition (VD) is used to subdivide the area of interest into patches. VD is the partitioning of the plane into convex polygons based on the distance to the generating points. Fibonacci points serve here as generating points. Fibonacci points are evenly spaced points on a sphere ([González, 2010](#)). The distance between the neighboring Fibonacci points determines the resolution of an equal-area Fibonacci grid. In [Fig. 3.6a](#), a Fibonacci grid with 250 km distance between the points is shown. Based on the generated Fibonacci grid, a Voronoi Decomposition (VD) is performed. As a result, each convex polygon contains exactly one Fibonacci point and every point in a particular polygon is closer to its generating point than to any other ([Liebling and Pournin, 2012](#)). These convex polygons are called Voronoi cells ([Fig. 3.6b](#)).

In the example shown in [Fig. 3.6b](#), Voronoi decomposition is limited to the grounding line defined by [Zwally et al \(2012\)](#), which is the reason for the different geometry and, thus the area of the patches close to the grounding line. Because the Voronoi decomposition is based on an equal-area grid, the polygons in the interior of the ice sheet that do not contain the grounding line encompass almost identical areas.

It is a simple algorithm to partition the region of interest without introducing gaps or overlaps between the patches while taking into account the grounding line

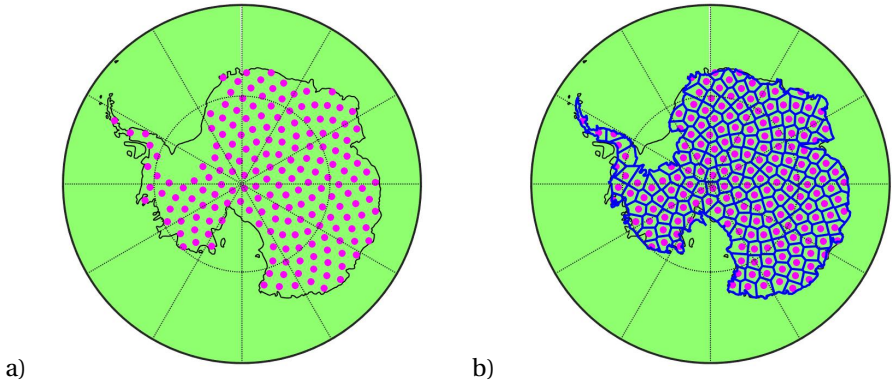


Figure 3.6: a) Fibonacci grid with 250 km distance between the Fibonacci points, (b) based on the Fibonacci grid in (a) Voronoi Decomposition (VD) limited to the AIS grounding line defined by Zwally et al (2012)

position or, generally speaking, the boundary of a target region. By varying the distance between the Fibonacci points, the size of produced patches varies. Therefore, the limited VD algorithm based on a Fibonacci grid fulfills all requirements for a patch-definition algorithm set in the previous section.

#### DYNAMIC PATCH DEFINITION

The limited VD algorithm based on a Fibonacci grid is a useful tool for defining patches. However, the larger the distance between the Fibonacci points the more discontinuous is the pattern of the estimated signal. Since the main objective of this study is deriving high-resolution spatial maps of the estimated signals in Antarctica, a dynamic patch approach is suggested. For this, patch boundaries are computed using different (dynamic) patch configurations yielding different estimates at the same node of the cubature formula. The average of the different estimates at each node represents the final solution. This means that if a range for Fibonacci grids is chosen to be between 300 and 400 km with spacing of 0.1 km, one thousand different configurations of patches (i.e., 300 km; 300,1 km; 300,2 km ... 400 km) are generated and used to compute one thousand different design matrices and in turn, one thousand GIA estimates. The mean of the thousand estimates at each node of the cubature formula (defined by the 0.05-degree GN grid) represents the final solution.

To show the capability of the dynamic patch approach to recover spatial pattern of a signal, a synthetic experiment is performed. The GIA model from Whitehouse et al (2012), abbreviated as W12a hereafter, is multiplied by 3700 kg/m<sup>3</sup> rock density (Riva et al, 2009) resulting in the surface densities shown in Fig. 3.7a. These surface densities represent a 'true' signal. In the next step, piecewise constant surface densities are generated based on the continuous 'true' signal using VD<sub>350</sub>-patches (Voronoi Decomposition applied to a Fibonacci grid that is generated using a 350 km distance between the Fibonacci points). This results in  $x_{VD350}$  shown in Fig. 3.7b. The discontinuous  $x_{VD350}$  is used to generate (noise-

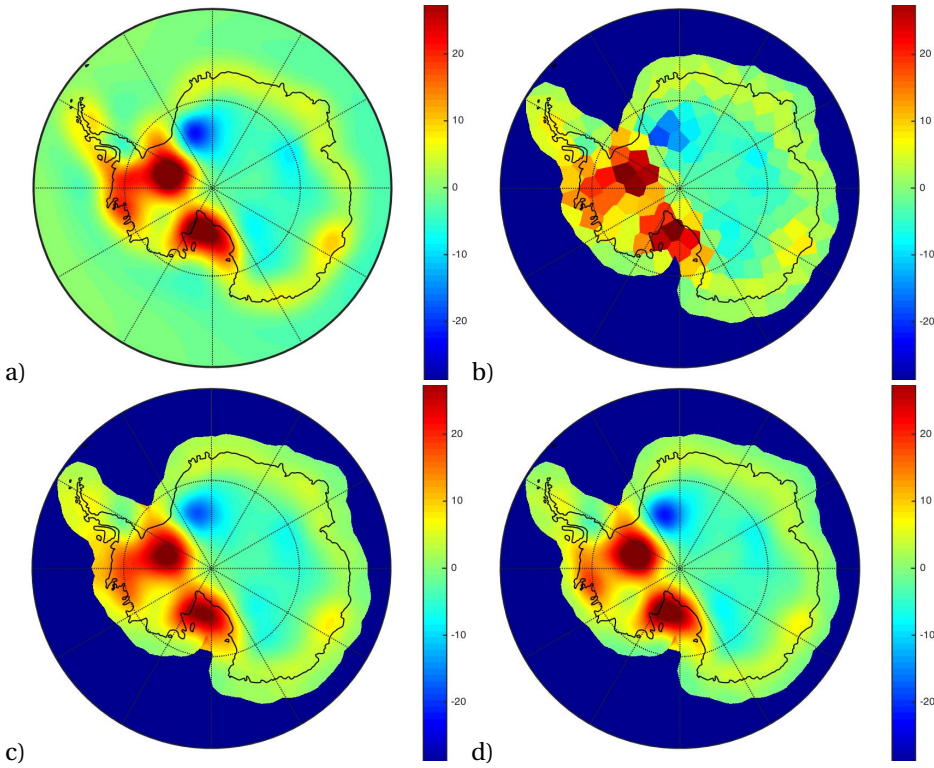


Figure 3.7: a) W12a GIA-model used as the 'true' signal. (b) Simulation input  $x_{VD350}$ : W12a GIA-model area-weighted averaged over patches that are produced using  $VD_{350}$  over the AIS including the 400 km extended area. These averages are used to generate observations  $\delta g_{VD350}$  at satellite altitude. Result when applying dynamic patch approach  $VD(300:0.1:400)$  to (c)  $\delta g_{VD350}$  and (d)  $\delta g_{VD101}$  (produced using  $VD_{101}$  instead of  $VD_{350}$ ).

free) pseudo-observations in space according to  $\delta g_{VD350} = A_{VD350} x_{VD350}$ . To note is that patches are defined over the AIS including 400 km offshore. The extended area of 400 km is used as GIA signal occurs beyond the grounded portion of the ice sheet as can be seen in Fig. 3.7a. The question is whether the dynamic patch approach can recover the continuous pattern of the 'true' signal when the generated pseudo-observations contain only its discontinuous information. To answer this question, different patches are defined using  $VD(300:0.1:400)$  and corresponding matrices ( $A_{VD300} \dots A_{VD400}$ ) are computed. The LSA is performed using one thousand different design matrices, whereby the vector of observations  $\delta g_{VD350}$  remains unchanged. As a result, the thousand estimates  $\hat{x}_{VD300} \dots \hat{x}_{VD400}$  are averaged at each node of the cubature formula defined by the 0.05-degree GN grid. The result is shown in Fig. 3.7c.

The result is encouraging as it nicely reproduces the W12a GIA pattern shown in Fig. 3.7a, although only a limited range of Fibonacci grids (300 - 400 km) was used to parameterize  $\delta g_{VD350}$ . The result shown in Fig. 3.7d recovers the con-

tinuous pattern of the 'true' signal considerably better than the result shown in Fig. 3.7c, since the simulation input in this case was computed over patches generated using  $VD_{101}$  instead of  $VD_{350}$ . Consequently, the observations in space, generated according to  $\delta g_{VD101} = A_{VD101} x_{VD101}$ , contain more information about the spatial pattern of the 'true' signal than  $\delta g_{VD350}$ . For real applications it means that the dynamic patch approach can recover continuous pattern of the estimated signal. When observations on the Earth's surface need to be projected into space, the smaller the patches used the more information about the spatial pattern is preserved. When using the dynamic patch approach, the spatial pattern of the estimated signal is not restricted to particular boundaries of the utilized patches. Additional simulations proved the result to be independent on the spacing used for the dynamic patch approach. That is, there was no significant difference between the results and corresponding uncertainties produced using 300:0.1:400 km range of Fibonacci grids and those produced using 300:1:400 km range of Fibonacci grids.

### 3.3.3. DYNAMIC PATCH APPROACH

In this Section, the approach presented in Ch. 2 is modified by using the patch approach. The key Eq. 2.3 of Ch. 2 is simplified as

$$\dot{h}_{\text{rock}} = \frac{\dot{m}_{\text{GRACE}} - \dot{m}_{\text{surf}^*}}{d} \quad (3.13)$$

where

$$\dot{m}_{\text{surf}^*} = (\dot{h}_{\text{ICESat}} - \dot{h}_{\text{firn}}) \cdot \rho_{\alpha} + \dot{m}_{\text{firn}} \quad (3.14)$$

represents the mass changes in the *surface* layer (ice + firn) and  $d = \rho_{\text{rock}} - \rho_{\alpha}$  is the denominator of Eq. 2.3. Please note that strictly speaking the term '*surface*' mass changes can only be properly used after  $\dot{h}_{\text{rock}}$  is also subtracted from ICESat derived height changes  $\dot{h}_{\text{ICESat}}$ . That is why a *surf*\* instead of *surf* label is used. Since ICESat is almost entirely sensitive to the surface mass changes, this approximated terminology seems adequate. From a computational point of view, the fact that ICESat theoretically observes the vertical rates related to GIA in addition to the surface processes, is accounted for by the fact that the density of ice/snow is used in the denominator in Eq. (2.3).

Essentially, the procedure here is the same as in Ch. 2. The signal mainly associated with surface processes is subtracted from the total signal observed from GRACE, but here in terms of gravity disturbances at the satellite altitude. The remainder represents signal associated with present-day GIA which is estimated on the Earth's surface using the dynamic patch approach and is converted to vertical deformation using the assumed rock density (or density difference between rock and ice/firn, if applicable). The derived GIA rates are then multiplied by the density of rock. The resulting empirical GIA mass change rates are then subtracted from the total signal observed from GRACE in terms of gravity disturbances after being projected into satellite altitude. The remainder represents signal due to ice mass changes (ice, firn) and is estimated on the Earth's surface using the dynamic patch approach.

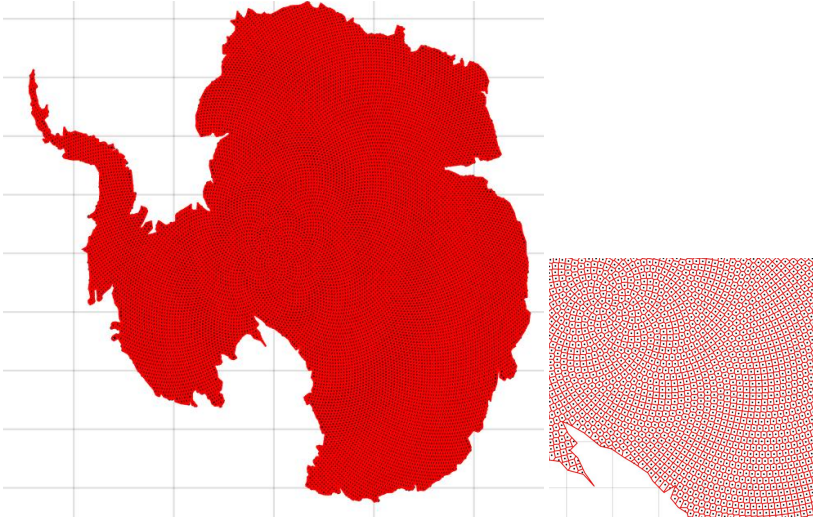


Figure 3.8:  $VD_{27}$  (Voronoi Decomposition applied to a Fibonacci grid that is generated using 27 km distance between the Fibonacci points) applied over the AIS. The inlet highlights boundaries of the generated patches (in red). Fibonacci points are in blue

To help explaining the algorithm of the dynamic patch approach, the major steps are summarized in the diagram shown in Fig. 3.9 and are here described in detail. First, surface mass changes  $\dot{m}_{\text{surf}}^*$  are computed as described in Ch. 2, but without applying Gaussian smoothing. In computations over the polar gap, only SMB from RACMO ( $\dot{m}_{\text{firn}}$ ) was used, as ICESat data are not available in this area and it is assumed that there are no ice dynamics taking place.

In the next step, gravity disturbances  $\delta \dot{g}_{\text{surf}}^*$  are computed representing the signal at satellite altitude mainly due to mass variations in the surface layer. For this, surface-layer patches are defined using  $VD_{27}$  (Voronoi Decomposition applied to a Fibonacci grid that is generated using 27 km distance between the Fibonacci points) over AIS only. Fig. 3.8 shows the geometry of the patches. The distance between the Fibonacci points is chosen to be 27 km, because it is the same as the spatial resolution of RACMO data used in the combination. These data have the lowest resolution in the computation of  $\dot{m}_{\text{surf}}^*$ . Mass changes in the surface layer are then area-weighted averaged over the surface-layer patches resulting in  $\dot{m}_{\text{surf}27}^*$ . After computing the design matrix  $A_{VD27}$  according to Eq. (3.8), the gravity disturbances at satellite altitude are calculated using Eq. (3.10) as

$$\delta \dot{g}_{\text{surf}}^* = A_{VD27} \dot{m}_{\text{surf}27}^* \quad (3.15)$$

The corresponding covariance matrix  $\Sigma_{\delta \dot{g}_{\text{surf}}^*}$  is computed according to

$$\Sigma_{\delta \dot{g}_{\text{surf}}^*} = A_{VD27} \Sigma_{\dot{m}_{\text{surf}27}^*} A_{VD27}^T \quad (3.16)$$

using the standard deviation of uncorrelated noise in the  $\dot{m}_{\text{surf}}^*$ . The  $\Sigma_{\dot{m}_{\text{surf}27}^*}$  is computed by applying the formal error propagation technique to Eq. (3.14) utiliz-

ing standard deviations described in Sec. 2.5.1 for each component of this equation.

To obtain gravity disturbances  $\delta\dot{g}_{\text{rock}^*}$  mainly due to mass variations in the GIA layer,  $\delta\dot{g}_{\text{surf}^*}$  is subtracted from the gravity disturbances  $\delta\dot{g}$  that represent the total GRACE signal

$$\delta\dot{g}_{\text{rock}^*} = \delta\dot{g} - \delta\dot{g}_{\text{surf}^*}. \quad (3.17)$$

The  $\delta\dot{g}$  are computed using Eq. (3.9). For this, unconstrained spherical harmonic solutions with full variance-covariance information produced at TU Delft are used. A linear trend was co-estimated along with bias, annual and S2 harmonic terms over the same time span as  $\hat{m}_{\text{surf}^*}$  (Feb. 2003 - Oct. 2009). The noise covariances of monthly GRACE solutions were propagated into the estimated trend. Both, the trend and the corresponding full noise covariance matrix were first computed in the spectral domain and then propagated into the spatial domain in terms of gravity disturbances. As a consequence, the covariance matrix of the  $\delta\dot{g}_{\text{rock}^*}$  is computed as

$$\Sigma_{\delta\dot{g}_{\text{rock}^*}} = \Sigma_{\delta\dot{g}} + \Sigma_{\delta\dot{g}_{\text{surf}^*}}. \quad (3.18)$$

After obtaining  $\delta\dot{g}_{\text{rock}^*}$ , the mass changes  $\widehat{m}_{\text{rock}^*}$  mainly associated with GIA signal can be estimated using the dynamic patch approach. For the least-squares estimate

$$\widehat{m}_{\text{rock}^*} = (A_{\text{rock}}^T \Sigma_{\delta\dot{g}_{\text{rock}^*}}^{-1} A_{\text{rock}})^{-1} A_{\text{rock}}^T \Sigma_{\delta\dot{g}_{\text{rock}^*}}^{-1} \delta\dot{g}_{\text{rock}^*}, \quad (3.19)$$

the design matrix  $A_{\text{rock}}$  that contains geometrical information about the patch distribution is required. As GIA might occur at large spatial scales, it must be parameterized beyond the grounded portion of the ice sheet as well. Therefore, 400 km beyond the AIS are additionally used to define patches for the GIA layer. The ocean mass changes are assumed to be negligibly small compared to the mass changes associated with GIA as discussed in Ch. 2. Since the data area must extend beyond the patches by 300 km (Sec. 3.3.1), it extends here by 700 km beyond the AIS. The dynamic patch approach is applied using VD(100:1:700), meaning that a wide range of Fibonacci grids (101 - 700 km) is used with 1 km spacing to define patches. After computing  $A_{\text{rock}_{\text{VD}101}} \dots A_{\text{rock}_{\text{VD}700}}$ , the 600 different  $\widehat{m}_{\text{rock}^*}$  were estimated with corresponding uncertainties

$$\Sigma_{\widehat{m}_{\text{rock}^*}} = (A_{\text{rock}}^T \Sigma_{\delta\dot{g}_{\text{rock}^*}}^{-1} A_{\text{rock}})^{-1}. \quad (3.20)$$

To get height changes  $\hat{h}_{\text{rock}}$  associated with GIA,  $\widehat{m}_{\text{rock}^*}$  must be divided by corresponding  $d$  according to Eq. 3.13. Therefore, area-weighted averages for  $d$  were computed over the patches that were used to parameterize GIA. As a result, the 600 estimates  $\hat{h}_{\text{rock}_{\text{VD}101-700}}$  are averaged at each node of the cubature formula defined by the 0.05-degree GN grid yielding  $\bar{h}_{\text{rock}}$ . To compute mass changes  $\bar{m}_{\text{rock}}$  associated with GIA, the  $\bar{h}_{\text{rock}}$  is multiplied by the density of rock (the same as in Ch. 2). The uncertainties in the estimated parameter  $\widehat{m}_{\text{rock}^*}$  (diagonal elements of the noise covariance matrix  $\Sigma_{\widehat{m}_{\text{rock}^*}}$ ) were propagated into  $\bar{m}_{\text{rock}}$  using formal error propagation technique in conjunction with uncertainties associated with  $d$  and the density of rock (Ch. 2).

Finally, the gravity disturbances due to mass variations in the surface layer  $\delta \dot{g}_{\text{surf}}$  can be calculated to estimate ice-mass changes  $\overline{\dot{m}}_{\text{surf}}$ . For this,  $\overline{\dot{m}}_{\text{rock}}$  is used to compute  $\delta \dot{g}_{\text{rock}} = A_{\text{rock}} \overline{\dot{m}}_{\text{rock}}$ . The corresponding standard deviations are propagated as

$$\Sigma_{\delta \dot{g}_{\text{rock}}} = A_{\text{rock}} \Sigma_{\overline{\dot{m}}_{\text{rock}}} A_{\text{rock}}^T. \quad (3.21)$$

To transfer as much information as possible of the estimated signal into gravity disturbances at satellite altitude, the design matrix computed for the smallest patches (based on VD<sub>27</sub>) is used. After subtracting  $\delta \dot{g}_{\text{rock}}$  from the total GRACE signal  $\delta \dot{g}$ , the remaining  $\delta \dot{g}_{\text{surf}}$  is used to estimate ice-mass change rates by using least-squares:

$$\widehat{\dot{m}}_{\text{surf}} = (A_{\text{surf}}^T \Sigma_{\delta \dot{g}_{\text{surf}}}^{-1} A_{\text{surf}})^{-1} A_{\text{surf}}^T \Sigma_{\delta \dot{g}_{\text{surf}}}^{-1} \delta \dot{g}_{\text{surf}} \quad (3.22)$$

with

$$\Sigma_{\delta \dot{g}_{\text{surf}}} = \Sigma_{\delta \dot{g}} + \Sigma_{\delta \dot{g}_{\text{rock}}}. \quad (3.23)$$

Similarly to defining patches for the GIA layer, different Fibonacci grids spanning the range between 101 and 700 km are used to define patches and in turn, to compute design matrices  $A_{\text{surfVD101}} \dots A_{\text{surfVD700}}$ , but this time the patches are defined over the grounded portion of the ice sheet only. This is an extremely advantageous feature of the patch-approach, since mass variations associated with surface processes can be pinpoint instead of leaking into the ocean assuming the GIA is estimated correctly.

## 3.4. RESULTS

Following the steps described in Sec. 3.3.3, combination results associated with GIA are shown and discussed in Sec. 3.4.1. Corresponding results associated with ice-mass changes are subject of Sec. 3.4.2. Combination results are summarized in Sec. 3.4.3 and discussed in Sec. 3.4.4.

### 3.4.1. GIA ESTIMATES

The estimated GIA height changes corrected for LPZ bias (as in Ch. 2) in mm/yr are shown in Fig. 3.10. Although a dynamic patch approach using VD(101:1:700) has been tested, only the results starting from VD<sub>250</sub> are shown. This is done, because the signal content of results produced using VD(101:1:250) is considerably lower than their noise content. Since patch definition is a regularization by parameterization, examining how the spatial pattern and the magnitude of the estimates evolves over different patch sizes is necessary to avoid oversmoothing and thus, to find a preferable patch definition. For this, the wide range of Fibonacci grids used for the dynamic patch definition is subdivided using a sliding window width of 100 km with a sliding increment of 50 km yielding 8 GIA estimates for VD(250:1:700) displayed in Fig. 3.10. The sliding window width of 100 km is sufficient to produce reasonable estimates, since experiments based on synthetic data have shown the results are nearly independent of whether 100 or 1000 realizations were computed within the same range of Fibonacci grids used to define patches. The 50 km wide

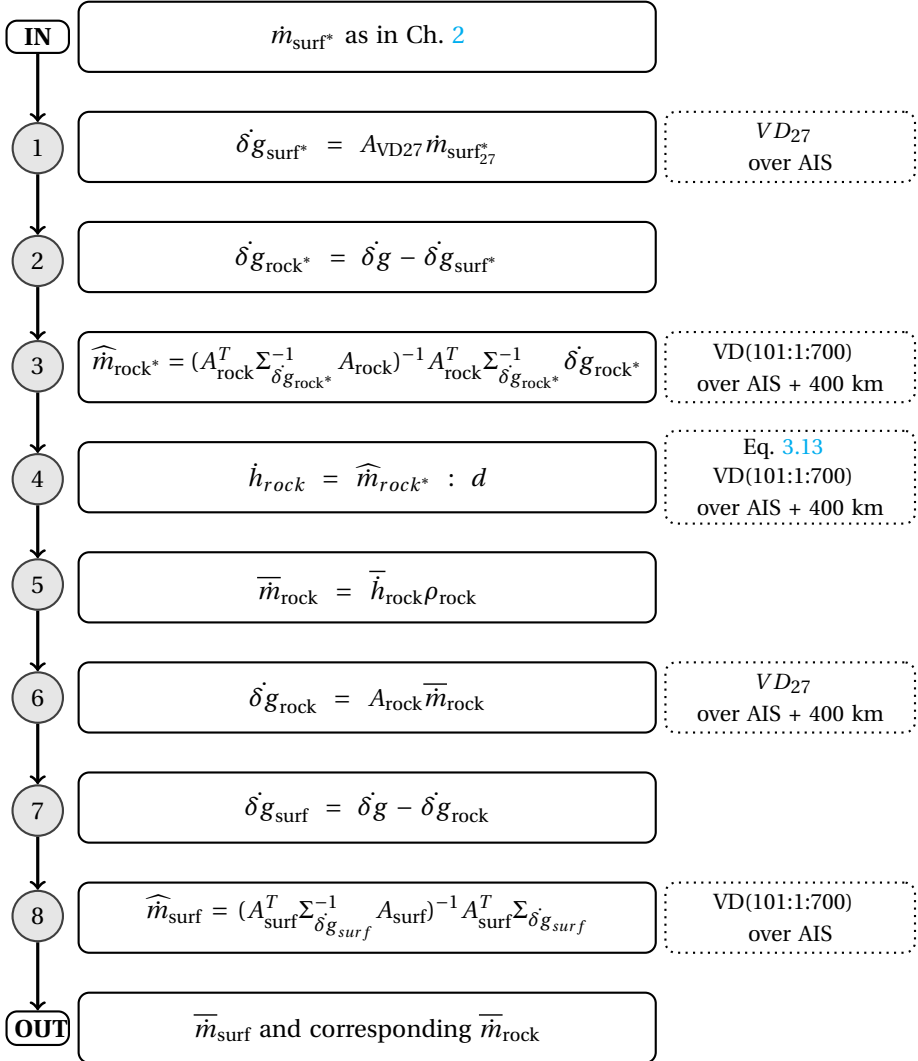


Figure 3.9: Flow diagram to summarize the major steps of the dynamic patch approach

Table 3.1: The properties associated with the estimated GIA rates depending on the range of Fibonacci grids used for parameterization

AIS Est. Mass Change in Gt/yr		in mm/yr			GPS-comparison			Fibonacci distance
mass-LPZ bias	$1\sigma$	LPZ-bias	$\max(\dot{h}_{\text{rock}})$	$\min(\dot{h}_{\text{rock}})$	WRMS	D	DWRMS	range
136	213	0.2	51.2	-40.7	8.8	-0.1	8.8	250-350
132	70	0.1	32	-17	7.5	1.8	7.3	300-400
130	34	0.1	30	-15	6.1	1.9	5.8	350-450
123	20	0.1	25	-11	4.4	0.7	4.3	400-500
115	14	0.2	18	-11	3.7	-0.2	3.7	450-550
110	10	0.2	20	-12	3.7	-0.6	3.6	500-600
106	8	0.2	20	-12	3.7	-0.7	3.6	550-650
102	7	0.2	14	-11	3.7	-0.8	3.6	600-700

sliding increment was used, because it leads to estimates that are sufficiently different, but still within  $1\sigma$  range of corresponding uncertainties (Tab. 3.1).

In Fig. 3.10, the prominent GRACE features are clearly observable: the higher the spatial resolution (the smaller patches used for parameterization), the higher the noise content and corresponding standard deviation (Tab. 3.1). It is also known that removal of noise (using larger patches for parameterization) might be accompanied by signal distortion. To decide which range of Fibonacci grids should be used to define patches for obtaining a preferred GIA solution, independent GPS observations at 79 stations are used (circles in Fig. 3.10). At these GPS sites, 8 sets of estimated GIA rates are compared to the elastic-corrected GPS-derived present-day uplift rates (Fig. 3.10 and Tab. 3.1). A GIA solution is regarded as a preferred one when its estimated rates at the GPS sites best fit the corresponding elastic-corrected GPS vertical rates. The agreement is analyzed in terms of the weighted root-mean-square of the residuals (WRMS) between the estimated vertical rates and those observed at the GPS stations (using Eqs. 2.5 and 2.6).

The properties associated with the estimated GIA rates are summarized in Tab. 3.1 depending on the range of Fibonacci grids used for parameterization. Based on the results, the GIA-estimates shown in Fig. 3.10e using VD(450:1:550) are regarded as preferred with one of the lowest WRMS of 3.7 mm/yr between the estimated GIA rates and those observed from GPS. Bias-corrected WRMS (DWRMS) is also 3.7mm/yr for this range of Fibonacci grids used to define patches. For larger patches, WRMS and corresponding DWRMS are not changing significantly. Note that the uncertainties for both the GPS and GIA uplift rates are used in the calculations. It is interesting to mention that when using VD(450:1:550) to parameterize GIA, the systematic bias D between estimated GIA rates and those observed from the GPS stations is almost zero mm/yr and thus one of the smallest (in an absolute sense) in Tab. 3.1.

### 3.4.2. ICE-MASS CHANGE ESTIMATES

After the present-day GIA spatial pattern with corresponding signal magnitude has been estimated, Steps 5-8 in Fig. 3.9 are performed yielding 11 ice-mass change estimates  $\bar{m}_{\text{surf}}$  for the range of VD(101:1:700) (when using a sliding window width

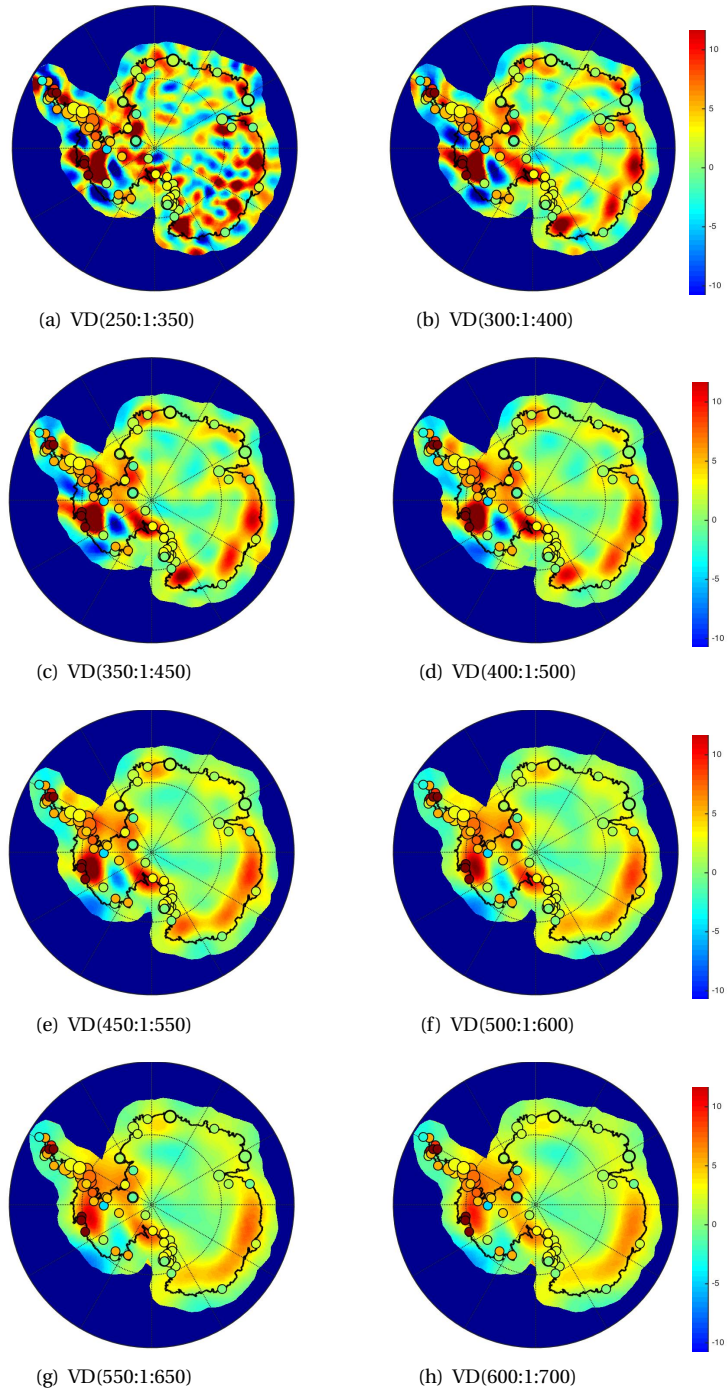


Figure 3.10: Estimated present-day GIA rates  $\bar{h}_{\text{rock}}$  corrected for LPZ bias in mm/yr using different patch configurations for parameterization.  $\bar{h}_{\text{rock}}$  are overlain by observed elastic-corrected vertical rates at the 79 GPS sites (circles).

of 100 km with a sliding increment of 50 km as described in previous section). To help decide which range of patches is the preferred one for estimating ice-mass changes, ICESat-RACMO combination  $\dot{m}_{\text{surf}^*_{27}}$  is used. Although  $\dot{m}_{\text{surf}^*_{27}}$  is not corrected for GIA uplift rates and is not an independent dataset, it provides a good reference of the spatial pattern of surface processes. Before comparing differently parameterized ice-mass change estimates  $\overline{\dot{m}}_{\text{surf}}$  with  $\dot{m}_{\text{surf}^*_{27}}$ , the latter undergoes a similar procedure as GRACE-derived observations to ensure a fair comparison. That means that gravity disturbances  $\delta g_{\text{surf}^*}$ , which are computed at satellite altitude in Step 1 in Fig. 3.9, are used as pseudo-observations to estimates  $\overline{\dot{m}}_{\text{surf}^*}$ . The  $\overline{\dot{m}}_{\text{surf}^*}$  is parameterized in the same way as ice-mass change estimates derived from the full combination (i.e., GRACE-ICESat-RACMO) yielding 11  $\overline{\dot{m}}_{\text{surf}^*}$  estimates.

To understand how the patch approach affects the high-resolution ICESat-RACMO combination, the corresponding auxiliary results are analyzed first. Fig. 3.11 illustrates the ICESat-RACMO combination  $\dot{m}_{\text{surf}^*_{27}}$  in Fig. 3.11a. The uncertainties are shown in Fig. 3.11b. The input mass changes  $\dot{m}_{\text{surf}^*_{27}}$  computed over AIS amount to -190 Gt/yr. Figures 3.11c-d show ICESat-RACMO-based estimates  $\overline{\dot{m}}_{\text{surf}^*}$  after applying the patch-approach when VD(150:1:250) is used for parameterization. The range of 150-250 km is used as an example. When an ordinary least-squares estimator is used (weight matrix is the identity matrix), the mass changes computed over the AIS amount to -190 Gt/yr (Fig. 3.11c). When a weighted least-squares solution is computed (using  $\Sigma \dot{m}_{\text{surf}^*_{27}}$ ), the mass changes integrated over the AIS amount to -90 Gt/yr (Fig. 3.11d). Although the amount of mass is fully recovered when using the 'error-free' patch approach, the result is still noisy (Fig. 3.11c). When the patch approach considers the covariance matrix computed using Eq. 3.16, the noise is suppressed and observations exhibiting large standard deviations are down-weighted yielding a lower mass loss over AIS. In other words, the patch approach acts as a statistical filter that uses (full) variance-covariance matrix and does not require any a priori information regarding the magnitude of the estimated signal. The objective function to be minimized is simply the weighted sum of squared residuals. If statistical information is not considered, the patch approach along with its dynamic patch definition acts as a smoother reducing the spatial resolution, but preserving the total signal content.

When choosing an optimal ice-mass change estimate  $\overline{\dot{m}}_{\text{surf}}$  from the full combination (i.e., GRACE-ICESat-RACMO), differently parameterized  $\overline{\dot{m}}_{\text{surf}}$  are compared to differently parameterized  $\overline{\dot{m}}_{\text{surf}^*}$ . The dynamic patch approach is applied to ICESat-RACMO-combination  $\overline{\dot{m}}_{\text{surf}^*}$  preserving the total signal content.

As a criterion for similarity, RMS reduction in percent

$$R = 100 \cdot \left( \frac{RMS_{\overline{\dot{m}}_{\text{surf}}} - RMS_{\overline{\dot{m}}_{\text{surf}} - \overline{\dot{m}}_{\text{surf}^*}}}{RMS_{\overline{\dot{m}}_{\text{surf}}}} \right) \quad (3.24)$$

following [Tesmer et al \(2011\)](#) is computed considering the entire ice sheet as a time series. RMS signal reductions in percent for the range of VD(150:1:700) are shown in Tab. 3.2.

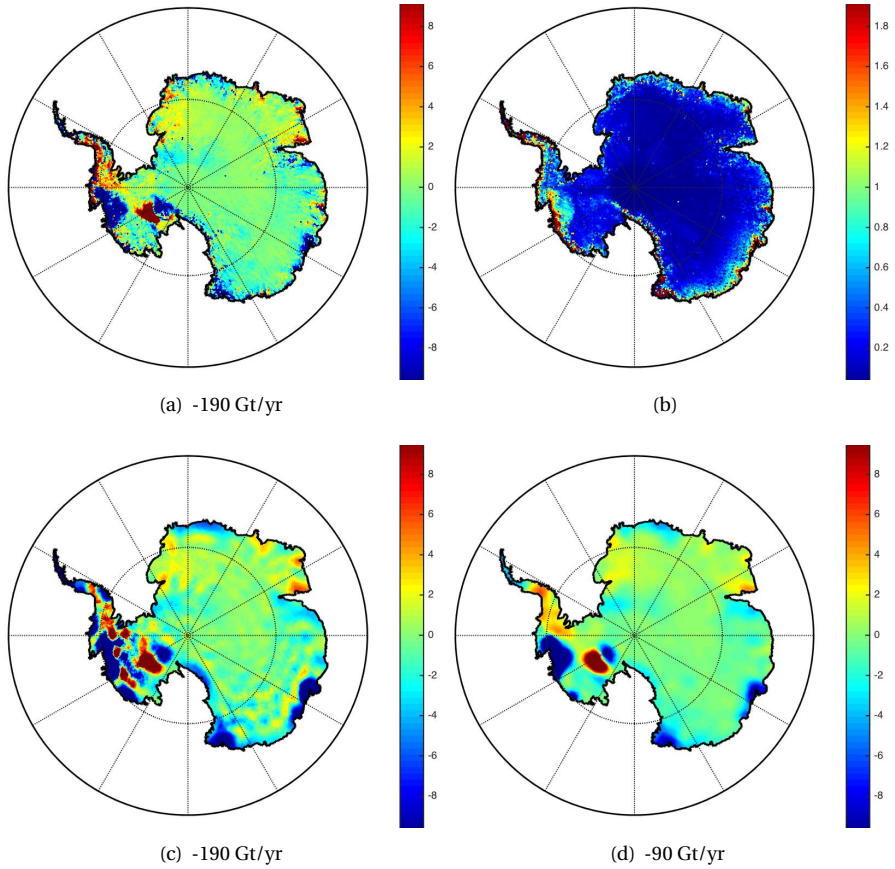


Figure 3.11: (a)  $\bar{m}_{\text{surf}^*}$  being the area-weighted average over VD<sub>27</sub>-patches and (b) corresponding uncertainties. (c-d) Patch-approach applied on (a) using VD(150:1:250). In (c) patch approach estimates using ordinary least-squares; in (d) patch approach estimates using weighted least-squares. Results are in cm/yr ewh.

Table 3.2: Reduction in percent of estimated ice-mass changes  $\bar{m}_{\text{surf}}$  (computed from the full combination GRACE-ICESat-RACMO) by  $\bar{m}_{\text{surf}^*}$  (ICESat-RACMO combination) for different range of Fibonacci grids used for parameterization.

$\bar{m}_{\text{surf}^*}$ \ $\bar{m}_{\text{surf}}$		Range of Fibonacci grids in km used for patch definition									
		150:250	200:300	250:350	300:400	350:450	400:500	450:550	500:600	550:650	600:700
150:250		0	0	0	0	0	0	0	0	0	0
200:300		31	38	29	23	22	20	18	15	12	10
250:350		31	56	61	51	47	42	38	32	26	22
300:400		12	37	64	70	66	60	52	43	35	30
350:450		-8	15	46	63	70	66	58	50	41	34
400:500		-22	0	32	49	61	63	60	56	46	38
450:550		-39	-17	15	33	45	52	59	61	52	43
500:600		-58	-34	-1	18	31	42	57	65	59	49
550:650		-78	-54	-19	0	14	27	47	62	64	56
600:700		-96	-69	-32	-12	2	16	38	57	64	60

Table 3.3: Reduction in percent of estimated ice-mass changes  $\overline{m}_{\text{surf}}$  (computed from the full combination GRACE-ICESat-RACMO) by  $\overline{m}_{\text{surf}}^*$  (ICESat-RACMO combination) for different range of Fibonacci grids used for parameterization.

		Range of Fibonacci grids in km used for patch definition					
		300:400	310:410	320:420	330:430	340:440	350:450
$\overline{m}_{\text{surf}}$	$\overline{m}_{\text{surf}}^*$	69.8	69.3	68.7	67.7	67.3	66.2
300:400		69.8	69.3	68.7	67.7	67.3	66.2
310:410		70.8	71.5	71.2	70.5	70.1	69.2
320:420		71.4	72.6	73.0	72.5	72.1	71.5
330:430		69.7	71.5	72.4	72.4	73.0	72.7
340:440		65.0	66.8	67.8	68.7	70.5	70.3
350:450		62.7	64.9	66.3	67.6	69.6	70.2

About 70% of the ice-mass change variance  $\overline{m}_{\text{surf}}$  (estimated from the full combination GRACE-ICESat-RACMO) can be explained by  $\overline{m}_{\text{surf}}^*$  (ICESat-RACMO combination). This agreement is obtained when both signals are parameterized using VD(300:1:400) or VD(350:1:450). The geographical plots of ice-mass change estimates parameterized using VD(250:1:700) are shown in Fig. 3.12. When examining the result obtained using VD(300:1:400) shown in Fig. 3.12b, it seems that this solution exhibits a great spatial resolution compared to the spatial maps of surface processes shown in Fig. 3.11, but contains too much noise in the interior of EA. On the other hand, the solution obtained using VD(350:1:450) shown in Fig. 3.12c seems to be already oversmoothed, as the geographical location and magnitude of prominent features such as glacial thickening in Kamb Ice Stream with mass loss in its direct proximity are not properly detected. In the next step therefore, sliding increment of 10 km for the range of VD(300:1:450) is analyzed with corresponding RMS signal reductions summarized in Tab. 3.3.

Because the maximum similarity between the  $\overline{m}_{\text{surf}}^*$  and  $\overline{m}_{\text{surf}}$  is achieved when both are parameterized using the range of 320-420 km Fibonacci grids, this parameterization is regarded as a preferred one to parameterize Antarctic ice-mass changes. Fig. 3.13 visualizes the corresponding findings.

### 3.4.3. COMBINATION RESULTS

A range of different solutions based on different patch configurations has been estimated for the signal associated with GIA and ice-mass changes. Independent GPS observations helped decide that the range of patches based on 450-550 km Fibonacci grids is the most suitable for parameterizing Antarctic GIA signal. After subtracting the estimated GIA from the full GRACE-signal at satellite altitude, ice-mass changes are parameterized using different patch configurations. The most suitable parameterization for ice-mass changes is determined to be the range of patches based on 320-420 km Fibonacci grids. This parameterization yields the best fit between the combination results with the auxiliary results derived by applying dynamic patch approach to the ICESat-RACMO combination. The geographical plots of the results are shown in Fig. 3.14 with the corresponding mass change values summarized in Tab. 3.4. Please note that ice-mass change value is not derived as in Ch. 2 by simply subtracting a value for estimated GIA-mass change rate from the total mass change estimated from GRACE. When using the

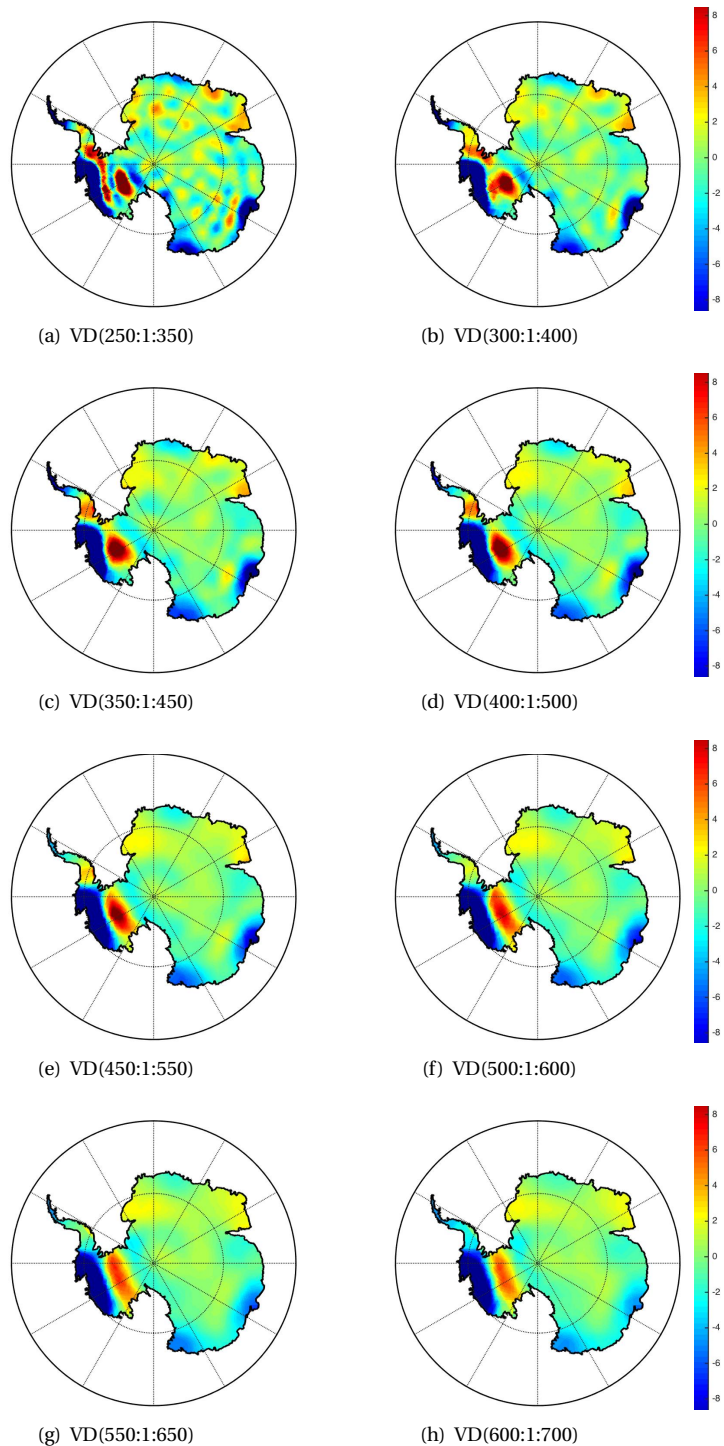


Figure 3.12: Ice-mass change estimates  $\overline{m}_{\text{surf}}$  corrected for LPZ bias using different patch configurations for parameterization. Results are in cm/yr ewh.

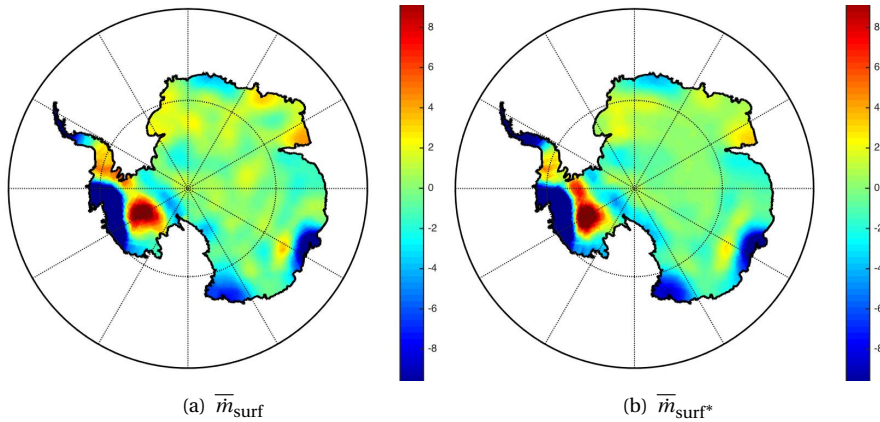


Figure 3.13: Surface mass change estimates in cm/yr ewh parameterized by VD(320:1:420): (a) full combination results (GRACE-ICESat-RACMO), (b) ICESat-RACMO combination results.

Table 3.4: Estimates of the mass change components computed over the grounded ice sheet. Uncertainties are  $1\sigma$ .

	Estimated mass change rates(Gt/yr)						LPZ-bias	
	GIA			Ice-mass			GIA	Ice-mass
	EA	WA	AIS	EA	WA	AIS	mm/yr	mm/yr EWH
	85	30	115	-45	-98	-143	0.2	-2.6
Est. Uncertainties	13	3	14	35	5	36		

suggested patch approach, both GIA and ice-mass changes are parameterized using different geophysical boundaries and different dynamic patch configurations without estimating the total GRACE mass change on the Earth's surface. Low-precipitation zone (LPZ) calibration is performed here as in Ch. 2 by computing and subtracting a LPZ bias (Tab. 3.4) from the estimated GIA and ice-mass change rates before integrating them over the AIS.

Figures 3.14c-d display geographical plots of the standard deviation of noise in the estimated rates associated with GIA and ice-mass changes. It can be observed that for both estimates the latitude-dependent GRACE errors dominate the combination results. This is likely due to the fact that the full noise covariance matrix of the GRACE-derived trend is incorporated while only the main diagonal of the ICESat-RACMO combination is used. Since the spatial correlations of the ICESat-RACMO combination are not available, it could be argued that for the sake of consistency only the main diagonal of the GRACE related covariance matrix should be used within the combination. However, neglecting the correlation of noise in GRACE data leads to more 'stripes' in the estimated signal maps and higher uncertainty of the derived estimates, as illustrated in Fig. 3.15, emphasizing the importance of a full noise description.

Examining again the results that consider the full noise covariance matrix of

3

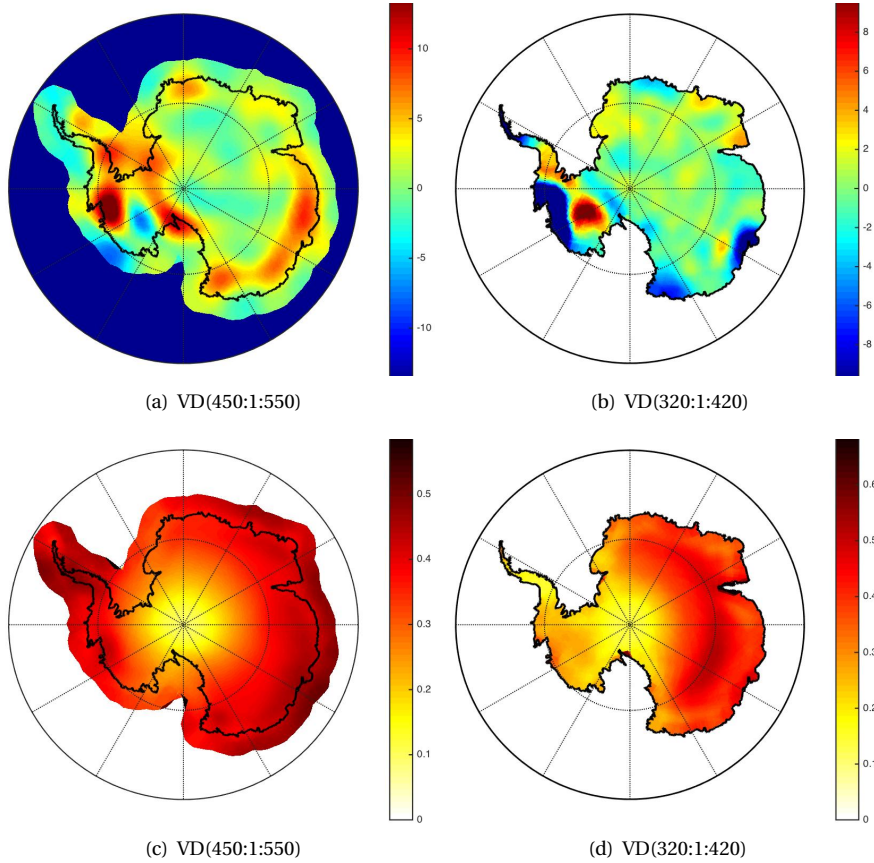


Figure 3.14: Estimates (a, b) and uncertainties (c, d) for the estimated GIA rates (a, c) in mm/yr and ice-mass change rates (b, d) in cm/yr ewh

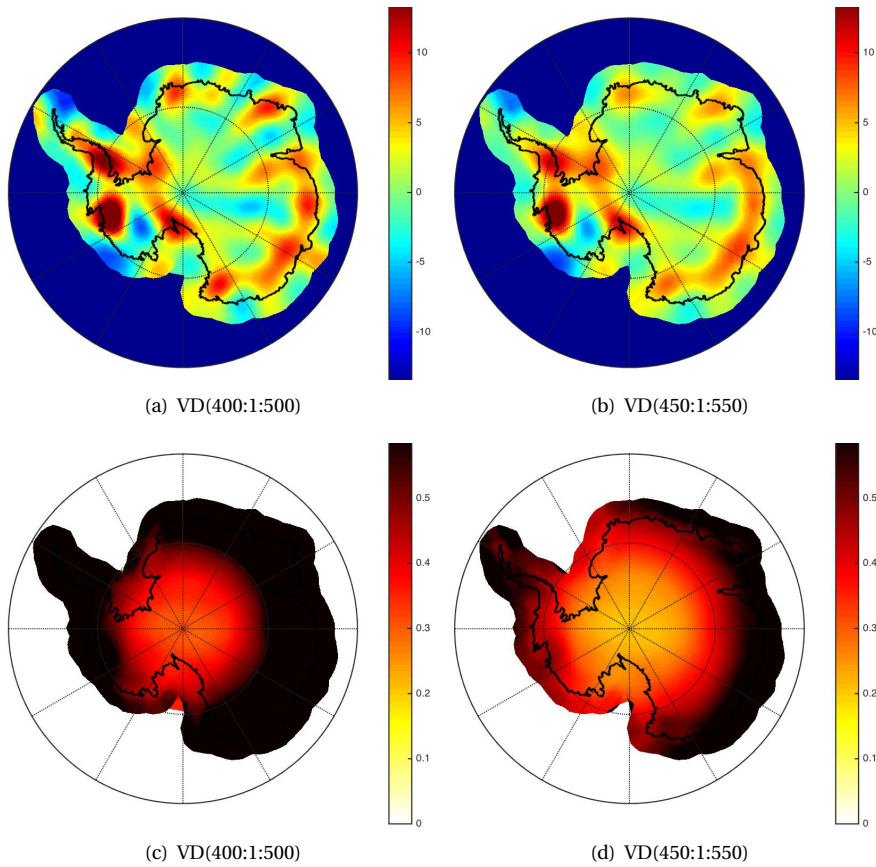


Figure 3.15: Estimates (a, b) and corresponding uncertainties (c, d) for the estimated GIA rates in mm/yr when only the main diagonal of noise covariance matrix of GRACE data is used.

Table 3.5: Estimates of the ice-mass changes in Gt/yr and corresponding uncertainties computed over the grounded ice sheet. Uncertainties are  $1\sigma$ .

AIS		WA		EA		Fibonacci
mass	$1\sigma$	mass	$1\sigma$	mass	$1\sigma$	distance in km
-157	134	-102	15	-55	133	250:1:350
-149	49	-99	6	-50	49	300:1:400
-143	36	-98	5	-45	35	320:1:420
-134	24	-96	3	-39	23	350:1:450
-130	15	-93	2	-37	15	400:1:500
-125	10	-89	2	-37	10	450:1:550
-117	7	-82	1	-34	7	500:1:600
-113	6	-80	1	-33	6	550:1:650
-115	5	-82	1	-33	5	600:1:700

the GRACE-derived trend, it is obvious that the largest uncertainties associated with the estimated GIA over the grounded AIS (Fig. 3.14c) are in the areas most expected, such as Antarctic Peninsula (AP) and Amundsen Sea sector (ASE) in WA and the most coastal regions in EA (Oates Land, Wilkes Land and Enderby Land). This also correlates with the regions of highest uncertainty in the ICESat-RACMO combination shown in Fig. 3.11b. The uncertainties associated with the estimated ice-mass changes (Fig. 3.14d), however, do not correlate with the regions of highest uncertainty in ICESat-RACMO combination. Moreover, signal estimated in the AP seems to be perfectly resolved compared to the relatively high uncertainties in EA. To find a reason for this unexpected pattern, the noise standard deviations of the estimated ice-mass changes are shown for the case when larger patches are used for parameterization (Fig. 3.16). Despite the fact that the uncertainties become in general smaller when larger patches are used, the noise standard deviations in AP do not differ significantly from those over EA anymore (Fig. 3.16). This behavior could be explained by the fact that when smaller patches are used to parameterize ice-mass changes, the noise level in GRACE data is much higher than the noise standard deviations associated with the estimated GIA. When larger patches are used to parameterize ice-mass changes, the noise level in GRACE data becomes smaller or comparable with the noise level of the derived GIA (which was parameterized using VD(450:1:550)). Table 3.5 summarizes ice-mass change values in Gt/yr and corresponding uncertainties computed over the grounded AIS, EA, and WA depending on the different patch configurations used to parameterize the estimated signal.

By analyzing results summarized in Tables 3.1, 3.4, and 3.5, it can be concluded that the proposed dynamic patch approach estimates preferred GIA rates with higher certainty than the preferred high-resolution ice-mass change rates due to the limited horizontal GRACE resolution. However, the developed methodology is capable of obtaining high-resolution ice-mass changes with reasonable uncertainties (Tab. 3.5). The largest uncertainties are determined over EA, due primarily to the much larger surface area involved.

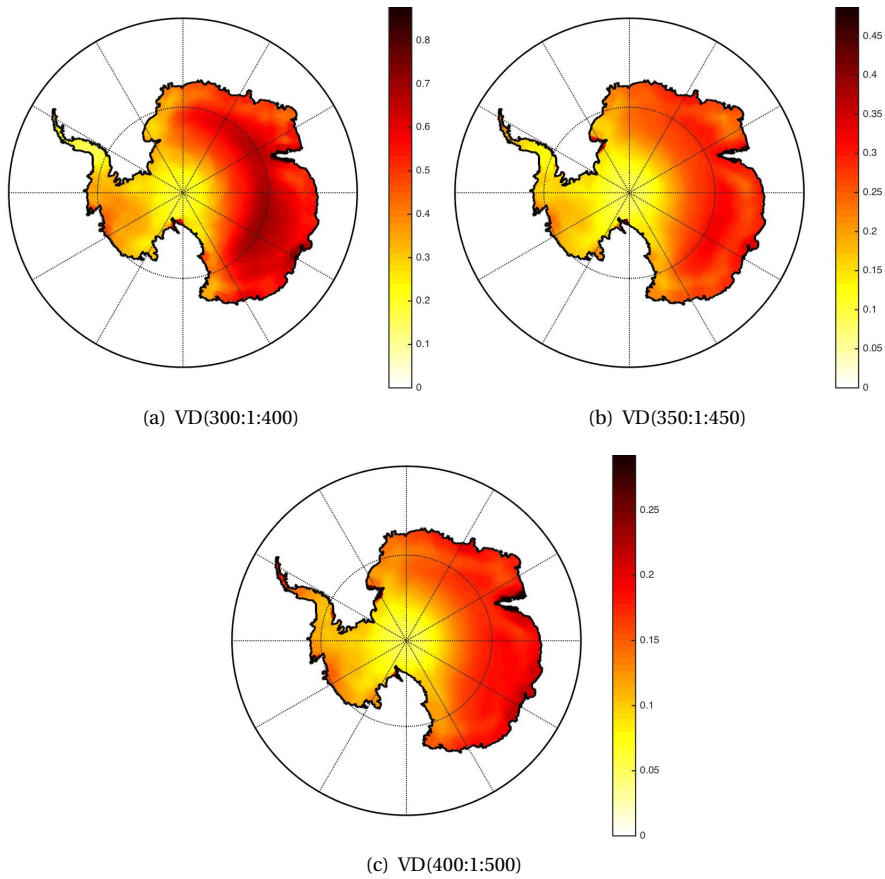


Figure 3.16: Uncertainties for differently parameterized ice-mass change rates in cm/yr ewh. Note, that different scales are used.

#### 3.4.4. DISCUSSION

To analyze how the proposed patch approach affects the derived GIA and ice-mass change estimates over the AIS, the results derived in Ch. 2 are compared to those derived in this chapter. As 10 different GIA fields were estimated in Ch. 2, constrained by 10 different GRACE fields used in the combination, only a representative case based on CSR RL05 DDK5 is used here for comparison. The GIA solution based on the CSR RL05 DDK5 field has already been distributed to the community and used for comparison in a range of recent studies, such as in [Schoen et al \(2015\)](#), [Wolstencroft et al \(2015\)](#), [Nield et al \(2016\)](#), and [Martín-Español et al \(2016a\)](#).

The results from both combinations are shown in Fig. 3.17. Compared to the results derived in Ch. 2, noticeably better localized signal is recovered by the patch approach when comparing the magnitude and spatial pattern of the estimated GIA and ice-mass change rates. Especially when comparing derived ice-mass changes (Fig. 3.17c and 3.17d), the enhanced spatial resolution due to the modified methodology is clearly evident. Although over the target area integrated mass changes are mostly in good agreement (fall within  $1\sigma$  range of estimates derived in Ch. 2), there are substantial differences in EA related to both the improved data and the methodology. The largest differences occur in EA because of, but not limited to, the new RACMO2.3 dataset that simulates considerably wetter conditions in the interior of EA ([Van Wessem et al, 2014](#)) than its predecessor RACMO2.1 used in Ch. 2. These differences are reflected in the total GIA-induced mass estimates over EA which increase compared to earlier work from  $37\pm 34$  Gt/yr to  $85\pm 13$  Gt/yr with more derived present-day uplift rates along the EA coast (in Oates Land, Terre Adelie and Wilkes Land), but with considerably reduced uncertainties. The corresponding ice-mass changes in EA derived from both approaches are difficult to compare, as previous estimates barely contain any spatial details (Fig. 3.17d). Moreover, the new estimate indicates ice-mass loss with  $-45\pm 35$  Gt/yr, whereas in Ch. 2 derived estimate indicates slight mass gain of  $5\pm 38$  Gt/yr. Both estimates, however, are not statistically significant because of relatively low signal-to-noise ratio over a large area.

For WA, the mass change estimates are robust against different data and modified methodology (Fig. 3.17) with a very good agreement between both mass changes related to GIA and surface processes. Mass rate estimates from previous work amount to  $27\pm 21$  Gt/yr and  $-105\pm 22$  Gt/yr for GIA and ice-mass changes, respectively. Updated estimates exhibit considerably lower uncertainties with  $30\pm 3$  Gt/yr for GIA and  $-98\pm 5$  Gt/yr for corresponding ice-mass loss. The high-resolution spatial map of the updated GIA estimate (Fig. 3.17a) shows high uplift rates beneath the Filchner Ronne Ice shelf (FRIS) and Ross Ice shelf (RIS). The highest uplift rates are estimated again in ASE with a maximum rate of 18 mm/yr which is 3 times higher than the maximum rate estimated in ASE in Ch. 2.

In the ASE, the high GIA uplift rates were first suggested by [Groh et al \(2012\)](#) with its spatial map first being shown in [Gunter et al \(2014\)](#). The genuineness of a GIA uplift in ASE was then confirmed by ([Martín-Español et al, 2016b](#)). They derived similar uplift rates in ASE to those shown in Ch. 2 by combining complementary geodetic observations while constraining spatial wavelength of GIA us-

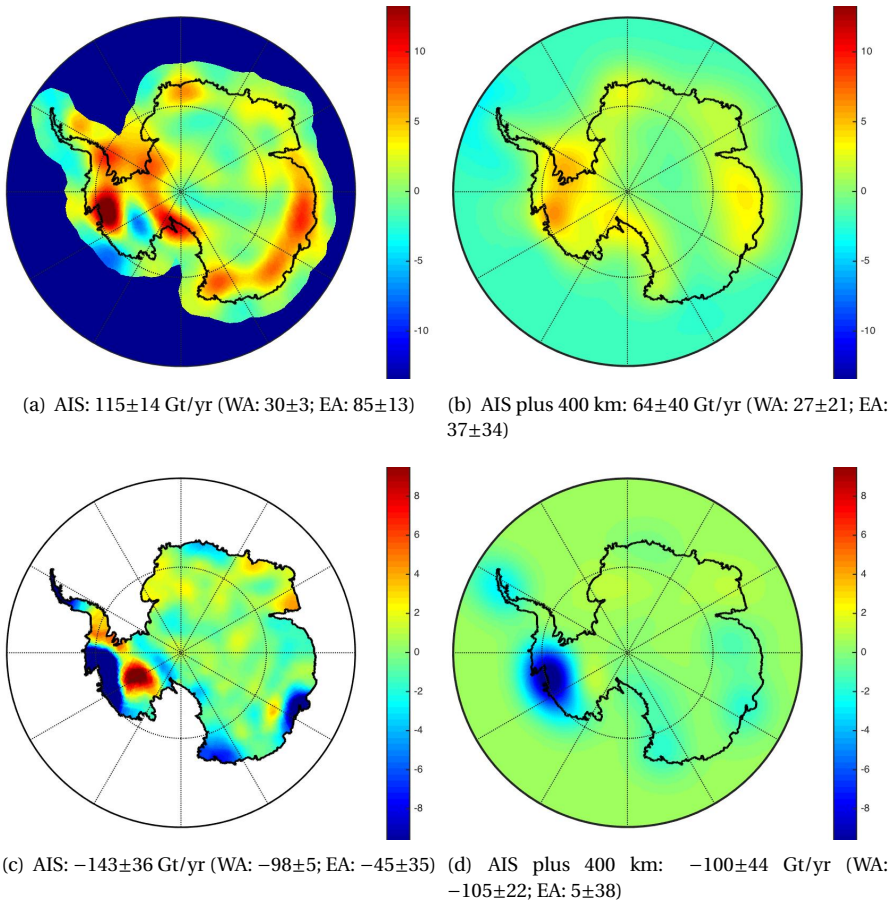


Figure 3.17: Estimates (a, c) using patch-approach and (b, d) estimates derived in Ch. 2 using GRACE CSR RL05 DDK5. Estimated GIA rates (a, b) are in mm/yr and ice-mass change rates are (c, d) in cm/yr ewh

ing forward models (500 km over WA linearly increasing up to 1700 km over East Antarctica).

3

Entirely new in the data-driven GIA solution using the proposed patch approach is the subsidence of maximum  $-8$  mm/yr (Fig. 3.17a) in the proximity of Kamb Ice Stream (KIS). Through forward modeling, [Nield et al \(2016\)](#) have demonstrated that a significant present-day GIA signal might occur in response to the Late Holocene ice changes related to stagnation and reactivation of ice streams in this area. Although heavily depending on the regional upper mantle viscosity, [Nield et al \(2016\)](#) have shown that GIA model-predicted vertical deformation in this region can reach up to  $-17$  mm/yr. The study by [Nield et al \(2016\)](#) supports, therefore, the estimated subsidence in WA. The error analysis for the combination approach shown in Fig. 3.14c provides additional evidence regarding the genuineness of the estimated present-day GIA, as the subsidence is statistically significant (at the 95% level of confidence). Thus, the proposed patch approach allows the complex spatial pattern of the present-day GIA-induced vertical deformation to be detected.

Comparing the estimated GIA-induced apparent mass trend with other recent studies that are largely independent of forward models, yields no consensus. Both ([Schoen et al, 2015](#)) and ([Martín-Español et al, 2016b](#)) used the same hierarchical Bayesian framework to separate ice-mass change and GIA. For the same time frame as used in this study, ([Schoen et al, 2015](#)) reported estimated GIA to be  $12 \pm 4$  Gt/yr and corresponding ice-mass changes to be  $-76 \pm 15$  Gt/yr for WA. While their ice-mass change rate is almost within the  $1\sigma$  range of the estimates based on the patch-approach ( $-98 \pm 5$ ), their GIA-induced apparent mass trend differs significantly from the results shown in Fig. 3.17a in terms of both the spatial pattern and the magnitude of the retrieved signal. After [Martín-Español et al \(2016b\)](#) allowed the spatial GIA length scale to vary, as opposed to using a fixed GIA length scale in ([Schoen et al, 2015](#)), they derived for the same time period a GIA solution of  $55 \pm 8$  Gt/yr over the entire AIS with corresponding ice-mass loss of  $-42 \pm 24$  Gt/yr. Although, spatially varying constraints led to a spatial GIA pattern in ASE (Fig. 10 in [Martín-Español et al \(2016b\)](#)) that is similar to the GIA estimated in this study, the area-integrated GIA solution as well as the ice-mass trend differ significantly. Nevertheless, both results suggest ice-mass loss over the AIS. This is not the case for a recent study by [Zwally et al \(2015\)](#) who derived an ice-mass increase over AIS for a similar time period (2003-2008) of  $82 \pm 25$  Gt/yr. Even when using very large patches to parameterize ice-mass changes (Tab. 3.5) at the expense of spatial resolution, a negative ice-mass balance is derived over AIS ( $-115 \pm 5$  Gt/yr for VD(600:1:700)). The serious inconsistencies between the recent studies emphasize the need for further research: (i) the data used in the combination should be accurately validated preferably with independent data sets; (ii) data-driven estimates should be extensively compared against GIA model-predicted vertical displacements that consider Late Holocene ice changes in addition to LGM, as well as a wide range of plausible Earth parameters.

### 3.5. CONCLUSIONS

In this study, unconstrained GRACE time-variable gravity fields with their full covariance information have been used in conjunction with ICESat, RACMO2.3 and GPS data to derive high-resolution spatial maps for GIA and ice-mass changes over Antarctica. For this, a dynamic patch approach has been developed that removes correlated noise in GRACE data, since the patch approach acts as a statistical filter that uses (full) variance-covariance matrix and does not require any a priori information regarding the magnitude of the estimated signal. The patch approach also allows a consistent combination of GRACE data with data that feature higher spatial resolution (ICESat-RACMO combination) without yielding attenuation of their signal magnitude. While using different (dynamic) patch configurations, the proposed patch approach incorporates geophysical knowledge about boundaries of the parameterized signal avoiding spatial leakage between the land and adjacent ocean. It also allows complex spatial pattern, if one exists, to be detected. These features increase signal recovery and yield better localization.

A range of different solutions based on different patch configurations was estimated for signal associated with GIA and ice-mass changes. Independent GPS observations helped decide that the range of patches based on 450-550 km Fibonacci grids is the most suitable for parameterizing Antarctic GIA signal. The most suitable parameterization for ice-mass changes was determined to be the range of patches based on 320-420 km Fibonacci grids. This parameterization led to the best fit between the combination results with the auxiliary results derived by applying the patch approach to the ICESat-RACMO combination. As a result, the derived GIA and ice-mass change signals exhibit considerably higher spatial resolution compared to the results derived in Ch. 2, especially when comparing derived ice-mass changes.

GIA rates derived using the proposed dynamic patch approach exhibit considerably lower uncertainties over the entire AIS compared to the results derived in Ch. 2. Although both estimates show many similarities, such as the general subsidence in EA interior and uplift beneath the Ross and Filchner Ronne Ice shelf with the highest uplift rates being estimated in ASE, there are also some noticeable differences in new GIA solution, such as a prominent subsidence in the proximity of Kamb Ice Stream and uplift along the EA coast (in Oates Land, Terre Adelie and Wilkes Land). The total GIA-induced apparent mass trend is estimated to be  $115 \pm 14$  Gt/yr (WA:  $30 \pm 3$ ; EA:  $85 \pm 13$ ).

The fact that the data used in this study are seven-years-old, should not influence the derived GIA rates which are assumed to be time invariant over relatively short geologic time frames. The derived ice-mass changes are surely not representative for the last seven years, but are derived here to demonstrate the capability of the proposed patch-approach to recover high-resolution spatial pattern of ice-mass changes. The suggested method recovers statistically significant high-resolution maps of mass loss for WA ( $-98 \pm 5$  Gt/yr) and the entire AIS ( $-143 \pm 36$  Gt/yr).

The developed patch approach along with its dynamic patch definition is capable of retrieving complex spatial pattern of present-day GIA with high certainty.

The reliability of the estimates is expected to increase once a longer timespan covered by observations becomes available. Nevertheless, further research is required that validates high quality of data used in the combination so far. A high quality of GRACE solutions and its noise description has been validated in (Farahani et al, 2016), but an accurate cross-validation of all datasets used in the combination is missing. The highest uncertainty represent GPS observations that need to be accurately corrected for elastic uplift before they can be fully exploit to constrain Antarctic GIA. Up to now, only linear trends related to Antarctic mass variations have been analyzed neglecting possibly crucial temporal variations. Therefore, the subject of the next Ch. 4 is developing an approach that allows physically natural variations of signal constituents in time. This approach will be then used in Ch. 5 to compare RACMO, GPS and GRACE data used in the combination.

# 4

## STOCHASTIC APPROACH FOR TIME-SERIES ANALYSIS

### 4.1. INTRODUCTION

As shown in Ch. 3, fully exploiting GRACE data and combining them in a consistent way with ICESat data and RACMO model output allows high-resolution spatial maps of GIA and corresponding ice-mass changes to be retrieved. To simultaneously estimate these two processes, a linear trend along with deterministically modeled seasonal components is derived for datasets used in the combination. While a constant trend is a valid assumption for describing the evolution of GIA, it is often too strong of an assumption to describe Antarctic surface processes that might contain large inter-annual, multi-year variations or even large episodic events. Accurately estimating surface processes is especially important when correcting GPS observations for elastic uplift - a step that must be performed before using GPS vertical site displacements to constrain Antarctic GIA as it has been done in e.g., [Whitehouse et al \(2012\)](#); [Ivins et al \(2013\)](#); [Sasgen et al \(2013\)](#); [van der Wal et al \(2015\)](#); [Schoen et al \(2015\)](#); [Martín-Español et al \(2016b\)](#).

Normally, surface processes are estimated as constant trends along with deterministically modeled seasonal components (e.g., [Shepherd et al, 2012](#); [Velicogna et al, 2014](#); [Gunter et al, 2014](#)) without allowing for inter-annual and seasonal variability, which might have yield erroneous trend estimates ([Davis et al, 2012](#)). Accurately modelling known sources of temporal variation is crucial for interpreting geodetic data properly, especially because of large inter-annual variations in the Antarctic climate ([Ligtenberg et al, 2012](#)). Moreover, very few geophysical processes are exactly periodic; instead there are signal constituents which fluctuate around a reference value, e.g., around a one-year period with slightly varying amplitudes. Therefore, modelling seasonal processes using traditional deterministic

---

*This chapter is mainly based on O. Didova, B. C. Gunter, R. E. M. Riva, R. Klees, and L. Riese-Koerner (2016). An approach for estimating time-variable rates from geodetic time series. Journal of Geodesy pp 1-15*

fitting methods may not provide very accurate results. In this study, we model them stochastically within a KF framework allowing for physically natural variations of signal constituents in time. This idea was brought to the geodetic community by [Davis et al \(2012\)](#) while already being a well-established technique in econometrics since the 1980s ([Harvey, 1989](#)). However, [Davis et al \(2012\)](#) assumed the statistical noise parameters to be known. Moreover, the econometric literature lacks methods for a robust estimation of the noise parameters as the optimization problem to be solved for those parameters turns out to be non-convex (i.e., there can be multiple local minima).

Therefore, the main objective of the work described in this chapter is to provide a robust tool for estimating time-variable trends from geodetic time series. For this purpose, detailed descriptions are provided on how different components such as trend and known periodicities can be modeled stochastically and put into KF form (Section 4.2). Special attention is paid towards carefully estimating the noise parameters, which is an essential step in the KF. The presented statistical framework is appropriate to any time series, but is demonstrated in this study on GRACE and GPS time series that have been widely used in the context of trend estimation (Section 4.3). A spectral analysis of the results shows that the developed tool yields more reliable estimates compared to those derived from commonly used LSA. Moreover, the technique presented allows different geodetic time series to be analyzed for validation purposes.

## 4

## 4.2. METHODOLOGY

The theory described below is largely based on [Durbin and Koopman \(2012\)](#) and [Harvey \(1989\)](#). As the methodology is demonstrated on GRACE and GPS data, Sections 4.2.1 – 4.2.4 are relevant for both types of datasets, whereas Section 4.2.5 is devoted to the analysis of features typical of GPS time series. Section 4.2.6 summarizes the major steps of the time-series analysis by the suggested method.

### 4.2.1. TREND MODELLING

The following function is commonly fit to time series data to obtain a trend:

$$y_t = \mu_t + \sum_{i=1}^2 (c_i \cdot \cos \omega_i t + s_i \cdot \sin \omega_i t) + \varepsilon_t, \quad t = 1, \dots, n, \quad (4.1)$$

where  $y_t$  denotes an observation at time  $t$ ,  $\mu_t = \alpha + \beta \cdot t$  is a linear trend with an intercept  $\alpha$  and a slope  $\beta$ , and  $(c_i \cos \omega_i t + s_i \sin \omega_i t)$  are harmonic variations with angular frequency  $\omega_i = \frac{2\pi}{T_i}$ , where  $T_1 = 1$  for an annual signal, and  $T_2 = 0.5$  for a semi-annual signal. The irregular term  $\varepsilon_t$  includes unmodeled signal and measurement noise in the series and is often assumed to be an independent and identically distributed (iid) random variable with zero mean and variance  $\sigma_\varepsilon^2$  (i.e.,  $\varepsilon_t \sim N(0, \sigma_\varepsilon^2)$ ).

The deterministic linear trend  $\mu_t = \alpha + \beta \cdot t$  can be made stochastic by letting  $\alpha$  and  $\beta$  follow random walks. This leads to a discontinuous pattern for  $\mu_t$ . A better model is obtained when working directly with the current  $\mu_t$  rather than with the

intercept  $\alpha$ . Since  $\mu_t$  can be obtained recursively from

$$\mu_{t+1} = \mu_t + \beta, \quad \text{with } \mu_0 = \alpha, \quad (4.2)$$

stochastic terms are now introduced as

$$\begin{aligned} \mu_{t+1} &= \mu_t + \beta_t + \xi_t, & \xi_t &\sim N(0, \sigma_\xi^2), \\ \beta_{t+1} &= \beta_t + \zeta_t, & \zeta_t &\sim N(0, \sigma_\zeta^2). \end{aligned} \quad (4.3)$$

Equation (4.3) with  $\sigma_\xi^2 > 0$  allows the intercept of the trend to move up and down, while  $\sigma_\zeta^2 > 0$  allows the slope to vary over time. A deterministic trend is obtained if  $\sigma_\xi^2 = \sigma_\zeta^2 = 0$ . Because there is no physical reason for the intercept to change over time, we model it deterministically by setting  $\sigma_\xi^2 = 0$ ; this leads to a stochastic trend model called an *integrated random walk*. The larger the variance  $\sigma_\zeta^2$ , the greater the stochastic movements in the trend. In other words,  $\sigma_\zeta^2$  defines how much the slope  $\beta$  in Eq. (4.3) is allowed to change from one time step to another.

A deterministic harmonic term of angular frequency  $\omega$  is

$$c_t = c \cdot \cos \omega t + s \cdot \sin \omega t, \quad (4.4)$$

where  $\sqrt{c^2 + s^2}$  is the amplitude and  $\tan^{-1}(s/c)$  is the phase. Equivalent to the linear trend, the harmonic term can be built up recursively, leading to the stochastic model

$$\begin{aligned} c_t &= c_{t-1} \cdot \cos \omega + s_{t-1} \cdot \sin \omega + \zeta_t, \\ s_t &= -c_{t-1} \cdot \sin \omega + s_{t-1} \cdot \cos \omega + \zeta_t^*, \end{aligned} \quad (4.5)$$

where  $\zeta_t$  and  $\zeta_t^*$  are white-noise disturbances that are assumed to have the same variance (i.e.,  $\zeta_t \sim N(0, \sigma_\zeta^2)$ ) and to be uncorrelated. These stochastic components allow the parameters  $c$  and  $s$  and hence the corresponding amplitude and phase to evolve over time. Note that  $c_t$  in Eq. (4.5) is the current value of the harmonic signal and  $s_{t-1}$  appears by construction to form  $c_t$ .

Introducing the stochastic trend and stochastic harmonic models into Eq. (4.1) yields

$$y_t = \mu_t + c_{1,t} + c_{2,t} + \varepsilon_t, \quad \varepsilon_t \sim N(0, \sigma_\varepsilon^2) \quad (4.6)$$

with  $c_{1,t}$  and  $c_{2,t}$  being annual and semi-annual terms, respectively. It is straightforward to extend Eq. (4.6) by additional harmonic terms using the stochastic model of Eq. (4.5) with the corresponding angular frequencies.

#### 4.2.2. STATE SPACE MODEL

The state space form of the equations defined in Section 4.2.1 is

$$\begin{aligned} y_t &= Z_t \alpha_t + \varepsilon_t, & \varepsilon_t &\sim N(0, H), \\ \alpha_{t+1} &= T_t \alpha_t + R_t \eta_t, & \eta_t &\sim N(0, Q), \quad t = 1, \dots, n, \\ & & \alpha_1 &\sim N(a_1, P_1), \end{aligned} \quad (4.7)$$

where  $y_t$  is still an observation vector,  $\alpha_t$  is an unknown state vector, and  $\varepsilon_t$  is the irregular term with  $H = I\sigma_\varepsilon^2$ . The first Equation of (4.7), where the design matrix  $Z$  links  $y_t$  to  $\alpha_t$ , is called the observation equation and the second is called the state equation. Any model that includes an observation process and a state process is called a *state space model*. The observation equation has the structure of a linear regression model where the vector  $\alpha_t$  varies over time. The second equation represents a first order vector autoregressive model. The transition matrix  $T$  describes how the state changes from  $t$  to  $t+1$ , and  $\eta_t$  is the process noise with  $Q = I\sigma_\eta^2$ . The initial state  $\alpha_1$  is  $N(a_1, P_1)$  where  $a_1$  and  $P_1$  are assumed to be known.

The state vector is defined as

$$\alpha_t = [\mu_t \quad \beta_t \quad c_{1,t} \quad s_{1,t} \quad c_{2,t} \quad s_{2,t}]^T. \quad (4.8)$$

The observation equations read

$$y_t = [1 \quad 0 \quad 1 \quad 0 \quad 1 \quad 0] \alpha_t + \varepsilon_t \quad (4.9)$$

and the state space matrices are

$$T = \begin{bmatrix} 1 & 1 & 0 & 0 & 0 & 0 \\ 0 & 1 & 0 & 0 & 0 & 0 \\ 0 & 0 & \cos\omega_1 & \sin\omega_1 & 0 & 0 \\ 0 & 0 & -\sin\omega_1 & \cos\omega_1 & 0 & 0 \\ 0 & 0 & 0 & 0 & \cos\omega_2 & \sin\omega_2 \\ 0 & 0 & 0 & 0 & -\sin\omega_2 & \cos\omega_2 \end{bmatrix}, \quad (4.10)$$

$$R = \begin{bmatrix} 0 & 0 & 0 & 0 & 0 \\ 1 & 0 & 0 & 0 & 0 \\ 0 & 1 & 0 & 0 & 0 \\ 0 & 0 & 1 & 0 & 0 \\ 0 & 0 & 0 & 1 & 0 \\ 0 & 0 & 0 & 0 & 1 \end{bmatrix}, \quad Q = I\sigma_\eta^2 = \begin{bmatrix} \sigma_\zeta^2 & 0 & 0 & 0 & 0 \\ 0 & \sigma_{\zeta_1}^2 & 0 & 0 & 0 \\ 0 & 0 & \sigma_{\zeta_1}^2 & 0 & 0 \\ 0 & 0 & 0 & \sigma_{\zeta_2}^2 & 0 \\ 0 & 0 & 0 & 0 & \sigma_{\zeta_2}^2 \end{bmatrix}.$$

For the defined state space model, the system matrices  $Z$ ,  $T$ ,  $R$ ,  $H$ , and  $Q$  are independent of time. Therefore, the corresponding index  $t$  is dropped out hereinafter. Another reason for not including any time reference is that we use equally spaced data. It is worth pointing out that a state space model can also be defined for time series containing data gaps or for unevenly spaced time series. While dealing with missing observations is particularly simple as shown in [Durbin and Koopman \(2012, chap. 4.10\)](#), some modifications might be required for unevenly spaced time series depending on the complexity of the state space model ([Harvey, 1989, chap. 9](#)).

### 4.2.3. KALMAN FILTER AND SMOOTHER

To solve the linear state space model of Section 4.2.2 the Kalman filter approach described by [Durbin and Koopman \(2012, chap. 4.3\)](#) is used. The KF recursion for

$t = 1, \dots, n$  processes the data sequentially and comprises the equations:

$$\begin{aligned} v_t &= y_t - Z a_t, & F_t &= Z P_t Z^T + H, \\ a_{t|t} &= a_t + P_t Z^T F_t^{-1} v_t, & P_{t|t} &= P_t - P_t Z^T F_t^{-1} Z P_t, \\ a_{t+1} &= T a_t + K_t v_t, & P_{t+1} &= T P_t (T - K_t Z)^T + R Q R^T, \end{aligned} \quad (4.11)$$

where  $K_t = T P_t Z^T F_t^{-1}$  is referred to as the Kalman gain and  $v_t$  is the innovation with variance  $F_t$ . Once  $a_{t|t}$  and  $P_{t|t}$  are computed, the following relation can be used to predict the state vector  $a_{t+1}$  and its variance matrix at time  $t$

$$a_{t+1} = T a_{t|t}, \quad P_{t+1} = T P_{t|t} T^T + R Q R^T. \quad (4.12)$$

While filtering aims at obtaining the expected value for the state vector using the information available so far, the aim of Kalman smoothing is to use the information made available for the entire time series. Because the smoothed estimator is based on more information than the filtered estimator, smoothing yields, in general, a smaller mean squared error than filtering. According to [Durbin and Koopman \(2012, chap. 4.4\)](#), a smoothed state  $\hat{\alpha}_t$  and its error variance  $V_t$  can be obtained by evaluating

$$\begin{aligned} r_{t-1} &= Z^T F_t^{-1} v_t + L_t^T r_t, & N_{t-1} &= Z^T F_t^{-1} Z + L_t^T N_t L_t, \\ \hat{\alpha}_t &= a_t + P_t r_{t-1}, & V_t &= P_t - P_t N_{t-1} P_t \end{aligned} \quad (4.13)$$

in a backward loop for  $t = n, \dots, 1$  initialized with  $r_n = 0$  and  $N_n = 0$ , where  $L_t = T - K_t Z$ .

#### 4.2.4. ESTIMATION OF HYPERPARAMETERS

Until now, it was assumed that the parameters  $\sigma_\varepsilon^2$  and  $\sigma_\eta^2$ , which determine the stochastic movements of the state variables and therefore have a significant influence on the results, are known. In practical applications, they are usually unknown except for the measurement noise error for which some *a priori* information is frequently available. The estimation of these so-called hyperparameters is itself based on the Kalman filter and is performed by maximizing the likelihood. If a process is governed by hyperparameters  $\psi$ , which generate observations  $y_t$ , the likelihood of producing the given data for known hyperparameters is according to [Harvey \(1989\)](#)

$$L(Y_n | \psi) = p(y_1, \dots, y_n) = p(y_1) \prod_{t=2}^n p(y_t | Y_{t-1}), \quad (4.14)$$

where  $p(y_t | Y_{t-1})$  represents the distribution of  $y_t$  conditional on the information set at time  $t-1$ , that is  $Y_{t-1} = \{y_{t-1}, y_{t-2}, \dots, y_1\}$ . The hyperparameters  $\psi$  are chosen in such a way that the likelihood function is maximized. Equivalently, we may maximize the loglikelihood  $\log L$

$$\log L(Y_n | \psi) = \sum_{t=1}^n p(y_t | Y_{t-1}). \quad (4.15)$$

The distribution of  $y_t$ , conditional on  $Y_{t-1}$ , is assumed to be normal (or Gaussian). Therefore, substituting  $N(Z_t a_t, F_t)$  for  $p(y_t|Y_{t-1})$  in Eq. (4.15) yields

$$\log L(Y_n|\psi) = -\frac{n}{2} \log(2\pi) - \frac{1}{2} \sum_{t=1}^n (\log |F_t| + v_t^T F_t^{-1} v_t), \quad (4.16)$$

which is computed from the Kalman filter output Eq. (4.11) according to [Durbin and Koopman \(2012, chap. 7\)](#).

The hyperparameters are defined as

$$\psi = 0.5 \log \begin{bmatrix} \sigma_\varepsilon^2 & \sigma_\eta^2 \end{bmatrix}^T = 0.5 \log \begin{bmatrix} \sigma_\varepsilon^2 & \sigma_\zeta^2 & \sigma_{\zeta_1}^2 & \sigma_{\zeta_2}^2 \end{bmatrix}^T, \quad (4.17)$$

which ensures that they are non-negative, since here they represent standard deviations.

#### OPTIMIZATION

Maximizing  $\log L$  is equivalent to minimizing  $-\log L$ . One searches numerically for a set of optimal parameters that provides the minimum value for negative  $\log L$ , given the process and the observed data. This optimization problem is carried out by using an Interior-Point (IP) algorithm as described in [Byrd et al \(1999\)](#). The function  $-\log L(Y_n|\psi)$  to be minimized is called the objective function. Since the IP algorithm of [Byrd et al \(1999\)](#) is a gradient-based local solver, the gradient for the objective function is computed analytically according to [Durbin and Koopman \(2012, chap. 7\)](#):

$$\begin{aligned} \frac{\partial \log L(Y_n|\psi)}{\partial \psi} &= \frac{1}{2} \sum_{t=1}^n \text{tr} \left\{ (u_t u_t^T - D_t) \frac{\partial H_t}{\partial \psi} \right\} \\ &\quad + \frac{1}{2} \sum_{t=2}^n \text{tr} \left\{ (r_{t-1} r_{t-1}^T - N_{t-1}) \frac{\partial R_t Q_t R_t^T}{\partial \psi} \right\} \end{aligned} \quad (4.18)$$

using quantities calculated in Section 4.2.3 with  $u_t = F_t^{-1} v_t - K_t^T r_t$  and  $D_t = F_t^{-1} + K_t^T N_t K_t$ .

The IP algorithm is used because it accounts for a potential non-convexity, and the problem we are dealing with is non-convex. If an optimization problem is non-convex, there can be multiple local minimum points with objective function values different from the global minimum ([Horst et al, 2000](#)). Finding a globally optimal solution of a multivariate objective function that has many local minima is very challenging. One of the main difficulties is the choice of the initial guess for the starting point  $\psi_0$  (initial solution) that is required for the optimization. If the initial guess is sufficiently close to a local minimum, the optimization algorithm terminates at this local minimum (Fig. 4.1). Visualizing the objective function is helpful to choose a suitable initial guess, but the described problem is at least four-dimensional. Dimensionality may further increase, for instance, if other periodic constituents are considered (e.g., the S2 tidal alias in GRACE data analysis); another example of a higher dimension is discussed in Section 4.2.5. Therefore, the approach is to compute the objective function for a number of starting points and

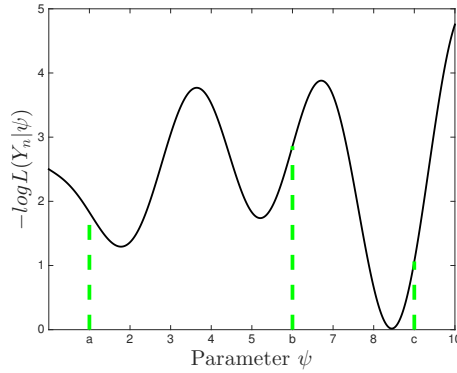


Figure 4.1: The importance of an initial guess in the context of non-convex optimization problem illustrated using a fictitious one parameter model. Depending on the starting point (initial guess), globally suboptimal (e.g., starting from points *a* or *b*) or globally optimal solution (e.g., starting from point *c*) can be found.

use the solution in further computations that provides the smallest objective function value and thus is more likely to be a global minimum (Anderssen and Bloomfield, 1975). The question, however, is how to define suitable starting points that allow all or as many as possible local minima to be identified, which in turn will increase the probability of finding the global minimum. For this, a set of uniformly distributed starting points is randomly generated within a finite search space. As a result, the same optimal solution is obtained after each run despite the fact that the method is heuristic, ensuring the existence of an optimal solution within the predefined bounds.

#### LIMITING THE PARAMETER SPACE

In the following, the parameter search space is limited in the context of a non-convex optimization problem to improve the chance of finding a global optimum. First, all lower bounds are set equal to zero. The upper bounds are chosen from LSAs to the given data as follows. The model described by Eq. (4.1) is fit to the data, and the variance of the postfit residuals is used as an upper bound for  $\sigma_\varepsilon^2$  in Eq. (4.9). This choice is justified, since LSA-residuals contain the unmodeled signal, measurement noise and possible fluctuations in the modeled terms (in our case in trend, annual and semi-annual components), whereas  $\sigma_\varepsilon^2$  in Eq. (4.9) does not include possible fluctuations in the modeled terms, because we model them stochastically as described in 4.2.1. Similarly, the upper bounds for annual and semi-annual terms are found. After subtracting a deterministic trend from the time series, annual and semi-annual signals are simultaneously estimated using LSA within a sliding window that has a minimum timespan of two years. The maximum size of the sliding window corresponds to the length of the time series used. Done this way, a sufficient amount of annual and semi-annual amplitudes are estimated and the corresponding variances are used as upper bounds for  $\sigma_{c_1}^2$  and  $\sigma_{c_2}^2$ , respectively. The choice of the upper bounds is justified by the fact that

the standard deviation of the signal computed for different time intervals is never smaller than the process noise of this signal, since here standard deviations indicate possible signal variations within the considered time span, whereas process noise represents the signal variations from one time step to the next only. Moreover, these upper bounds still include possible variations within the trend component supporting the idea being the upper limits for the process noise associated with estimated harmonics. Regarding the process noise associated with the trend component  $\sigma_\zeta^2$ , no upper bound is set.

By bounding the search space for  $\psi$  in the manner described above and by setting the amount of start points to 200 (chosen by trial and error), after each run numerically the same optimal solution is obtained. To substantiate the reliability of the estimated hyperparameters, the amplitude distribution of the estimated signal constituents Eq. (4.8) is additionally analyzed as a function of frequency. Investigating whether the amplitude spectrum shows a peak around the expected frequency allows us to draw conclusions on the reasonableness of the estimated noise parameters, since they determine the estimation of the signal constituents.

To illustrate the idea of the analysis in the spectral domain, an example based on GPS time series, which will be described later, is presented in Fig. 4.2. To produce this figure, we first estimated noise parameters stored in  $\psi$  Eq. (4.17) with and without limiting the parameter space for  $\sigma_\varepsilon^2$ ,  $\sigma_{c_1}^2$  and  $\sigma_{c_2}^2$ . For these two cases, we then estimated the state vector  $\alpha_t$  and computed the amplitude spectrum for the rate  $\beta_t$ , annual  $c_{1,t}$  and semi-annual  $c_{2,t}$  estimates. Fig. 4.2a provides an indication of reasonably estimated hyperparameters, since the amplitude spectrums of the corresponding signal estimates show significant peaks over the expected frequencies and there are no significant peaks elsewhere. For comparison, Fig. 4.2b provides an example generated without limiting the parameter space, where the hyperparameter associated with the annual signal is overestimated including variations of the rate/slope component while the amplitude of the slope has an unrealistically small magnitude of zero mm. This example also emphasizes the importance of limiting the parameter search space within a non-convex optimization problem.

The solution we obtain for the hyperparameters  $\psi$  is referred to as an *unconstrained* solution hereinafter, since only the search space for the global solver has been limited, but no restrictions are applied yet to the parameters themselves.

#### CONSTRAINED OPTIMIZATION

Introducing constraints on some of the noise parameters may improve the chance of finding a global minimum within a non-convex optimization. Sometimes, we have prior knowledge about some noise parameters, e.g., we know that  $\sigma_\varepsilon^2$  must be larger than some threshold. This inequality constraint can be easily applied within the numerical optimization (Nocedal and Wright, 2006). However, if the introduced constraints are not supported by the data, applying them may significantly change the estimated noise parameters and in turn the estimate of the state vector  $\alpha_t$  yielding erroneous geophysical interpretations. As we are dealing with a non-convex problem, the testing procedure proposed in Roese-Koerner et al

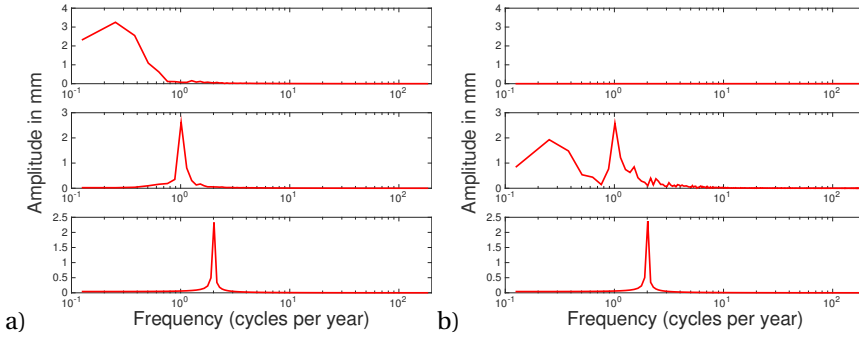


Figure 4.2: Amplitude spectra of the estimated slope (top), annual (middle) and semi-annual (bottom) components in mm. The estimation of the signal components is based on differently estimated hyperparameters (noise parameters): (a) by limiting the parameter search space for finding an optimal minimum and (b) without limiting the parameter search space.

(2012) cannot be applied. Therefore, we outline a method to verify whether the data support the applied constraints paying particular attention to non-convexity.

Firstly, we perform a so-called basic test to check the plausibility of the applied constraints. For this, we compute the absolute difference between the constrained and unconstrained case which should be smaller than the estimated standard deviations of the unconstrained hyperparameters:

$$|\psi_{\text{con}} - \psi_{\text{uncon}}| < \sigma_{\psi_{\text{uncon}}}, \quad (4.19)$$

where  $\sigma_{\psi_{\text{uncon}}}$  is derived using the corresponding Hessian. This is a quick test for serious mistakes meaning that constraints are absolutely not supported by the data if the left-hand side of the equation is larger than the right-hand side. If the basic test does not reject introduced constraints (meaning the test is positive), the second, computationally more comprehensive Likelihood Ratio test (LR-test) is performed.

The basic idea of the LR-test is the following: if the constraint is valid, imposing it should not lead to a large reduction in the loglikelihood function (Greene, 1993). Therefore, the test statistic is

$$\text{LR} = 2(\log L(Y_n | \psi_{\text{uncon}}) - \log L(Y_n | \psi_{\text{con}})). \quad (4.20)$$

LR is asymptotically  $\chi^2$  distributed with degrees of freedom equal to the number of constraints imposed (Wilks, 1938). The null hypothesis is rejected (the test is negative) if this value exceeds the appropriate critical value from the  $\chi^2$  tables, meaning that the data do not support the constraints applied.

According to Greene (1993) the parameter spaces, and hence the likelihood functions of the two cases must be related. Moreover, the degrees of freedom of the  $\chi^2$  statistic for the LR-test (Eq. (4.20)) equals the reduction in the number of dimensions in the parameter space that results from imposing the constraints. Hence, the degree of freedom equals the amount of active constraints. A constraint

is called active (or binding) if it is exactly satisfied, and therefore, holds as an equality constraint (Boyd and Vandenberghe, 2004, p. 128). In short, the LR-test is usually applied in the equality constrained case. However, if one constraint is active it reduces the number of dimensions in the parameter space by one, since it defines one parameter on which this constraint is applied. If a constraint is active it simultaneously means that this constraint strongly influences the solution. Since we are dealing with a non-convex optimization problem having multiple local minima, it may be the case that a constraint can still strongly affect the solution without becoming active, e.g., by simply shifting the solution to the next minima. Therefore, to estimate the degree of freedom for the LR-test performed in the context of non-convex optimization problem with inequality constraints, we have to estimate how many restrictions do indeed influence the solution. This will be achieved by using a brute force method summarized in Algorithm 1. The idea of the method is to successively apply the constraints until all restrictions are satisfied and thereby, to control the number of degrees of freedom for the LR-test. As it might be the case that applying a constraint to one parameter will already satisfy the constraints to the other parameters, we check whether newly added restrictions make previously added ones superfluous.

---

**Algorithm 1** : A method for determining the degrees of freedom for the LR-test performed in the context of a non-convex optimization problem with inequality constraints.

---

**Require:**  $\psi_{\text{uncon}}$

```

while the constraints are not satisfied do
  add the most violated constraint
  compute  $\psi_{\text{con}}$ 
  if the number of constraints applied > 1 then
    check whether newly added restriction makes previously added constraints
    negligible
  end if
end while

```

---

It is important to note that the degrees of freedom of the  $\chi^2$  statistic may differ already because of the used state space form; for details, the reader is referred to Harvey (1989, chap. 5). If both tests, i.e., the basic test and the LR-test, indicate that the data do not support the constraints, the constraints are relaxed towards unconstrained values until both tests are positive (see Algorithm 2). In this context, it is worth mentioning again that the basic test is performed for the purpose of reducing the computational complexity: if the constraints do not pass the basic test, there is no need to perform the LR test.

By doing so, we avoid using constraints that are too strong and not supported by the data, but still try to find a compromise between a statistically-based and a physically meaningful estimate.

---

**Algorithm 2** : The procedure of validating and potentially relaxing the inequality constraints applied within a non-convex optimization.

---

**Require:**  $\psi_{\text{uncon}}$  and  $\psi_{\text{con}}$

```

while basic and LR-test negative do
  relax the most violated constraint
  perform basic test
  if basic test negative then
    LR-test negative
  else
    perform Algorithm 1
    perform LR-test
  end if
end while

```

---

### 4.2.5. GPS

The analysis of GPS time series often differs substantially from that of GRACE data. GRACE time series have a sampling period of typically one month, data gaps are sparse, and noise correlations between the monthly data (if there are any) are negligible. GPS data are known to contain coloured (temporally correlated) observational noise that cannot be neglected (Williams, 2003a). Moreover, GPS time series are frequently unevenly spaced in time and may contain large data gaps as well as outliers. In the following sections, we describe how we handle these different features present in the GPS data.

#### PRE-PROCESSING

A KF can easily deal with unevenly distributed observations. However, equally spaced data will be beneficial when we later define the state space model for temporally correlated noise. Therefore, we generate equally spaced data by filling short gaps with interpolated values and long gaps with NaN values. We define a gap to be long if more than seven consecutive measurements are missing, i.e., more than one week of daily GPS data.

Since the KF is not robust to outliers, they should be removed beforehand. Outliers are detected here by a Hampel filter according to Pearson (2011). The measurements are removed from the time series where horizontal or vertical site displacements of a GPS station were identified as outliers.

#### COLOURED NOISE

The white noise assumption in Section 4.2.2 is too strong for the observational noise when dealing with GPS measurements. A classical approach to consider the coloured noise within the framework of KF is to extend the state vector  $\alpha_t$  in Eq. (4.7) with the noise (so-called "shaping filter") (Bryson and Johansen, 1965). To do so, we first need to assess the type of noise. For this reason, we estimate the state vector from Eq. (4.8) using filtering and smoothing recursions described in Section 4.2.3, but now the components of the state vector are made deterministic

by setting the process noise variance  $\sigma_\eta^2$  to zero and  $\sigma_\varepsilon^2$  to one. This is equivalent to the classical LSA. Dealing with missing observations in the derivation of the KF and smoother is particularly simple as shown in [Durbin and Koopman \(2012, chap. 4.10\)](#). Using KF here instead of LSA permits us to compute smoothed residuals at each time step  $t = n, \dots, 1$

$$\hat{\varepsilon}_t = H(F_t^{-1}v_t - K_t^T r_t) \quad (4.21)$$

by using quantities computed in Section 4.2.3. In this way computed residuals are now equally distributed in time. They represent an approximation of the noise, which we model as an autoregressive moving average (ARMA) process of order  $(p, q)$ . The ARMA process is defined as

$$\varepsilon_t = \sum_{j=1}^l \phi_j \varepsilon_{t-j} + \kappa_t + \sum_{j=1}^{l-1} \theta_j \kappa_{t-j}, \quad t = 1, \dots, n, \quad (4.22)$$

where  $\phi_1, \dots, \phi_p$  are the autoregressive parameters,  $\theta_1, \dots, \theta_q$  are the moving average parameters and  $\kappa_t$  is a serially independent series of  $N(0, \sigma_\kappa^2)$  disturbances and  $l = \max(p, q + 1)$  with  $p, q \in \{0, \dots, 5\}$ . Some parameters of an ARMA model can be zero, which yields two special cases: if  $q = 0$ , the process is autoregressive (AR) of order  $p$ ; if  $p = 0$ , the process is a moving-average (MA) process of order  $q$ .

The postfit residuals obtained after fitting a deterministic model to the data represent coloured noise. It is important to understand that it is only an approximation of the observational noise, since the residuals contain a potentially unmodeled time-dependent portion of the signal. To parameterize this approximate coloured noise using an ARMA( $p, q$ ) model, we need to determine how  $p$  and  $q$  should be chosen. For this, we follow the idea of [Klees et al \(2003\)](#) and use the ARMA( $p, q$ ) model that best fits the noise power spectral density (PSD) function. Thus, using the PSD function of the approximate coloured noise we estimate the pure recursive part of the filter (MA) and non-recursive part of the filter (AR) by applying the standard Levinson-Durbin algorithm ([Farhang-Boroujeny, 1998](#)). The parameters of the MA and AR models are computed using a defined  $p$  and  $q$ , which are then used to compute the PSD function of the combined ARMA( $p, q$ ) solution. To control the dimension of the state vector  $\alpha_t$  we limit the maximum order of the ARMA process to 5, which means we compute a PSD for ARMA( $p, q$ ) generated for  $p, q \in \{0, \dots, 5\}$  (including two special cases AR( $p$ ) and MA( $q$ )). Then, we use GIC (Generalized Information Criterion) order selection criterion to select the PSD of the ARMA model that best fits the PSD of the approximate coloured noise. The  $p$  and  $q$  of this ARMA model define the number of  $\phi$  and  $\theta$  coefficients used to parameterize coloured noise  $\varepsilon_t$ . More details about the use of ARMA models in the context of GPS time series can be found in [Appendix A](#).

#### STATE SPACE MODEL

GPS data are often contaminated by offsets ([Gazeaux et al, 2013](#)). If undetected, they might produce an error in trend estimates ([Williams, 2003b](#)). For Antarctica, the offsets are usually related to hardware changes and thus are step-like. To in-

corporate an offset into state space form we define a variable  $w_t$  as:

$$w_t = \begin{cases} 0, & t < \tau, \\ 1, & t \geq \tau. \end{cases} \quad (4.23)$$

Adding this to the observation Eq. (4.6) gives

$$y_t = \mu_t + c_{1,t} + c_{2,t} + \delta w_t + \varepsilon_t, \quad t = 1, \dots, n, \quad (4.24)$$

where  $\delta$  measures the change in the offset at a known epoch  $\tau$ . For  $k$  offsets, the state vector can be written as

$$\alpha_t^{[\delta]} = [\delta_1 \cdots \delta_k]^T. \quad (4.25)$$

Coloured noise  $\varepsilon_t$  can be included into the state space model as:

$$\alpha_t^{[\varepsilon]} = \begin{bmatrix} \varepsilon_t \\ \phi_2 \varepsilon_{t-1} + \cdots + \phi_l \varepsilon_{t-l+1} + \theta_1 \kappa_t + \cdots + \theta_{l-1} \kappa_{t-l+2} \\ \phi_3 \varepsilon_{t-1} + \cdots + \phi_l \varepsilon_{t-l+2} + \theta_2 \kappa_t + \cdots + \theta_{l-1} \kappa_{t-l+3} \\ \vdots \\ \phi_l \varepsilon_{t-1} + \theta_{l-1} \kappa_t \end{bmatrix} \quad (4.26)$$

with  $\eta^{[\varepsilon]} = \kappa_{t+1}$ ; then, the corresponding system matrices are given by

$$T^{[\varepsilon]} = \begin{bmatrix} \phi_1 & 1 & & 0 \\ \vdots & & \ddots & \\ \phi_{l-1} & 0 & & 1 \\ \phi_l & 0 & \cdots & 0 \end{bmatrix}, \quad R^{[\varepsilon]} = [1 \quad \theta_1 \quad \cdots \quad \theta_{l-1}]^T, \quad (4.27)$$

$$Z^{[\varepsilon]} = [1 \quad 0 \quad 0 \cdots 0].$$

It is worth noting that for irregularly spaced observations, it is less straightforward to put an ARMA( $p, q$ ) process for models of order  $p > 2$  into state space form. Therefore, the data were pre-processed as outlined in Section 4.2.5.

Combining the parameterization of  $k$  offsets (Eq. (4.25)) and of the "shaping filter" (Eq. (A.2)) with the basic model defined in Eq. (4.8) (hereafter  $\alpha_t$  used with the index  $b$  for *basic*), we take the state vector as

$$\alpha_t = (\alpha_t^{[\varepsilon]}, \alpha_t^{[b]}, \alpha_t^{[\delta]}), \quad (4.28)$$

and the system matrices as

$$\begin{aligned} Z_t &= (Z^{[\varepsilon]}, Z, \mathbf{I}_k), \quad T = \text{diag}(T^{[\varepsilon]}, T, \mathbf{I}_k), \\ R &= \text{diag}(R^{[\varepsilon]}, R, \mathbf{0}_k), \\ Q &= I\sigma_\eta^2 = \text{diag}([\sigma_{\kappa_{t+1}}^2 \quad \sigma_\zeta^2 \quad \sigma_{\zeta_1}^2 \quad \sigma_{\zeta_1}^2 \quad \sigma_{\zeta_2}^2 \quad \sigma_{\zeta_2}^2]) \end{aligned} \quad (4.29)$$

with  $Z, T$  and  $R$  being defined in Eqs. (4.9) – (4.10).

After defining this modified state space model, GPS time series can be processed as GRACE time series. In particular, the search space for the global solver associated with the ARMA parameters does not experience any bounds.

#### 4.2.6. SUMMARY OF THE DEVELOPED FRAMEWORK

The flow diagram in Fig. 4.3 outlines the major steps of the time-series analysis by the suggested method. The method can be applied to any equally spaced data; it can cope with missing observations and different stochastic properties of the data. Once the components of interest are defined in the state vector, the corresponding state space model with all required matrices can be formulated. If present, time-correlated observational noise can be modeled using a general ARMA model that subsumes two special cases (AR and MA) as described in Section 4.2.5 or in more detail in Appendix A. Another representation of the coloured observational noise within the state space formalism can be found in e.g., [Dmitrieva et al \(2015\)](#), in which a linear combination of independent first-order Gauss-Markov (FOGM) processes is used to approximate the noise.

Once in the state space form, the parameters governing the stochastic movements of the state components are estimated by numerically optimizing likelihood. The likelihood function is computed using the by-products of the Kalman filter (Eq. (4.16)). Finding an optimal solution as demonstrated in Section 4.2.4 is the key of the proposed methodology, since it ensures optimal estimates for the hyperparameters, which in turn determine the estimates of the signal constituents. Limiting the parameter search space (Section 4.2.4), as well as imposing constraints (Section 4.2.4) that are supported by the data, both increase the likelihood of getting the optimal solution. Once the hyperparameters are estimated, the Kalman filter and smoother can be used (Section. 4.2.3) for obtaining the best estimate of the state at any point within the analyzed time span. This can be important for investigating the way in which a component such as trend has evolved in the past.

### 4.3. APPLICATION TO REAL DATA

In this section, we demonstrate the performance of the proposed methodology compared with the commonly used LSA technique on two different types of geodetic time series <sup>1</sup>. As an example, we use GRACE and GPS time series, although the methodology can be applied to any other time series. After a brief description of the data sets, the results of computational experiments are presented and discussed.

#### 4.3.1. DATA

We use daily GPS vertical site velocities at the CAS1 station, which is located in Wilkes Land, East Antarctica. There are three reasons for selecting this GPS station: first, it is a GPS site with continuous long-term observations; second, the time series data contain all the features described in Section 4.2.5; and third, because of its geolocation. A significant accumulation anomaly event was concentrated along the Wilkes Land coast in 2009 ([Luthcke et al, 2013](#)). Due to a high

<sup>1</sup>The freely available software provided by [Peng and Aston \(2011\)](#) was used as an initial version for the state space models. MATLAB's Global Optimization Toolbox along with the Optimization Toolbox was used to solve the described optimization problem.

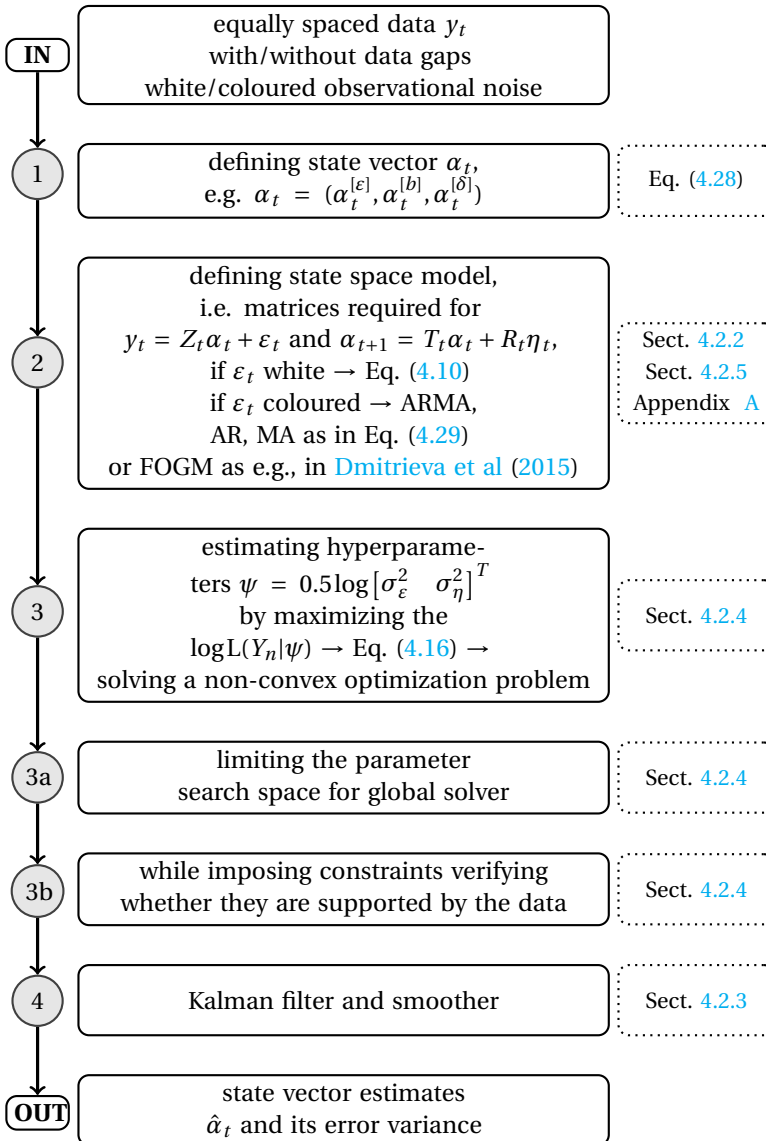


Figure 4.3: Flow diagram to summarize the major steps of the described approach for time series analysis.

signal-to-noise ratio, we expect this event to be detected by both observing systems, GPS and GRACE. Consequently, we can use this prior knowledge about geophysical processes to verify the plausibility of the proposed methodology.

The GPS data at CAS1 are processed similar to [Thomas et al \(2011\)](#). The GPS time series contains two step-like offsets (in Oct. 2004 and Dec. 2008) within the chosen estimation period, which is Feb. 2003 to Dec. 2010. For the same period, GRACE monthly time series are computed at Delft University of Technology ([Farahani, 2013](#)) complete to spherical harmonic degree/order 120 and optimally filtered using a Wiener filter ([Klees et al, 2008](#)). Stokes coefficients representing the monthly gravity fields were converted into vertical deformations following [Kusche and Schrama \(2005\)](#) making GRACE data comparable with GPS observations. This conversion is done for potential validation which, as will be shown later, leaves room for physical interpretations if the proposed methodology is applied.

4

### 4.3.2. RESULTS

Results derived by modelling signal constituents stochastically within the KF framework are called hereinafter KF results for brevity. We show plots in the time and frequency domain for GPS and GRACE time series at the same geolocation. Both time series represent vertical deformations due to GIA and the elastic response of the solid Earth to the surface load. Before discussing the results it is worth noting that what is called *trend* (in mm) thereafter is the integrated random walk part of the signal ( $\mu_t$  in Eq. (4.8)) with deterministically modelled intercept and time-varying *slope* (or rate) in mm/yr introduced as  $\beta_t$  in Eq. (4.8).

For GRACE time series, we estimate the slope, and annual, semi-annual and tidal S2 periodic terms deterministically using LSA and stochastically using the KF framework. In both cases, the intercept is co-estimated deterministically. Fig. 4.4 shows vertical deformation derived based on GRACE data, the LSA fit and the KF fit, as well as estimated trends using different techniques. Error bars represent one-sigma uncertainties. Figs. 4.4a and 4.4b serve as a visual inspection and indicate that the model which allows signal components to vary in time represents the data considerably better than the model that assumes a linear trend and exactly periodic processes with constant amplitudes.

Fig. 4.5 demonstrates similar results as Fig. 4.4, but for GPS vertical site displacements. LSA results shown in Fig. 4.5a were generated by fitting intercept, a slope, annual and semi-annual terms and two offsets to the time series without modelling coloured noise. Time-correlated noise model is usually used to estimate more realistic parameter uncertainties than those resulting from white noise assumption ([Thomas et al, 2011](#)). However, to generate the KF results, we co-estimated time-correlated noise parameters as well. Following the procedure described in Section 4.2.5, we computed the noise PSD function of the LSA residuals, which is shown in black in Fig. 4.6. An AR(3) model (red in Fig. 4.6) was found to provide the best fit to the PSD of the approximate coloured noise. Coloured noise in the GPS time series was then parameterized with three autoregressive coefficients and co-estimated along with signal components. The results in Fig. 4.5 suggest that the KF method (Fig. 4.5b) outperforms the LSA method (Fig. 4.5a).

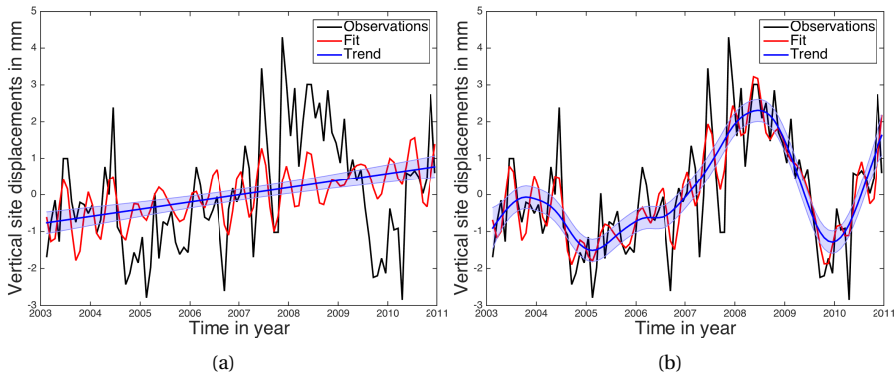


Figure 4.4: Vertical site displacements in mm derived based on GRACE data (black), the fit of a trend function (blue), and the fit of a trend function together with annual, semi-annual and tidal S2 periodic terms (red) using (a) LSA and (b) KF framework. Error bars are  $1\sigma$ .

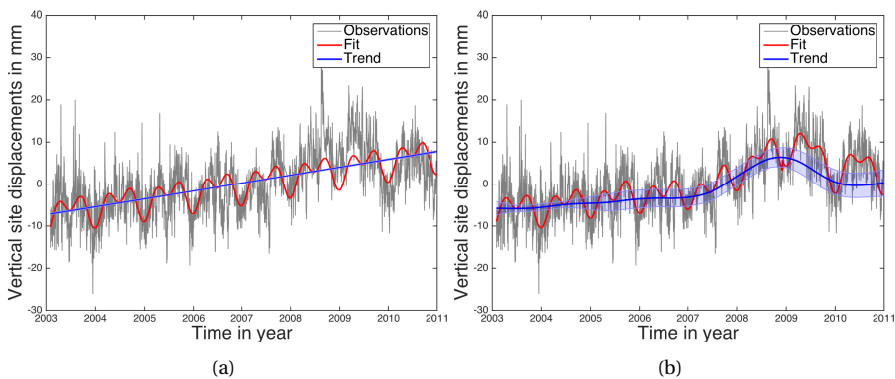


Figure 4.5: Vertical site displacements in mm observed by GPS (grey), the fit of a trend function (blue), and the fit of a trend function together with annual and semi-annual terms and two offsets (red) using (a) LSA and (b) KF framework. Error bars are  $1\sigma$ . Starting from Oct. 2004, there are inflated uncertainty estimates in (b), because of the co-estimation of two step-like offsets. In (a), the over-optimistic formal LSA errors are barely perceptible.

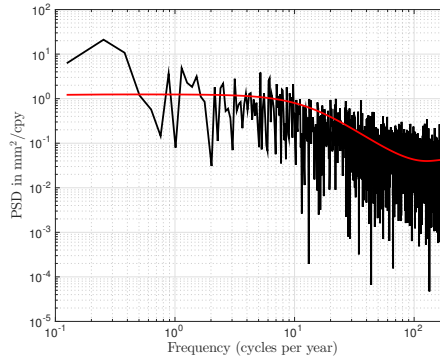


Figure 4.6: The PSD (power spectral density) of AR(3) model (red) that best fits the PSD of the postfit residuals (black), whereby LSA was used to fit a multi-parameter model to the GPS time series at the CAS1 site.

4

Because estimating rates/slopes as accurately as possible is the primary motivation of this study, Fig. 4.7 outlines the corresponding results. A constant slope as a result of a deterministic fitting along with the stochastically modeled time-varying slope are shown for GRACE (Fig. 4.7a) and GPS time series (Fig. 4.7b). To allow for a direct comparison between LSA and KF results, we compute a mean slope from the time-varying slope. If there were no changes in the rates of vertical deformation, the two constant values should be the same. In fact they differ significantly, as the proposed methodology suggests the presence of low-frequency variability in the slope component (black graphs in Fig. 4.7) that cannot be explained by any other modelled component. For GRACE, the constant slope estimated using LSA is  $0.2 \pm 0.07$  mm, whereas the mean slope determined from the time-varying estimates is  $0.36 \pm 0.12$  mm. Although these are small numbers in absolute terms, their relative difference is larger than 50%. For GPS, the slope derived based on KF is almost 2.5 times smaller than the LSA based slope estimate being  $0.77 \pm 0.46$  and  $1.89 \pm 0.11$  for KF and LSA, respectively.

To explain the different uncertainty estimates shown in Fig. 4.7, it is worth mentioning here that we propagated the correlations between errors of subsequent KF slope estimates into the mean slope. To compute the covariance matrix for the smoothed state vector  $\hat{\alpha}_t$ , that is,  $Cov(\alpha_t - \hat{\alpha}_t, \alpha_j - \hat{\alpha}_j)$  for  $t = 1, \dots, n$  and  $j = t + 1, \dots, n$ , the quantities defined in Section 4.2.3 were used according to Durbin and Koopman (2012, chap. 4.7):

$$Cov(\alpha_t - \hat{\alpha}_t, \alpha_j - \hat{\alpha}_j) = P_t L_t^T L_{t+1}^T \cdots L_{j-1}^T (I - N_{j-1} P_j). \quad (4.30)$$

For the case  $j = t + 1$ ,  $L_{t+1}^T \cdots L_t^T$  is replaced by the identity matrix  $I$ , which has a dimension of the estimated state vector. To compute the uncertainty estimates from LSA, formal errors were rescaled by the *a posteriori* variance. This is a commonly used approach (e.g., Baur (2012)) which yields over-optimistic uncertainties (e.g., Williams (2003a)).

In the context of slope estimation, we find it worth noting that especially for

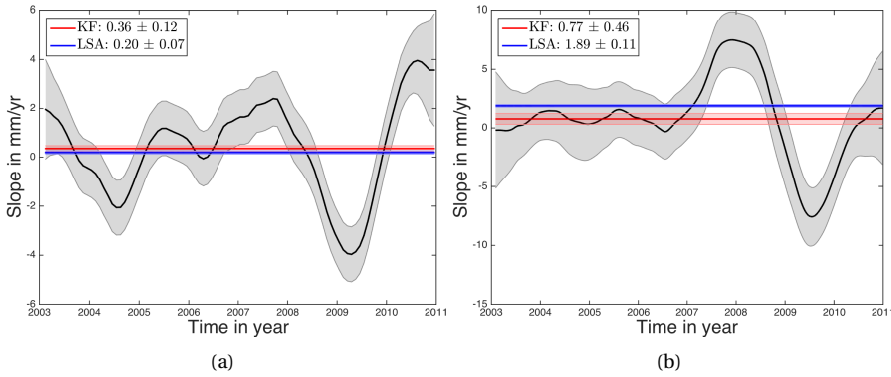


Figure 4.7: Slope estimates in mm/yr: KF time-varying slope (black), mean slope derived from KF time-varying slope (red), and LSA estimated slope (blue). (a) GRACE time series; (b) GPS time series. Error bars are  $1\sigma$ . The legend shows the values for the mean slope derived from KF time-varying slope (red) and for the LSA estimated slope (blue). Note, that different scales are used.

Antarctic GPS site velocities that are used to constrain GIA rates, each erroneously estimated millimeter of vertical deformation corresponds to significantly erroneous ice-mass change estimates (Gunter et al, 2014) highlighting the need to estimate these rates as accurately as possible.

To prove the presence of low-frequency variability in the slope component estimated with the KF technique, we compute the amplitude spectrum of the GRACE and GPS time series (cf. Fig. 4.8a and Fig. 4.8b, respectively). The results confirm the presence of long-term variations that deviate from a linear trend in both time series. While these inter-annual variations are absorbed in the residuals when using LSA (blue graphs in Fig. 4.8), they are captured by KF (red graphs in Fig. 4.8) and map into the time-varying slope component (Fig. 4.7). Considering root mean square (RMS) misfits for quantitative comparison, there is about 41% and 13% reduction in RMS misfits for GRACE and GPS time series, respectively, as a result of using the proposed KF instead of the LSA technique. As can be seen from Fig. 4.8, the dominant reduction of the RMS misfit is due to the time-varying slope with a smaller part being explained by the time-varying annual signal (the amplitude of the KF residuals around the 1 cycles per year frequency is smaller than the amplitude of the LSA residuals). The signals in the high frequency domain are considered as noise.

To validate the results based on the proposed methodology from the geophysical point of view, we plot the estimated time-varying rates derived from GPS and GRACE time series, respectively, in Fig. 4.9. The known accumulation anomaly event from 2009 is clearly evident. In this year, GPS and GRACE, observe maximum subsidence of the solid Earth as an immediate response to the high levels of accumulation within the analysed time period. Although the two observing systems do not agree perfectly, they do observe similar processes starting from 2005. In fact, there are a number of different factors to be considered when comparing GPS and

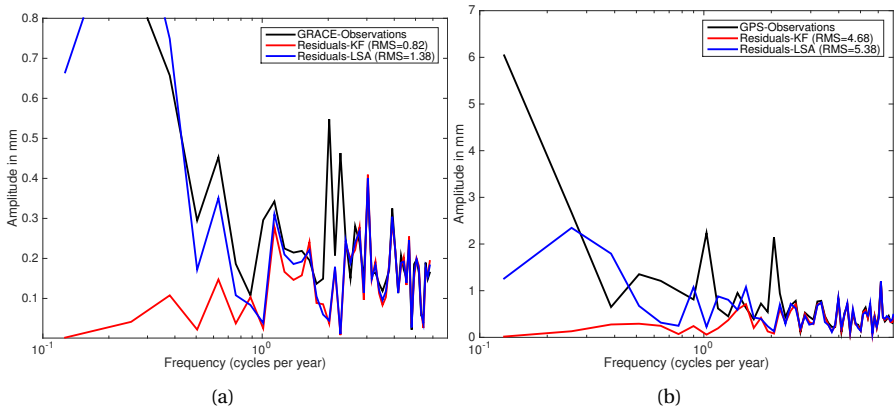


Figure 4.8: Amplitude spectra for observations (black), postfit residuals using the proposed KF technique (red) and the LSA technique (blue). (a) GRACE time series; (b) GPS time series. Root mean square (RMS) misfits are indicated for both KF and LSA. Note, that different scales are used.

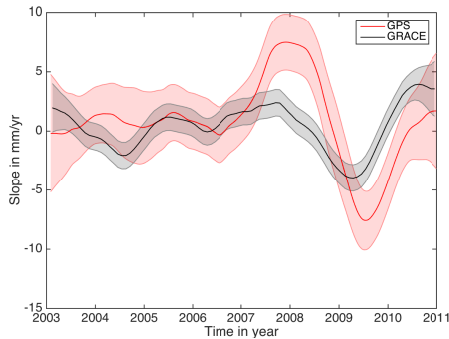


Figure 4.9: Time-varying slope for GRACE and GPS time series at the geolocation of the CAS1 site when using the proposed KF technique. Time-varying error bars are  $1\sigma$ .

GRACE time series, such as the spatial resolutions of the data sets (GPS-derived deformations are discrete point measurements, while GRACE results represent a spatial average), the effects of geocenter motion should be considered when converting GRACE coefficients into vertical deformation, etc. Though the validation of different geodetic observing techniques is out of the scope of this study, we feel the proposed methodology provides better interpretation opportunities (Fig. 4.9) than the traditional LSA approach. It should also be noted that once GRACE and GPS time series are corrected such that they represent the same signal, it is straightforward to combine them within the described approach. However, GRACE and GPS time series are used in this study to validate the proposed methodology. It is also worth mentioning here that we have chosen this GPS station because of the existing prior knowledge about the geophysical process (accumulation anomaly) that took place there in 2009. Two different observing systems, GPS and GRACE, detected this geophysical process because of its high magnitude. While estimating time-variable rates, the time series from these two different observing systems were treated in two different ways with respect to the observational noise model used: white noise for GRACE and coloured noise for GPS time series. Nonetheless, the time-varying trends derived from the GRACE and GPS time series show the same behavior. We therefore interpret this behavior as a signal and not as a potentially mismodelled observational noise.

The target of this study is to provide a robust tool for reliable trend estimation. The robustness of the proposed methodology is determined by finding an optimal minimum that is necessary for estimating the noise parameters (Section 4.2.4) which in turn, are the key for reliable rate estimates. To demonstrate the role of the noise parameters on the estimated signal components, we use the example shown in Fig. 4.2: Based on the GPS time series, we estimate the noise parameters by limiting the parameter search space for finding an optimal solution (as it is done through this section) and without limiting the parameter search space. Using these differently estimated noise parameters, we estimate modelled signal constituents. In Fig. 4.10, we illustrate the results for the slope and the annual component in the time domain (there is no evident difference in the semi-annual component as can be seen in Fig. 4.2). By limiting the parameter search space, the process noise for the slope and annual component is estimated to be 0.37 mm/yr and 0.06 mm, respectively. The corresponding estimates are shown in Fig. 4.10a suggesting a correlation between both, the changes in the rates of vertical deformation and their annual variability. This is physically reasonable, as both are responses to the changing climate.

If the parameter search space is not limited, the process noise for slope and annual signal is  $5.75 \cdot 10^{-8}$  mm/yr and 0.34 mm, respectively. Fig. 4.10b shows the corresponding plots. Because the slope is not allowed to vary much, it is comparable with the LSA estimate shown in Fig 4.7b. However, the variance of the annual component is much higher than the one used in Fig. 4.10a, which is why the corresponding annual amplitude in Fig. 4.10b shows an erratic behaviour.

We could also assume the noise parameters to be known, e.g., by modelling the slope deterministically and using a fixed standard deviation for the annual signal.

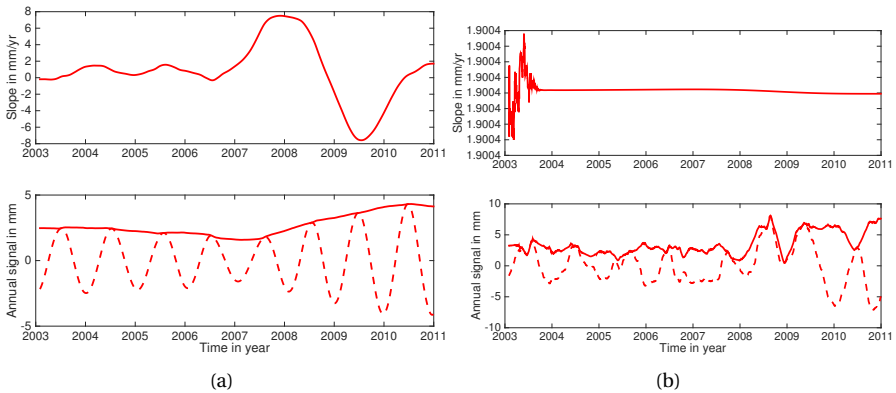


Figure 4.10: Estimated time-varying slope (top) and annual signal (bottom, dashed line) along with the time-varying annual amplitude (bottom, solid line) for GPS vertical site displacements using the proposed KF framework. a) when limiting the parameter search space for finding an optimal minimum; b) without limiting the parameter search space. Note, that different scales are used.

4

The higher we set this standard deviation the more we force the annual signal to absorb long-term variations and possible variations originating from other sources yielding wrong interpretations. Therefore, we recommend to limit the parameter search space as described in Section 4.2.4 and to verify potentially existing prior knowledge about noise parameters according to Section 4.2.4 to ensure the reliability of the estimated signal constituents. Moreover, we suggest modelling all signal components stochastically to ensure a reliable noise parameter estimation, unless there are good reasons not to do so.

#### 4.4. CONCLUSIONS

We developed a robust method for estimating time-variable trends from geodetic time series. This method is more sophisticated compared to commonly used LSA, as it allows the rate and seasonal signals to change in time. The advantages are twofold: more reliable trend estimation, because i) there is no contamination by seasonal variability and ii) it accounts for any long-term evolution in the time series, which would appear as noise when modelled as a time-invariant slope.

The right choice of the noise parameters is at the heart of the proposed methodology. We suggested a method which allows a robust estimation of the noise parameters. We verified the reliability of the estimates using spectral analysis. The plausibility of the estimated time-varying rates was additionally confirmed by existing geophysical knowledge. Furthermore, the results estimated using the KF framework were visually compared with those derived using LSA in the time and frequency domains. Visual inspections and RMS misfits suggested that KF outperforms LSA. The proposed methodology is not limited to GPS and GRACE time series, but can be used for any other time series.

Our results suggest that potential changes in rates may yield significantly dif-

ferent trends when post-processed compared to the deterministic linear trend. Indeed, the longer the time series, the more deviations can be expected from the deterministic linear trend assumption as well as from the constant seasonal amplitudes and phases. Moreover, any change in the trend term reflects an acceleration, making the stochastic approach much more flexible than the deterministic one. It can therefore be reasonable to consider signal as a stochastic process in particular when analyzing climatological data.



# 5

## COMPARING GRACE-, SMB-, AND GPS-DERIVED TIME-VARYING RATES IN ANTARCTICA

### 5.1. INTRODUCTION

In this chapter, the time series of GRACE and SMB involved in the combination described in Ch. 3, as well as GPS observations are compared against each other using the approach suggested in Ch. 4.

The evolution of changes in Antarctic surface mass balance (SMB) modeled by a regional climate model should also be observed in GRACE-derived mass changes corrected for ice dynamics. The reliability of SMB is crucial when used within space-based methods to derive Antarctic ice-mass changes (Shepherd et al, 2012). An accurate knowledge of temporal variations in SMB is especially important for correcting GPS-derived vertical displacement rates for elastic deformation before using GPS to constrain Antarctic GIA. A successful validation, therefore, can be an important contribution to climate change research, as the AIS is one of the main contributors to global sea-level rise.

Although it is known that Antarctic SMB exhibits large inter-annual variations (Helsen et al, 2008; Ligtenberg et al, 2012), most studies of Antarctica have described the evolution of mass changes in terms of linear rates and accelerations. Only a few studies have paid special attention to Antarctic inter-annual variations, the signal that maps into the time-varying trend when applying the approach suggested in Ch. 4. Horwath et al (2012) compared inter-annual variations of the Antarctic ice sheet derived from GRACE and ENVISAT radar altimeter data. In the Antarctic Peninsula (AP) and Amundsen Sea Embayment (ASE), Sasgen et al (2010)

compared inter-annual variations derived from GRACE with accumulation variations based on the net precipitation from the European Centre for Medium Range Weather Forecasts. Over the entire ice sheet, [Wouters et al \(2013\)](#) found that most GRACE-observed changes are controlled by SMB, and that the stochastic ice sheet variability can strongly affect estimates of linear mass-loss rates and, in particular, accelerations. [Velicogna et al \(2014\)](#) examined deterministically derived trends and accelerations from SMB and GRACE over five regions in Antarctica. Over the entire ice sheet, they concluded that "...SMB only explains a small part of the evolution of the change in mass balance".

The first purpose of this chapter is to compare SMB- and GRACE-based time-varying trends over the entire AIS, integrated over drainage systems (Fig. 3.4) defined by [Zwally et al \(2012\)](#). In order to do so, the dynamic patch approach described in Ch. 3 is utilized to ensure a fair comparison between SMB and GRACE data in terms of spatial resolution. The stochastic approach for time-series analysis introduced in Ch. 4 is then utilized to model trends along with known periodicities from SMB and GRACE data at the level of drainage systems. The second purpose of this chapter is to compare time-varying trends derived from GRACE, SMB, and GPS at the locations of GPS stations. This cross-comparison is also based on the patch approach along with the stochastic approach for time-series analysis.

5

## 5.2. DATA AND METHODOLOGY

To compare SMB and GRACE derived time-varying trends over the entire AIS, unconstrained DMT2 monthly GRACE solutions completed to degree 120, along with full noise covariance matrices, are used ([Farahani et al, 2016](#)). Degree-1 coefficients were added using values generated from the approach of [Swenson et al \(2008\)](#), and the  $C_{20}$  harmonics were replaced with those derived from satellite laser ranging ([Cheng and Tapley, 2004](#)). For the same time period for which DMT2 solutions are currently available (February 2003 to December 2011), time series of RACMO2.3 monthly cumulative SMB anomalies were used to derive time-varying trends.

To ensure a fair comparison between SMB and GRACE data in terms of spatial resolution, the dynamic patch-approach described in Ch. 3 for the same range of patches (320 - 420 km) was applied to both datasets. GIA rates derived in Ch. 3 have been removed from the total monthly GRACE signal at satellite altitude before applying the dynamic patch approach. As a direct output from the dynamic patch approach, regional surface densities from both SMB and GRACE are estimated. Surface densities derived from SMB represent variations within the firn layer in contrast to surface densities derived from GRACE which additionally contain variations within the ice layer after being corrected for GIA. GRACE-derived surface densities are calibrated to the LPZ in EA using the LPZ-bias derived in Ch. 3 (Tab. 3.4) making the monthly estimates regional to Antarctica. Please note that, strictly speaking, the time series derived from GRACE and SMB are not independent, since GIA removed from the total GRACE signal is estimated in Ch. 3 using a linear trend based among others on SMB computed for the time frame from February 2003 to October 2009. Nevertheless, time-varying rates derived from GRACE

and SMB are regarded as mainly independent, because GIA is a time-invariant trend that might only bias the non-linear variations if estimated incorrectly.

In the next step, the monthly derived surface densities from both datasets are integrated over the 27 Antarctic drainage systems (Fig. 3.4) defined by Zwally et al (2012). The resulting time series are used to estimate time-varying trends along with stochastically modeled known periodicities (annual and semiannual components for GRACE and SMB, and additionally tidal S2 periodic term for GRACE). For both datasets, a constant intercept is co-estimated.

To compare SMB, GRACE, and GPS derived time-varying trends, additional processing steps are required. First, SMB and GRACE derived monthly surface densities are converted into vertical deformation at the GPS stations. For this, the spherical harmonic analysis detailed in Sec. 3.3.1 is applied to convert surface densities into spherical harmonics  $C_{nm}^q, S_{nm}^q$ . These spherical harmonics are then converted into  $C_{nm}^h, S_{nm}^h$  in terms of vertical deformation following Kusche and Schrama (2005) as

$$\begin{Bmatrix} C_{nm}^h \\ S_{nm}^h \end{Bmatrix} = \frac{3\rho_w}{\rho_e} \frac{h'_n}{2n+1} \begin{Bmatrix} C_{nm}^q \\ S_{nm}^q \end{Bmatrix} \quad (5.1)$$

using the density of water  $\rho_w = 1000 \text{ kg/m}^3$  and the density of Earth  $\rho_e$  defined for Eq. (3.12), and Load Love numbers  $h'_n$ . Monthly spherical harmonics in terms of vertical deformation  $C_{nm}^h, S_{nm}^h$  are then synthesized at the locations of GPS stations resulting in a time series of vertical deformation. The major steps applied to SMB and GRACE data required for the comparisons detailed in this chapter, are summarized in Fig. 5.1.

GPS-derived vertical displacements at 10 permanent GPS stations are used. The processing of the GPS displacements followed that of Thomas et al (2011), but were intentionally not corrected for non-tidal atmospheric loading. The correction was applied in this framework using the AOD product (Flechtner, 2007) to be more consistent with GRACE-derived data. Only observations at 10 GPS stations (in contrast to 37 available) are validated here due to availability of the data necessary to perform meaningful time series analysis. This means that only observations at permanent GPS stations are utilized with a minimum of 6 years of observations available within the same time span as GRACE data used in the validation (February 2003 to December 2011). At the sites with co-located GPS receivers, the site with the longest record is used.

Despite the fact that GPS are discrete point measurements and GRACE and SMB results are spatially smoothed over the same range of patches (320 - 420 km derived in Ch. 3), there are two important aspects to be considered when comparing the vertical deformations obtained from the three independent techniques. The GPS observations used here refer to a reference frame with origin in the Center-of-Mass of the total Earth system (CM) and are therefore global, containing global GIA. In contrast, the vertical deformations obtained from SMB and GRACE are regional and GIA-free. This is because SMB is from a regional climate model and by definition GIA-free, and GRACE is calibrated to the LPZ in EA and corrected for the GIA signal derived in Ch. 3. To ensure a fair comparison between SMB, GRACE, and GPS time series, a contamination of GPS signal by leakage from non-

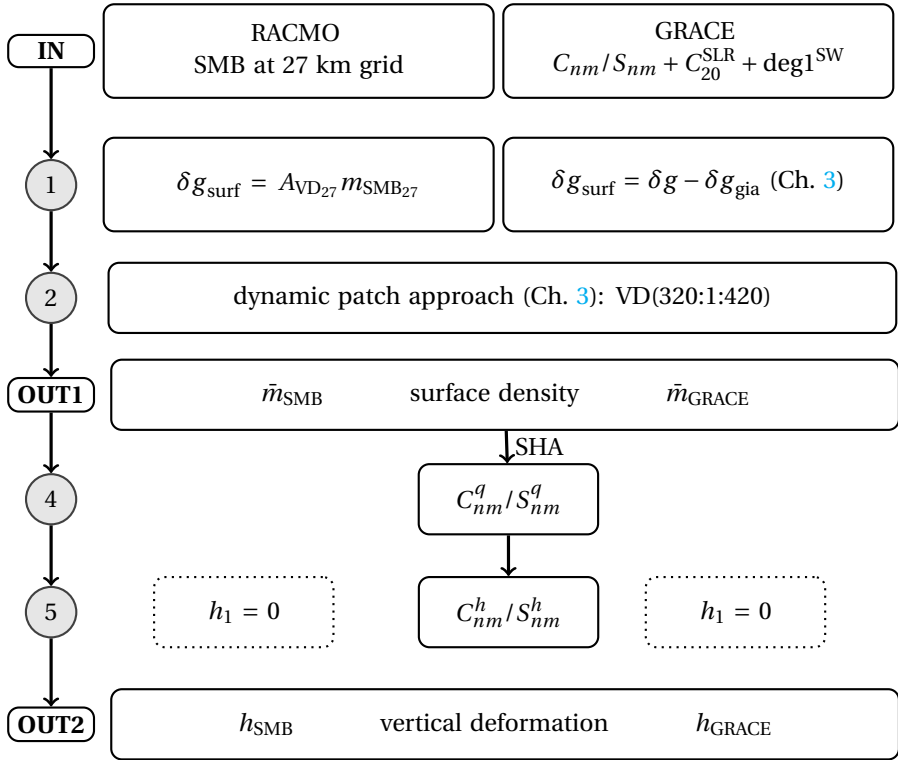


Figure 5.1: Flow diagram to summarize the major steps of the performed validation.

5

Antarctic sources must be avoided. This leakage is mostly originating from geocenter motion and changes in the spherical harmonic coefficient  $C_{20}$ . Since geocenter motion is a global signal, mostly driven by sources outside Antarctica (Clarke et al, 2005), it should be removed from the GPS time series. Geocenter motion is the motion of the CM with respect to the Center-of-Figure of the solid Earth (CF) (Ray, 1999) and is proportional to the degree-1 spherical harmonic coefficients. To remove geocenter motion from GPS time series, a degree-1 solution based on Swenson et al (2008) is utilized. When computing vertical deformation from SMB- and GRACE-derived surface density (Step 5 in Fig. 5.1), degree-1 is removed for consistency. Note that the degree-1 signal contained in GRACE after subtracting GIA (Step 2 in Fig. 5.1) can be contaminated by erroneous GIA, but is assumed to be compensated by the fact that the same data is used in Ch. 3 to derive it. This touches upon the second important aspect: GIA contaminates the GPS secular trend at very low degrees, mostly driven by GIA in the Northern Hemisphere (Klemann and Martinec, 2011). Hence, a time series of low-degree spherical harmonic  $C_{20}$  derived by Sun et al (2016) with degree-1 solution based on Swenson et al (2008) are assumed to be a sufficient first-order approximation of the non-Antarctic leakage.



Figure 5.2: Antarctic drainage systems defined by Zwally et al (2012) together with the following location indicators: Antarctic Peninsula (AP), Amundsen Sea Embayment (ASE), Ross Ice Shelf (RIS), Filchner Ronne Ice shelf (FRIS), Dronning Maud Land (DML), Enderby Land (EL), Kemp Land (KL), Lambert Glacier (LG), Philippi/Denman (PD), Queen Mary Land (QML), Wilkes Land (WL), Terre Adèlie (TA), George V Land (GVL), Siple Coast (SC), Smith Glacier (SG), Thwaites Glacier (TG), Pine Island Glacier (PIG).

## 5.3. RESULTS

First, the comparison of SMB and GRACE derived time-varying trends in terms of Gt/yr integrated over Antarctic drainage systems (Fig. 5.2) are discussed in Sec. 5.3.1. The cross-comparison of time-varying trends in terms of vertical deformation derived from three independent techniques (SMB, GRACE, and GPS) is subject of Sec. 5.3.2.

### 5.3.1. GRACE - SMB

Fig. 5.3 shows time-varying slopes estimated from GRACE data and SMB, respectively for the most dynamic region in the AIS, namely the Amundsen Sea Embayment (ASE). To highlight similarities/differences between the estimated time-varying trends from GRACE and SMB, two criteria are used: correlation  $\rho$  and WRMS signal reduction  $R$ . Signal reduction is used as a second criterion, because correlation is only a measure for linear relationship, and is not capable of accounting for any stochastic properties. Following Tesmer et al (2011), reduction of GRACE

trend WRMS is computed in percent as

$$R = 100 \cdot \left( \frac{WRMS_{GRACE} - WRMS_{GRACE-SMB}}{WRMS_{GRACE}} \right), \quad (5.2)$$

where  $WRMS_{GRACE}$  is the signal WRMS of the GRACE trend and  $WRMS_{GRACE-SMB}$  the signal WRMS of the GRACE-SMB residuals.

Visual inspection of trends obtained for three basins in the ASE (left column in Fig. 5.3) suggests that variations in the GRACE-derived trend are mostly explained by variations in the firn layer. Although trends from both datasets exhibit the same behavior with a significant correlation of minimum 0.6, a systematic bias between the two trends is clearly evident. Since SMB data contain variations within the firn layer and GRACE-derived rates represent variations within the firn and ice layer, subtracting SMB from GRACE rates should provide variations predominantly due to ice dynamics. Therefore, a mean trend for ice dynamics (ICE) is estimated by subtracting the mean slope of SMB from the mean slope of GRACE. This bias is added to the time-varying SMB rates resulting in  $SMB + ICE$  (right panel in Fig. 5.3).  $SMB + ICE$  was then used to recompute the reduction of GRACE trend WRMS. A noticeably better fit between the two time series is clearly visible after the SMB-derived trend has been shifted. The greater resemblance of the two trends also manifests itself in a considerably higher reduction of GRACE trend WRMS: on average, 70% of the GRACE-trend variance can be explained by  $SMB + ICE$  rates in this region. Since for all three basins the computed biases are negative, they add up to -148 Gt/yr of dynamic-driven mass loss in ASE. Note that in the following it is  $SMB + ICE$  that will be shown in the figures and validated against GRACE-derived time-varying trend. Corresponding statistics and mass change values for all basins are summarized in Tab. 5.1. Special attention should be paid to the acceleration term, as any change in the time-varying trend reflects an acceleration. As can be seen in Fig. 5.3, acceleration is not constant within the considered time span, although an accelerated process is captured by GRACE-derived trend in all three basins starting approximately from 2008. This accelerated process is not present in SMB-derived trend and can, therefore, be attributed to an accelerated dynamically induced ice loss.

Fig. 5.4 displays the ice trend corrected SMB- and GRACE-derived trends for four basins in the narrow AP. The inter-annual variations of the two datasets agree very well with a mean correlation of 0.7. The mean reduction of 39% confirms the presence of geophysical inter-annual signal induced by SMB in GRACE data. The biases are estimated to be negative, amounting to -15 Gt/yr. This mass loss is assumed to be driven by ice dynamics.

The trends for the remaining basins of WA are shown in Fig. 5.5. The Kamb Ice Stream with its glacier thickening is located in basin 18. For this basin, both GRACE and SMB derived rates are not correlated. The bias computed between the two time series is positive which is consistent with the geophysical knowledge regarding the build-up of ice in this area. After correcting the SMB-derived trend for glacier thickening of 18 Gt/yr, 46% of the GRACE-trend variance can be explained by SMB rates. A positive bias of 10 Gt/yr is estimated for the neighboring basin

19. Although the time-varying trends for both datasets exhibit similar behavior (correlation of 0.4 in Fig. 5.5d), the amplitude of SMB induced variations is considerably higher than those of GRACE, resulting in a negative reduction of GRACE trend WRMS for basin 19. For basin 23, which is located between ASE and AP, both datasets agree well resulting in -16 Gt/yr dynamically induced ice loss. In contrast, however, a positive bias of 2 Gt/yr is computed for basin 1 which is determined to be statistically insignificant (at the 95% level of confidence).

Trends for basins attributed to Queen Maud Land in EA are illustrated in Fig. 5.6. In this region, SMB explains on an average 43% of the GRACE trend WRMS (with a mean correlation of 0.8) emphasizing an excellent agreement between the two datasets that reveal the same geophysical variations. The computed bias is positive, indicating dynamic thickening in this region. Other possible sources for this bias can be underestimated GIA in Ch. 3 or underestimated linear trends in SMB, as was found to be the case for SMB generated from RACMO2.1 in Ch. 2. An interaction of all aforementioned sources might explain the positive bias as well.

Fig. 5.7 contains time-varying trends from SMB and GRACE derived for basins 11-14 in EA. In this region, SMB explains on an average 27% of the GRACE trend WRMS (with a mean correlation of 0.7) again confirming a good agreement between the two datasets. Biases are estimated to be positive, but small and for the three out of four basins statistically insignificant. Especially for basins 13 and 14, where relatively high mean trends for both GRACE and SMB are estimated, the difference between the two is negligibly small suggesting absence of ice dynamics. This can further be interpreted as an indication of reliably modeled SMB (constant trend and temporal variations) and correctly estimated GIA (Ch. 3) in these regions.

For the remaining eight basins (Fig. 5.8), which represent half of EA basins, the comparisons of the SMB- and GRACE-derived trends did not show good agreement, since either the GRACE trend WRMS was not reduced by subtracting SMB trend (resulting in negative  $R$  in Tab. 5.1) or the time-varying trends are uncorrelated (with a correlation smaller than 0.3). It can also be seen in Fig. 5.8 that for the most of these basins, one of the two datasets provide statistically insignificant (at the 95% level of confidence) mean trends, e.g. GRACE post-processed time-varying trend for basin 2 amounts to  $-0.2 \pm 0.8$  Gt/yr (Fig. 5.8a) or SMB-derived mean trend for basin 3 amounts to  $-0.5 \pm 0.4$  Gt/yr (Fig. 5.8b). A low signal-to-noise ratio might be responsible for a poor validation of the data in these basins. For the eight basins, subtracting SMB mean trend from that of GRACE results in the total dynamic-driven ice changes of 23 Gt/yr. These ice mass changes are not considered reliable, as the validation of SMB and GRACE temporal variations fails for reasons still under investigation. This also means that the corresponding uncertainties highlighted in Tab. 5.1 are not representative for these eight basins - an important conclusion enabled by comparing time-varying trends. To quantify dynamically induced mass changes over the entire ice sheet along with corresponding uncertainties, the estimated 23 Gt/yr (Fig. 5.8) are included along with a standard deviation of the same magnitude. This is justified by the fact that the eight basins with poor validation results contribute at least an error of 23 Gt/yr to

Table 5.1: Summary of statistics: Reduction ( $R_0$ ) of GRACE trend WRMS in % by SMB; correlation  $\rho$  between time-varying trends derived from GRACE and SMB; Reduction  $R$  of GRACE trend WRMS in % by  $SMB + ICE$ ; mean trend derived from GRACE and SMB with corresponding  $1\sigma$  standard deviation in Gt/yr for each basin, as well as estimated mean ice dynamics. To derive uncertainties for the mass changes integrated over the entire AIS (blue row), errors of the mean trend estimates were set to the magnitude of the corresponding estimated signal to reflect failed validation in the basins highlighted yellow.

basin	$R_0$ in %	$\rho$	$R$ in %	GRACE	$1\sigma_{GRACE}$	SMB	$1\sigma_{SMB}$	ICE	$1\sigma_{ICE}$
1	19	0.7	20	-1.2	1.4	-3.6	0.7	2.4	1.6
2	-105	0.3	-93	-0.2	0.8	-4.1	0.4	3.9	0.9
3	-25	-0.1	-5	16.7	1.7	-0.5	0.4	17.2	1.7
4	-13	0.2	-2	6.2	0.9	-0.8	0.3	6.9	1.0
5	18	0.6	22	0.8	0.5	-0.8	0.2	1.6	0.5
6	50	0.9	59	14.3	1.6	3.1	0.7	11.3	1.7
7	52	0.9	58	19.3	1.7	7.9	0.6	11.4	1.8
8	27	0.7	32	6.1	0.6	3.1	0.3	3.0	0.7
9	-96	0.0	-96	0.7	0.4	0.9	0.1	-0.2	0.4
10	-112	0.2	-100	5.3	0.7	0.6	0.2	4.7	0.7
11	26	0.8	26	0.9	0.5	0.1	0.1	0.8	0.5
12	24	0.8	25	1.6	1.6	-3.1	1.0	4.7	1.9
13	41	0.8	42	-20.7	2.0	-23.7	1.1	3.0	2.3
14	16	0.6	16	-12.7	1.8	-13.4	0.7	0.7	1.9
15	-10	0.0	44	-8.0	0.3	0.0	0.2	-8.0	0.3
16	-28	0.1	-9	-4.0	0.6	0.2	0.1	-4.2	0.6
17	4	0.2	4	-2.3	1.8	-4.8	0.5	2.5	1.9
18	-29	0.1	46	14.6	0.4	-3.4	0.3	18.0	0.5
19	-87	0.4	-44	6.7	0.7	-3.3	0.4	10.0	0.8
20	16	0.6	62	-35.5	1.1	-3.3	0.7	-32.1	1.3
21	4	0.8	83	-58.5	1.1	-0.4	0.8	-58.1	1.3
22	4	0.7	66	-56.4	1.2	1.1	0.8	-57.4	1.4
23	9	0.7	44	-15.1	0.7	1.1	0.4	-16.2	0.8
24	38	0.8	41	-6.2	0.8	-2.4	0.3	-3.8	0.9
25	29	0.7	43	-4.0	0.4	-0.8	0.1	-3.2	0.4
26	29	0.8	44	-6.0	0.6	-1.1	0.2	-4.9	0.6
27	25	0.6	29	-4.7	0.5	-1.5	0.1	-3.2	0.5
AIS				-142	15	-53	9	-89	24

the total dynamically induced mass changes. The same procedure was applied to SMB-induced and GRACE-derived surface mass changes that amount for the eight basins to -8.5 Gt/yr and 14.5 Gt/yr, respectively.

Based on the time-varying trends derived from GRACE and SMB for all Antarctic drainage systems for the time period from February 2003 to December 2011, total changes due to surface processes amount to  $-142 \pm 15$  Gt/yr, with  $-53 \pm 9$  Gt/yr and  $-89 \pm 24$  Gt/yr due to changes in the firn and ice layer, respectively.

### 5.3.2. GRACE - SMB - GPS

To compare GRACE-, SMB-, and GPS-derived trends at 10 Antarctic permanent GPS stations utilized in this study (Fig. 5.9), a similar procedure as described in Sec. 5.3.1 applies:

1. Subtract SMB-derived mean trend from that of GRACE while attributing the

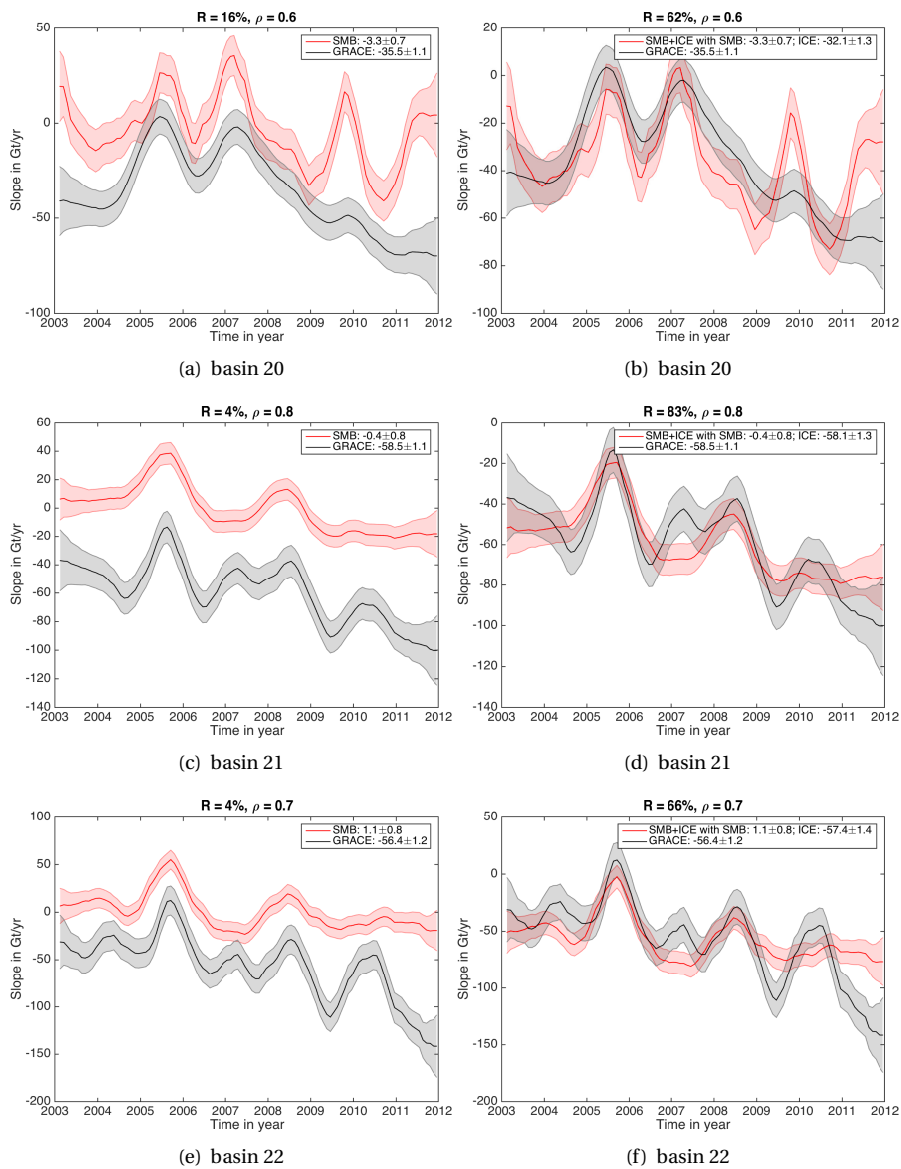


Figure 5.3: Time-varying slope estimated for GRACE and SMB with  $1\sigma$  time-varying error bars estimated for ASE: Thwaites and Smith Glaciers (basin 21), Pine Island Glacier (basin 22) and the coastal basin 20. Left: original estimates, right: after SMB-based slope is corrected for a constant bias

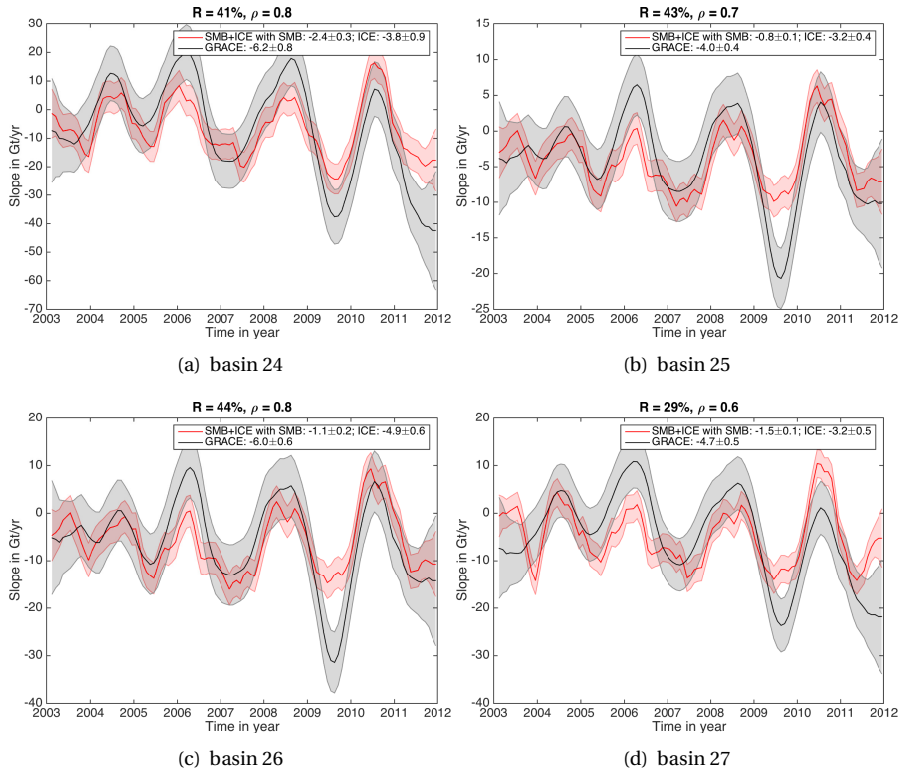


Figure 5.4: Time-varying slope estimated for GRACE and SMB with  $1\sigma$  time-varying error bars estimated for AP: basins 24-27. SMB-based slope has been corrected for a constant bias

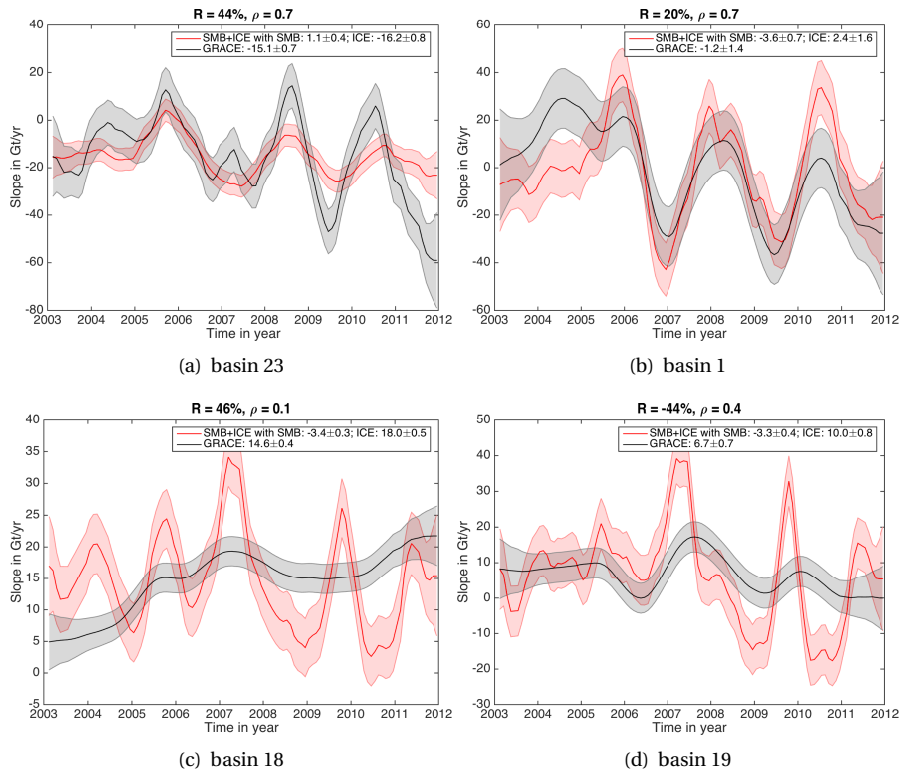


Figure 5.5: Time-varying slope estimated for GRACE and SMB with  $1\sigma$  time-varying error bars estimated for the coastal basin 23 and inland basins flowing into the Ross and Filchner Ronne Ice Shelves. SMB-based slope has been corrected for a constant bias

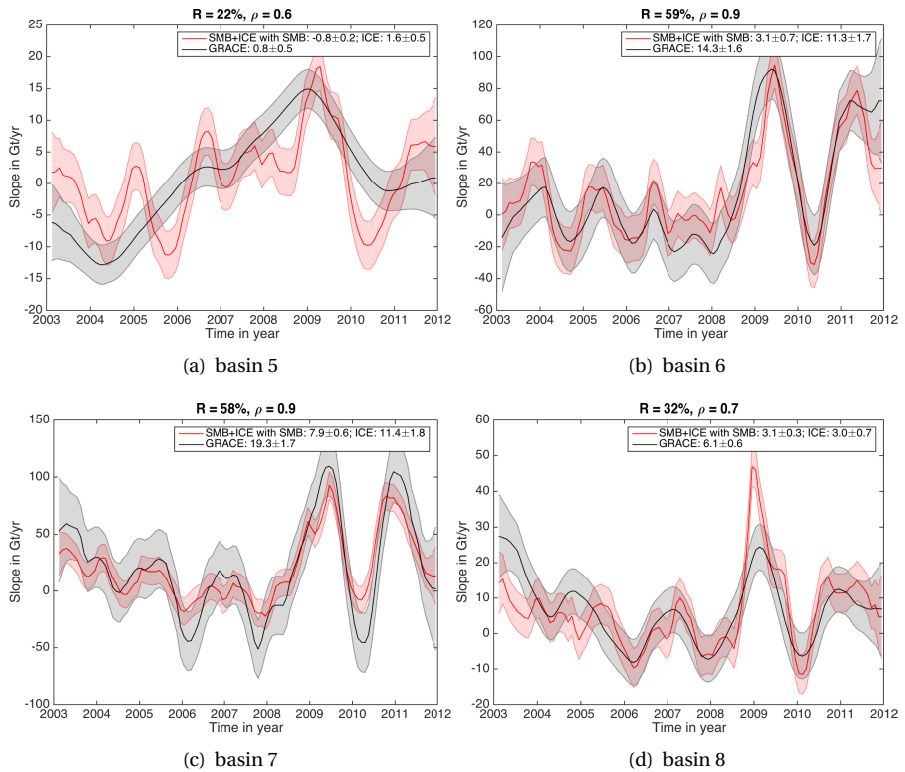


Figure 5.6: Time-varying slope estimated for GRACE and SMB with  $1\sigma$  time-varying error bars estimated in the Queen Maud Land of EA: Dronning Maud Land (basins 5 and 6), Enderby Land (basin 7) and Kemp Land (basin 8). SMB-based slope has been corrected for a constant bias

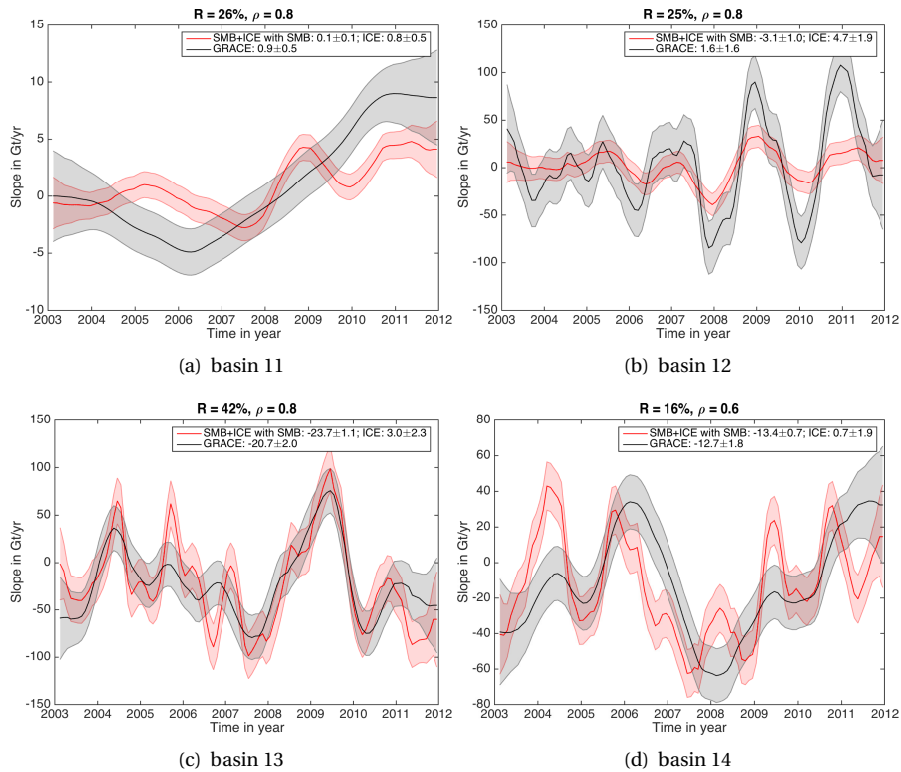


Figure 5.7: Time-varying slope estimated for GRACE and SMB with  $1\sigma$  time-varying error bars estimated in EA: Lambert (basins 11), Queen Mary Land (basin 12), Wilkes Land (basin 13), Terre Adèle and George V Land (basin 14). SMB-based slope has been corrected for a constant bias

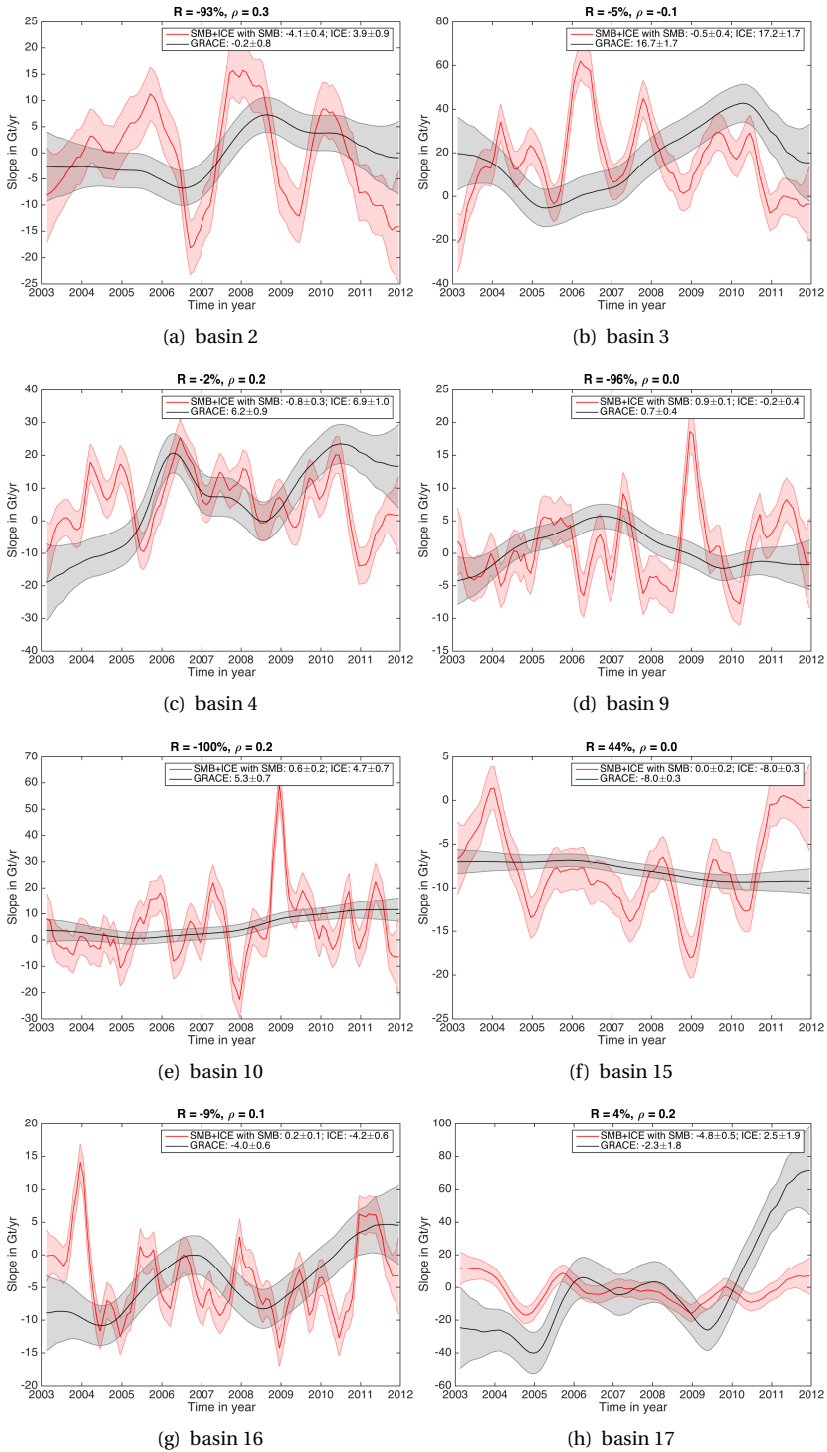


Figure 5.8: Time-varying slope estimated for GRACE and SMB with  $1\sigma$  time-varying error bars estimated in EA. SMB-based slope has been corrected for a constant bias

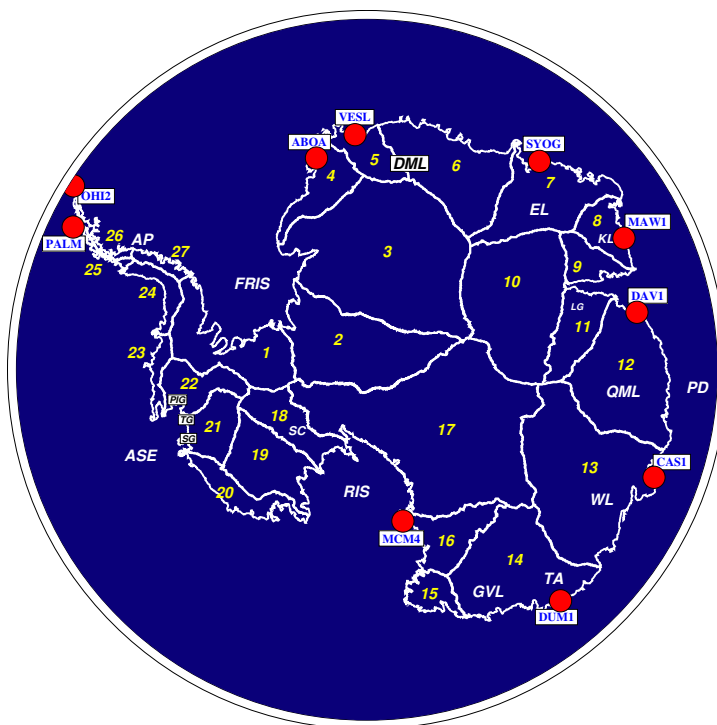


Figure 5.9: Antarctic drainage systems defined by Zwally et al (2012) together with the locations mentioned in the text as in Fig. 5.2. Circles represent the locations of the 10 analyzed GPS stations.

resulting bias to changes in ice dynamics.

2. Compute the reduction  $R$  of GRACE trend WRMS in percent by SMB+ICE and the correlation  $\rho$  between the two time-varying trends.
3. Subtract GRACE-derived mean trend from that of GPS yielding bias  $D$ .
4. Compute the reduction  $R_2$  of GPS trend WRMS in percent by GRACE+ $D$  and the correlation  $\rho_2$  between the two time-varying trends.

The time-varying trends corrected for biases and the resulting statistics are shown in Figures 5.10 - 5.12. In these figures, GPS-derived time-varying rates are corrected for degree-1,  $C_{20}$ , and atmospheric non-tidal variations. To highlight the agreement between GRACE- and SMB-derived time-varying trends at the locations of GPS stations, corresponding  $R$  and  $\rho$  are included in Figures 5.10 - 5.12.

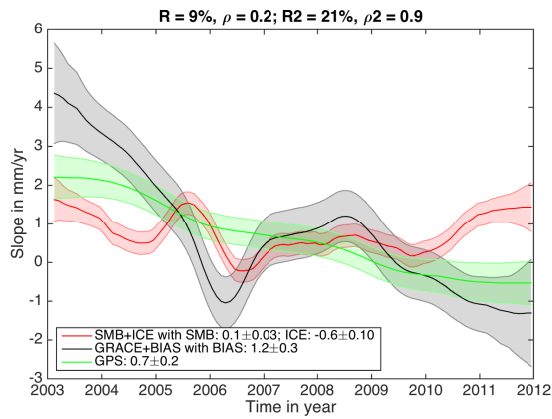
Generally, at all analyzed GPS stations, either the GRACE trend WRMS has been reduced by subtracting the trend from SMB+ICE (resulting in positive  $R$ ) or the time series are correlated with  $\rho \geq 0.3$ . SMB+ICE explains on an average 22% of the GRACE trend WRMS (the median for all stations is 32%) with a mean correlation of 0.6 (the median for all stations is 0.7) emphasizing a good agreement between

the two datasets not only if integrated over Antarctic drainage systems as shown in Sec. 5.3.1, but also if compared at the discrete points. The comparison of GRACE- and SMB-resolved variations with GPS-derived trends is more challenging. The main reason for this is that GPS are discrete point measurements that are sensitive to local effects, whereas GRACE and SMB results are spatially smoothed over the same range of patches (320 - 420 km).

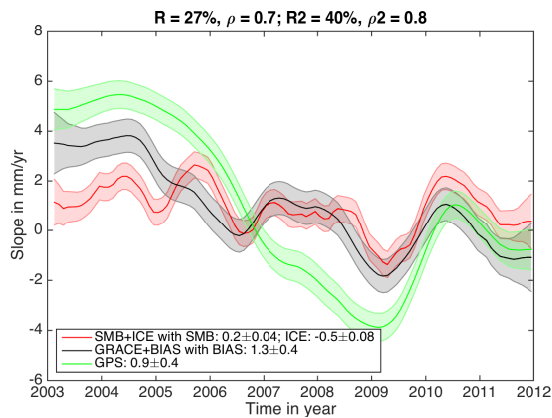
Fig. 5.10 shows vertical deformations derived at the three GPS-stations located in Queen Maud Land of EA (Fig. 5.9). The displacements derived at the ABOA station (Fig. 5.10a), which is located in Western Queen Maud Land, show similar variations to those derived at the VESL station (Fig. 5.10b), which is ca. 400 km apart. GPS- and GRACE-derived time-varying trends for both GPS stations are highly correlated with 21% and 40% of GPS variance being explained by GRACE at the ABOA and VESL station, respectively. At SYOG station (Fig. 5.10c), SMB-, GRACE- and GPS-derived variations exhibit a similar evolution, starting approximately from the middle of 2005. The elastic subsidence of solid Earth as an immediate response to the reported accumulation event in 2009 (Lenaerts et al, 2013), is captured by all three independent techniques at both VESL and SYOG stations. The magnitude of the derived GPS signal in Fig. 5.10 is comparable to the signals recovered from SMB and GRACE data after applying the patch approach.

Fig. 5.11 displays the evolution in vertical deformation derived for OHI2 and PALM station in the AP, as well as for MCM4 GPS-station located on the volcanically active Ross Island. SMB+ICE explains more than 40% of the GRACE trend WRMS at the GPS stations in the AP. SMB- and GRACE-derived trends are highly correlated for these two stations which is not unexpected, as they are located ca. 350 km apart in the narrow AP while range of 320-420 km was used for the patch approach (based on findings in Ch. 3). GPS-derived trends, however, differ substantially both between the stations and from SMB- and GRACE-derived trends. According to GPS-derived trends at OHI2, a pronounced mass loss should have taken place in January 2009 to induce an elastic uplift of such a high magnitude with its peak at 36 mm/yr. This event is captured by GRACE and SMB as well, but in July 2009 and with considerably lower magnitude. It is interesting to note that at the PALM station, the same event is captured by all three independent techniques with similar magnitude around July 2009. One year later (around July 2010), at OHI2 and PALM stations all three techniques report a subsidence of the solid Earth as an immediate response to a high level of accumulation. Accelerating rates are observed by GPS at the PALM station starting from the begin of the analyzed time span and continuing approximately till the mid of 2007. This positive acceleration might be attributed to the breakup of the Larsen B Ice Shelf in 2002 (Thomas et al, 2011). At MCM4, also an accelerated process, which is potentially related to the active volcano in the proximity of the station, is observed by GPS, but neither GRACE nor SMB capture it. A mass loss event, however, is observed by both GPS and GRACE around the beginning of 2008, but appears approximately three time more intense in GPS than in GRACE data.

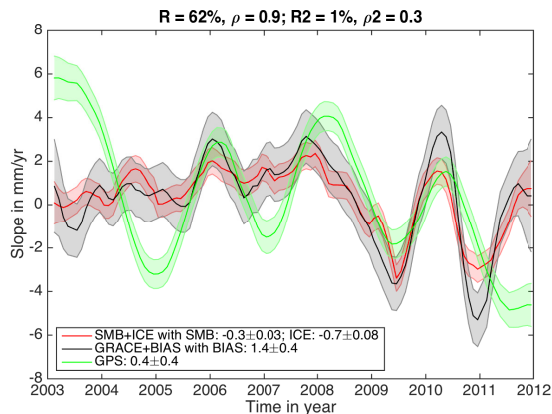
Fig. 5.12 shows time varying trends derived at the GPS stations located in EA. Both GPS and GRACE seem to observe the same geophysical processes with simi-



(a) ABOA

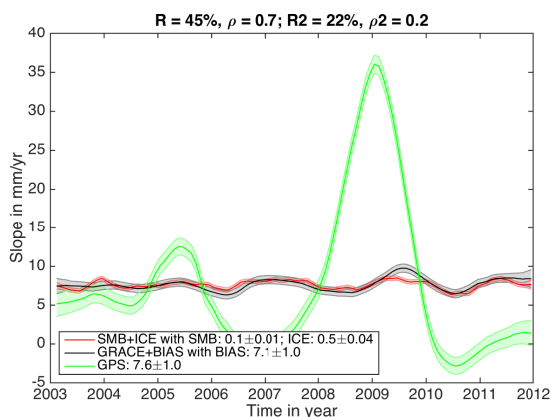


(b) Vesleskarvet (VESL)

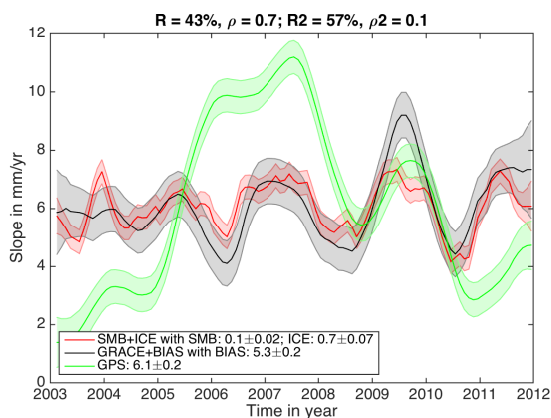


(c) Syowa (SYOG)

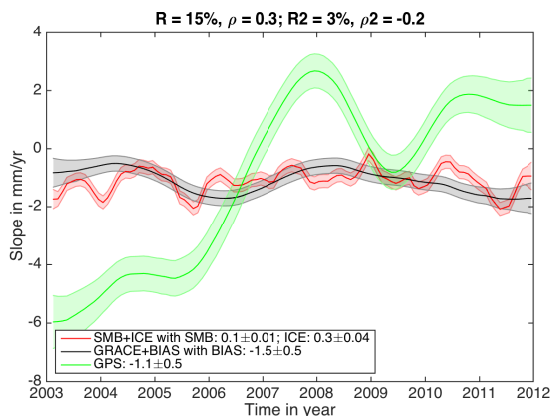
Figure 5.10: Time-varying slope estimated for GRACE, SMB, and GPS with  $1\sigma$  time-varying error bars.  $R$  is reduction of GRACE trend WRMS in % by SMB+ICE with the correlation  $\rho$  between the two time-varying trends.  $R2$  is reduction of GPS trend WRMS in % by GRACE+D with the correlation  $\rho2$  between the two time-varying trends



(a) O'Higgins Base (OHI2)



(b) Palmer station (PALM)



(c) McMurdo Base (MCM4)

Figure 5.11: Time-varying slope estimated for GRACE, SMB, and GPS with  $1\sigma$  time-varying error bars.  $R$  is reduction of GRACE trend WRMS in % by SMB+ICE with the correlation  $\rho$  between the two time-varying trends.  $R2$  is reduction of GPS trend WRMS in % by GRACE+D with the correlation  $\rho2$  between the two time-varying trends

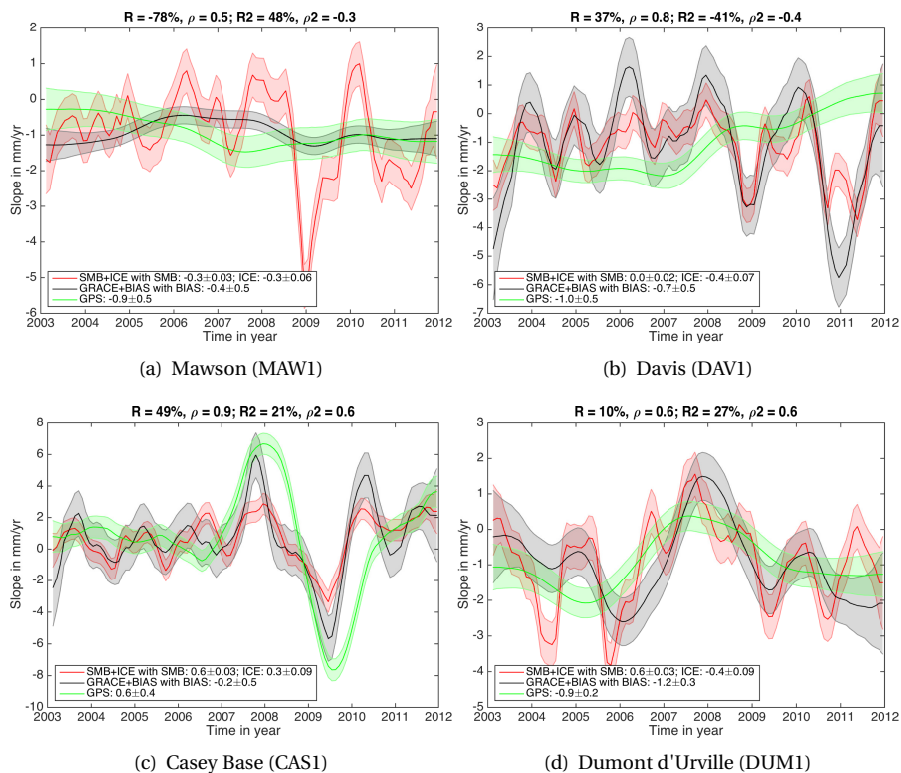


Figure 5.12: Time-varying slope estimated for GRACE, SMB, and GPS with  $1\sigma$  time-varying error bars.  $R$  is the reduction of GRACE trend WRMS in % by SMB+ICE and  $\rho$  is correlation.  $R2$  is reduction of GPS trend WRMS in % by GRACE+D with the correlation  $\rho2$

Table 5.2: Reduction ( $R$ ) of GPS trend WRMS in % by GRACE after being corrected for  $D$ . Correlation  $\rho$  between GPS- and GRACE-derived trends. Averaged time-varying trend derived from GPS time series that has been stepwise corrected for degree-1,  $C_{20}$ , and non-tidal atmospheric loading (ATM).

	GPS			GPS-deg1			GPS-deg1- $C_{20}$			GPS-deg1- $C_{20}$ -ATM		
	$\rho$	$R$	mean trend	$\rho$	$R$	mean trend	$\rho$	$R$	mean trend	$\rho$	$R$	mean trend
ABOA	0.8	17	1.3	0.8	24	1.3	0.9	16	0.7	0.9	21	0.7
CAS1	0.6	26	1.2	0.6	25	1.2	0.6	21	0.6	0.6	21	0.6
DAV1	-0.3	-69	-0.5	-0.3	-72	-0.5	-0.4	-38	-1.1	-0.4	-41	-1.0
DUM1	0.4	-7	-0.4	0.5	-1	-0.4	0.6	27	-0.9	0.6	27	-0.9
MAW1	-0.1	18	-0.4	-0.3	15	-0.4	-0.3	50	-1.0	-0.3	48	-0.9
PALM	0.1	58	6.7	0.1	59	6.7	0.1	57	6.2	0.1	57	6.1
SYOG	0.3	7	0.9	0.3	6	0.9	0.3	1	0.3	0.3	1	0.4
VESL	0.8	45	1.5	0.8	45	1.5	0.8	40	0.9	0.8	40	0.9
MCM4	-0.3	-2	-0.5	-0.3	-2	-0.6	-0.2	4	-1.2	-0.2	3	-1.1
OHI2	0.2	24	8.2	0.2	24	8.2	0.2	22	7.7	0.2	22	7.6

lar magnitude at the CAS1 station in Wilkes Land (Fig. 5.12c). All three techniques capture small-scale accumulation variability modeled by SMB at this GPS location. Please note the improved agreement between the magnitude of the peaks derived from GRACE and GPS rates in Fig. 5.12c compared to the results shown in Fig. 4.9. The better agreement is mainly caused by the dynamic patch approach applied to the GRACE data, which localizes the signal and thus, improves its recovery. Good agreement between all three techniques is also evident at the DUM1 stations where 27% of GPS variance is explained by GRACE and 10% of GRACE variance is explained by SMB. The correlation between all three techniques is 0.6 at this station. At the MAW1 station, trends based on GRACE and GPS do not reflect high variations modeled by SMB and lie within  $1\sigma$  range starting from 2008. At the DAV1 station, 37% of GRACE variance is explained by SMB while GPS seems to be insensitive to these variations within the firn layer. Instead, GPS-derived trend is almost constant for the time span between 2003-2007 with an almost constant acceleration from 2007 to the end of 2011.

In summary, it can be stated that for five out of ten analyzed GPS stations there is a good agreement between the temporal variations derived from three independent techniques. Tab. 5.2 provides an overview about the influence of applying different corrections to the mean GPS trend on its agreement with GRACE-derived trends. Without applying any corrections to GPS derived rates, at seven of ten analyzed GPS stations, the GPS trend WRMS has been reduced by subtracting the trend from GRACE. The reduction of GPS trend WRMS is slightly enhanced for ABOA, DUM1, PALM and decreased for CAS1, DAV1, MAW1, and SYOG stations after removing degree-1 from GPS derived rates. After additionally removing  $C_{20}$  from GPS based trends, at nine of ten analyzed GPS stations the GPS trend WRMS has been reduced by subtracting the trend from GRACE with a considerably increased reduction for four stations: from -72% to -38% for DAV1, from -1% to 27% for DUM1, from -2% to 4% for MCM4, and from 15% to 50% for MAW1 station. For the remaining stations, the reduction of GPS trend WRMS was lowered by additionally removing  $C_{20}$  from GPS-based trends. Additionally removing atmospheric non-tidal variations from GPS-derived rates only causes significant changes for the CAS1 station by enhanced reduction of GPS trend WRMS from 16% to 21%. For all

Table 5.3: Summary of the derived mean trends for GPS, GRACE, and for GIA derived in Ch. 3 at the analyzed GPS stations.  $D$  is the mean difference computed by subtracting GRACE-derived rates from those based on GPS. Unit is mm/yr.

	GPS-deg1- $C_{20}$ -ATM	GRACE	$D$	$h_{gia}$ (Ch. 3)
ABOA	$0.7 \pm 0.6$	$-0.5 \pm 0.1$	$1.2 \pm 0.6$	$1.4 \pm 0.3$
CAS1	$0.6 \pm 0.7$	$0.9 \pm 0.1$	$-0.2 \pm 0.8$	$5.3 \pm 0.5$
DAV1	$-1 \pm 0.8$	$-0.4 \pm 0.1$	$-0.7 \pm 0.8$	$4.6 \pm 0.4$
DUM1	$-0.9 \pm 0.6$	$0.2 \pm 0.1$	$-1.2 \pm 0.7$	$1.7 \pm 0.4$
MAW1	$-0.9 \pm 0.8$	$-0.6 \pm 0.1$	$-0.4 \pm 0.8$	$1.1 \pm 0.4$
PALM	$6.1 \pm 0.6$	$0.8 \pm 0.1$	$5.3 \pm 0.6$	$-2.5 \pm 0.5$
SYOG	$0.4 \pm 0.7$	$-1.1 \pm 0.1$	$1.4 \pm 0.7$	$2.7 \pm 0.4$
VESL	$0.9 \pm 0.7$	$-0.4 \pm 0.1$	$1.3 \pm 0.7$	$5.3 \pm 0.3$
MCM4	$-1.1 \pm 0.8$	$0.4 \pm 0.04$	$-1.5 \pm 0.8$	$0.7 \pm 0.3$
OHI2	$7.6 \pm 1.2$	$0.5 \pm 0.04$	$7.1 \pm 1.2$	$-2.9 \pm 0.4$

corrections, the correlation between GRACE and stepwise corrected GPS trends did not change significantly. Additional corrections for  $C_{20}$ , however, did influence GPS-derived mean trend on average by 0.6 mm/yr emphasizing the importance of accurately estimated changes at low degree spherical harmonics. Since the bias of 0.6 mm/yr did not systematically yield better or worse agreement between GRACE and GPS trends, but systematically lowered the mean trend derived from GPS, it will be considered as an additional error source when deriving standard deviation for GPS-deg1- $C_{20}$  for further analysis.

Tab. 5.3 summarizes the derived mean trends from GPS corrected for degree-1,  $C_{20}$ , and non-tidal atmospheric loading (ATM) with corresponding uncertainties that are updated to include an additional error of 0.6 mm/yr (in contrast to Figures 5.10 - 5.12). Furthermore, Tab. 5.3 contains GRACE-derived trends corrected for GIA, as well as GIA trends derived in Ch. 3 at the analyzed GPS stations. The mean difference  $D$  computed by subtracting GRACE-derived rates from those based on GPS should ideally be comparable with the GIA derived in Ch. 3. This requires, among others, that (i) GRACE-derived rates are sufficient for correcting GPS from secular trend and non-linear variations in elastic deformation, (ii) degree-1 and  $C_{20}$  sufficiently approximate non-Antarctic leakage yielding GPS to be regionalized to Antarctica, (iii) GPS measurements are not corrupted by local effects or technical artifacts, and (iv) GRACE and GPS are in an equivalent reference frame after having removed degree-1.

The estimated  $D$  indeed agrees within  $1\sigma$  with  $h_{gia}$  derived in Ch. 3 at ABOA and MAW1 stations, and within two standard deviations at the SYOG and MCM4 station. A significant  $D$  (at the 95% level of confidence), however, is estimated for only two GPS stations in the AP, OHI2 and PALM. At these stations,  $h_{gia}$  is estimated to be negative while  $D$  is estimated to be positive and approximately two times larger. Interesting to note is that at seven out of ten analyzed GPS stations, the estimated  $D$  and derived  $h_{gia}$  (in Ch. 3) trend differs in sign. In fact, this also applies to CAS1 and DUM1 stations at which a good resemblance was found between GPS and GRACE in terms of temporal variations (Fig. 5.12c,d). This means that, although GRACE-derived rates might be sufficient for correcting GPS

from non-linear variations in elastic deformation, a secular trend (or systematic bias) between GRACE- and GPS-derived trends exists. This trend can be caused by local effects not captured by homogeneous GRACE-derived deformations, by remaining far-field signal, by mm-level unknown biases at low degree spherical harmonics, by differences in reference frames, by technical artifacts (or is most likely the interaction of all aforementioned components). Therefore, without additional analysis the difference between the GPS- and GRACE-derived rates cannot be fully attributed to GIA-induced vertical deformation. The mm-level unknown biases emphasize the limitations of using GPS data to constrain Antarctic GIA, although a good agreement between GPS, SMB, and GRACE is found for 50% of analyzed GPS stations when examining time-varying rates. However, such comparisons of time-varying trends derived from GPS against GRACE-derived time-varying trends could shed light on the geophysical plausibility of different time series (e.g., degree-1,  $C_{20}$ ) used to correct GPS.

## 5.4. DISCUSSION

### 5.4.1. GRACE - SMB

Three classes of basins are shown in Fig. 5.13 summarizing the validation results presented in Sec. 5.3.1. The first class (white) represents basins where good agreement between temporal variations derived from SMB and GIA-corrected GRACE time series was found. Statistically significant ice mass changes were derived for these basins (Tab. 5.1). The second class (blue) represents basins with a good agreement between SMB- and GRACE-derived time-varying rates, but with statistically insignificant (at the 95% level of confidence) derived ice mass changes. These basins, therefore, contribute a large uncertainty to the total dynamically induced mass change estimates. The third class (orange) are basins where significant disagreement between SMB- and GRACE-derived time-varying rates was found. The corresponding estimated amount of the derived (ice) mass changes was set to contribute to the total Antarctic ice-mass change estimate with a standard deviation of the same magnitude. A low signal-to-noise ratio is likely responsible for a poor validation of the data in these basins.

An overall good agreement between temporal variations derived from SMB and GIA-corrected GRACE time series for 19 out of 27 basins during the time period of almost 9 years demonstrates the reliability of modeled temporal variations by RACMO. On the other hand, it also demonstrates the capability of gravity data to constrain the evolution of surface mass changes at the level of drainage systems. Although the high correlation of time-varying rates from independent datasets significantly increases confidence in these data, conclusions regarding the secular part of the time-varying trend remain challenging. This is due to the fact that a constant trend would manifest itself as a systematic 'bias' by shifting the curves shown in Figures 5.3-5.8 up or down. This means that each under- or overestimated constant rate in GIA or SMB would directly propagate into the derived ice dynamics. Sutterley et al (2014) provide an independent assessment of dynamically-induced mass changes for basins 21 and 22 in ASE. Their estimated

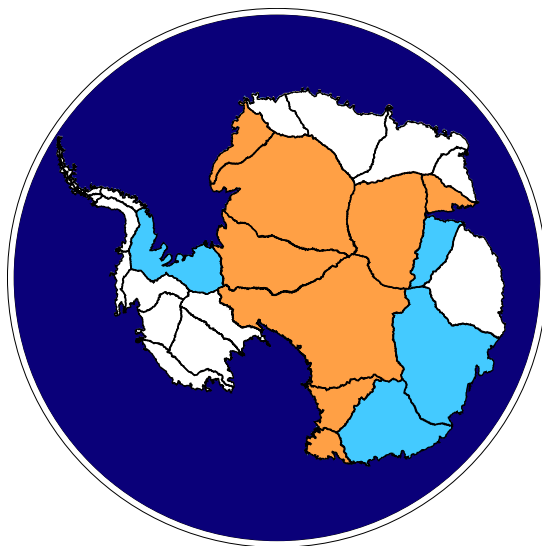


Figure 5.13: Antarctic drainage systems divided into three classes: white - good agreement between SMB- and GRACE-derived time-varying rates with statistically significant derived ice mass changes; blue - insignificant ice mass changes despite good agreement between SMB- and GRACE-derived time-varying rates; orange- significant disagreement.

mass loss from the mass budget method mainly represents dynamically-induced mass changes due to negligible surface runoff in Antarctica (Lenaerts et al, 2012). Over the same time period, Sutterley et al (2014) estimated the mass balance of these basins to amount to  $-105 \pm 6$  Gt/yr, which agrees reasonably well with the  $-115.5 \pm 2$  Gt/yr estimated in this study increasing the confidence in constant rates derived for SMB and GIA signal in this region.

For basin 13 in Wilkes Land, SMB and GRACE time series were compared by Williams et al (2014) and Velicogna et al (2014). Williams et al (2014) found a good agreement between the two datasets only for years 2008-2010 stating that the changes in this region are driven by surface processes and not ice dynamics. Velicogna et al (2014) found a good agreement for the entire period of January 2003 to July 2012, but emphasized discrepancies in the derived constant accelerations from the two time series attributing them to ice dynamics. The time-varying trends for basin 13 (Fig. 5.7c) (i) show an excellent agreement between GRACE and SMB for the entire investigated period from February 2003 to December 2011, (ii) suggest the absence of constant acceleration for this time frame, and (iii) confirm that the changes in this area are entirely driven by surface processes. These results demonstrate the importance of an adequate approach utilized to compare different data sets, as analyzing time-varying trends provides more insights into the geophysical processes.

The reported strong accumulation events such as in 2005 in ASE, WA (Horwath et al, 2012) or in 2009 and 2011 in Dronning Maud Land, EA (Lenaerts et al, 2013) are clearly captured by both GRACE- and SMB-derived time-varying trends. The

Table 5.4: Comparison of the results derived in this chapter for 2003-2011 with surface mass balance (SMB) and ice dynamic rates (ICE) from Zwally et al (2015) and Martín-Español et al (2016b) for 2003-2008 and 2003-2013, respectively. Unit is Gt/yr.

	ICE			SMB		
	Zw15	ME16	OD17	Zw15	ME16	OD17
EA	147±34	17.9±9.8	59.4 ±23.3	-11±6	38.5±19.5	-35.4±8.7
WA	-42±23	-100.9±6.1	-133.6±3.1	17±9	-12.4±10.3	-11.9±1.7
AP	-27±3	-29.5±3.9	-15±1.2	-2±1	1.5±7.1	-5.8±0.4

derived dynamically-induced mass changes confirm prominent Antarctic features, such as dynamic thinning in ASE and AP and thickening in Kamb Ice Stream.

The results presented in this chapter confirm the findings of Wouters et al (2013) that the most GRACE-observed changes in Antarctica are controlled by SMB, but also suggest that there is no constant acceleration over the investigated time frame. This might explain why Wouters et al (2013) and Velicogna et al (2014) could not detect a projectable linear acceleration with the existing GRACE time series.

A comparison of SMB and ice dynamic rates derived in this chapter (abbreviated as OD17 hereafter) with the most recent Antarctic estimates derived by Zw15 (Zwally et al, 2015) and ME16 (Martín-Español et al, 2016b), highlights the discrepancies of the current assessments for AIS. ME16 used forward models to constrain the spatiotemporal variability of geophysical processes while combining altimetry, gravimetry, and GPS data over the time period of 2003-2013. Zw15 combined altimetry along with meteorological reanalysis data for 2003-2008. The corresponding results are summarized in Tab. 5.4 for EA, WA, and AP. One should keep in mind that different data, methodologies, and assumptions were used to derive SMB and dynamic-driven mass changes, and that also the time period under investigation is different. Nevertheless, SMB derived for WA and AP lies within  $1\sigma$  interval between OD17 and ME16. A negative SMB trend in AP of  $-2\pm 1$  Gt/yr estimated by Zw15 is also in the  $1\sigma$  range of estimates based on OD17 and ME16. In WA, Zw15 estimates a positive mass balance in contrast to other two studies. Ice dynamics derived for WA and AP agree in sign between the three studies, but lie within  $1\sigma$  interval only for AP from ME16 and Zw15. For the large area of EA with a poor signal-to-noise ratio in its interior, the three studies differ significantly regarding both SMB and ice dynamic rates. SMB derived from OD17 agrees in sign with that of Zw15 contrary to ME16. The hypothesis of EA dynamic thickening by Zwally et al (2015) is more supported by OD17 than by ME16, although non of them lie within  $1\sigma$  interval.

To replicate the dynamic thickening hypothesis suggested by Zwally et al (2015), Martín-Español et al (2017) used the same approach as Martín-Español et al (2016b), but set different constraints to EA dynamic thickening while using SMB from RACMO as an a-priori solution. They estimated the dynamic trend to amount to  $80\pm 6$  Gt/yr when SMB was constrained with RACMO2.3, and to  $55\pm 6$  Gt/yr when SMB was constrained with RACMO2.4. In this chapter derived ice dynamics of  $59.4\pm 23.3$  Gt/yr lie within  $1\sigma$  interval from both of their estimates highlighting the importance of a sophisticated validation that allowed less reliable regions to be identified and corresponding uncertainties to be adjusted.

### 5.4.2. GRACE - SMB - GPS

At the locations of analyzed GPS stations, the comparison of GRACE- versus SMB-derived time-varying rates demonstrates the capability of GRACE data to resolve temporal variations of the Antarctic precipitation and increases confidence in SMB-modeled fluctuations. The evolution of vertical deformations derived from GPS, GRACE, and SMB reveals a good agreement for five out of ten analyzed GPS stations, although conclusions regarding the secular part of time-varying trend remain challenging. Nevertheless, visual comparisons of the derived temporal variations suggest a potential for providing a better understanding of geophysical processes.

Visual inspection of time-varying trends derived at the ABOA station suggests almost constant negative acceleration being observed by GPS. This is because the derived time-varying trend seems to change with a similar rate over the investigated time period (Fig. 5.10a). This negative acceleration is not contained in the SMB-derived rates, but in those from GRACE, and can be attributed to ice thickening. Dynamically induced thickening is also confirmed by elastic subsidence of  $-0.6 \pm 0.1$  mm/yr when subtracting SMB-derived mean trend from that of GRACE (Fig. 5.10a). Similar behaviour is observed at the VESL station between 2003-2009 prior to the large accumulation event in 2009. Also here the elastic subsidence is estimated to amount to  $-0.5 \pm 0.1$  mm/yr. ABOA and VESL stations are located in the basins 4 and 5, respectively, for which in Sec. 5.3.1 a dynamic thickening in terms of Gt/yr is estimated (Tab. 5.1). The estimates favourably compare with those derived by (Zwally et al, 2015). Zw15 derived  $8 \pm 4$  Gt/yr and  $4 \pm 3$  Gt/yr for basin 4 and 5, respectively. The mass changes derived in Sec. 5.3.1 amount to  $6.9 \pm 1$  Gt/yr and  $1.6 \pm 0.5$  Gt/yr for these basins.

When examining time-varying rates derived from GPS at the OHI2 and PALM stations in AP (Fig. 5.11a, b), it is evident that most likely regional variations yield variations of such a large magnitude as the peak in 2009 at the OHI2 station or in 2008 at the PALM station. If not accounting for the time span between 2008 to 2010 when computing mean trend at the OHI2 station, the resulting trend is halved. This example shows that local effects might significantly influence the estimated mean trend which, if used to constrain Antarctic GIA or to explain elastic deformation, might yield erroneous results. An inter-comparison, as provided in this chapter, can shed light on the processes contained in the analyzed time series.

## 5.5. CONCLUSIONS

Time-varying rates derived from GRACE and SMB data over Antarctic drainage systems reflect primarily variations within the firn layer governed by changes in precipitation rates. The performed validation allowed regions to be identified where GRACE and SMB capture the same temporal variations, which turned out to be the case for 19 out of 27 (70%) Antarctic drainage systems. After correcting SMB for a bias attributed to the changes in ice dynamics, SMB explained at an average 40% of GRACE-derived trend WRMS with a mean correlation of 0.7 between the two datasets in these 19 basins. The level of agreement not only validates modelled SMB variations, but is also an indication of reliably modeled constant SMB and

correctly estimated GIA in the most of Antarctic basins when geophysical knowledge about the prominent Antarctic features is accounted for.

Based on the time-varying trends derived from GRACE and SMB for all Antarctic drainage systems for the time period from February 2003 to December 2011, total changes due to surface processes amount to  $-142 \pm 15$  Gt/yr, with  $-53 \pm 9$  Gt/yr and  $-89 \pm 24$  Gt/yr being attributed to changes in the firn layer and in ice dynamics, respectively.

The inter-comparison of time-varying rates derived from GRACE, SMB, and GPS data at the locations of ten permanent GPS stations demonstrates the potential of GRACE data to be used for correcting GPS derived non-linear rates for elastic uplift, as for half of the analyzed GPS stations both GPS and GRACE were observing the same geophysical process with a signal of similar magnitude. Such an inter-comparison can help decide whether the observed power in the GPS time series at the low frequencies is caused by inaccurately modeled colored noise or is due to geophysical variations. Nevertheless, an interaction of secular trends, that are believed to originate from different sources, manifests itself as a systematic bias between the two datasets. Separating those constant trends is a challenging task that requires further research before GPS data can be utilized to explicitly constrain Antarctic GIA.

# 6

## CONCLUSIONS AND RECOMMENDATIONS

The work presented in this thesis sought to develop a refined methodology for separating the glacial isostatic adjustment (GIA) and ice-mass change signals in Antarctica by exploiting the strengths of independent data sets, such as those from gravimetry, altimetry, climate data, and others. This chapter highlights the most important products and findings of the work completed toward achieving the main goal and provides suggestions for future work.

### 6.1. CONCLUSIONS

In Ch. 2, the approach developed by [Riva et al \(2009\)](#) for estimating present-day GIA and ice mass change over Antarctica using a combination of satellite altimetry and gravimetry was revisited. In addition to the fact that reprocessed and extended satellite gravity and altimetry data sets were used, the key elements of the modified combination approach are an improved estimate of surface processes by incorporating a regional atmospheric climate model (RACMO2) and accompanying firn densification model, as well as a calibration of the results to a low-precipitation zone in East Antarctica (EA). The latter helped reducing the impact of the mm-level unknown biases (e.g. geocenter motion,  $C_{20}$ , errors in the ICESat campaign bias) inherent to the satellite data sets. The empirically derived GIA models are compared to a set of Antarctic GNSS site displacements, as well as to traditionally derived Antarctic GIA models. The main result is an empirically derived regional Antarctic GIA model with corresponding uncertainties, which suggests the presence of strong uplift in the Amundsen Sea and Philippi/Denman sectors, as well as subsidence in large parts of East Antarctica. The strong uplift was not present in the forward GIA models. This is because most forward GIA models do not treat ice load variations within the past thousand years, suggesting the uplift observed could be a product of more recent ice load changes.

The work of Ch. 2 was published in [Gunter et al \(2014\)](#). The GIA solution based on the CSR RL05 DDK5 field has already been distributed to the community and used for comparison in a range of recent studies, such as in [Schoen et al \(2015\)](#), [Wolstencroft et al \(2015\)](#), [Nield et al \(2016\)](#), and [Martín-Español et al \(2016a\)](#). The idea of calibrating results to a low-precipitation zone in EA was established and later used in e.g., [Groh et al \(2014\)](#). Furthermore, one of the secondary results are the elastic uplift rates derived based on the ICESat-RACMO combination, which were used by [Wolstencroft et al \(2015\)](#) for correcting GPS.

To improve the spatial resolution of the derived GIA and ice mass changes, a dynamic patch approach was developed in Ch. 3. The approach uses the relationship between the different datasets from Ch. 2, but the combination of GRACE with ICESat-RACMO data is performed at the satellite altitude in terms of gravity disturbances. GIA and ice mass changes are parameterized on the Earth's surface using geophysical boundaries and estimated by using weighted least-squares adjustment. GPS-derived uplift rates are implicitly incorporated into the combination to help defining the pattern of estimated present-day GIA. The dynamic patch approach that consistently combines data featuring different spatial resolution, allowed, for the first time, small-scale features in Antarctic GIA to be detected. Entirely new in the empirical GIA solution is a pronounced subsidence in the proximity of Kamb Ice Stream likely as a response to the Late Holocene loading related to stagnation and reactivation of ice streams in this area as reported by [Nield et al \(2016\)](#).

To better quantify the ice mass change variations in time, a stochastic approach for time series analysis was developed in Ch. 4 that allows for physically natural variations of signal constituents in time. This work has been published in [Didova et al \(2016\)](#). The results suggested that the developed technique provides more reliable trend estimates compared to the commonly used least-squares adjustment, as well as more physically valuable interpretations, while validating independent observing systems. In Ch. 5, this technique was used to derive ice mass changes at the level of drainage systems through a validation of time-varying trends derived from GRACE and SMB (surface mass balance modeled by RACMO), as opposed to dealing only with long-term linear trends. This analysis revealed an excellent agreement between GRACE- and SMB-derived rates for 70% of the Antarctic drainage systems, thus highlighting the reliability of the modeled temporal variations in SMB from RACMO. The sophisticated validation allowed regions with significant disagreement (30% of the Antarctic drainage systems) to be identified and corresponding uncertainties to be adjusted. The difference between the GIA-corrected GRACE time-varying trends and those derived from SMB is interpreted as ice dynamics yielding basin-wise estimates for dynamically-induced mass changes over the time period February 2003 - December 2011.

To gain insight into the regional variations, SMB- and GRACE-derived time-varying trends were compared to those derived from GPS measurements at the ten permanent GPS stations. The main outcome was a successful validation of temporal variations from SMB and GRACE at the discrete point measurements. The evolution of vertical deformations derived from GPS, GRACE, and SMB revealed a

good agreement for 50% of analyzed GPS stations demonstrating the potential of GRACE data to be used for correcting GPS derived rates for non-linear variations in elastic uplift. When attributing the difference between GPS and GRACE to GIA and comparing the results with those derived in Ch. 3, a mm-level bias is found. This difference can be caused by local effects (present in time-varying trends derived from GPS, but not captured by homogeneous GRACE-derived deformations), by remaining far-field signal, by mm-level unknown biases at low degree spherical harmonics, by differences in reference frames, by technical artifacts (or is most likely the interaction of all aforementioned components). Therefore, additional analysis is required prior to explicitly use GPS data to constrain Antarctic GIA.

Generally, it can be concluded that the patch approach suggested in Ch. 3 provides a localized GRACE signal with a comparable order of magnitude as the discrete GPS measurements for 50% of the analyzed GPS stations. Furthermore, it enables a consistent combination and/or comparison of GRACE with data that feature higher spatial resolution. Therefore, the combination of dynamic patch approach (Ch. 3) with the stochastic time series analysis (Ch. 4), provides a sophisticated tool for validating data exhibiting different spatio-temporal resolution and different noise characteristics. The results shed light on the strengths and weaknesses of different data and provide an improved understanding of the evolution of Antarctic geophysical processes. Moreover, both approaches are not only applicable in the context of estimating GIA and ice-mass changes in Antarctica, but can also be used in any other context where GRACE data and any other geodetic time series are involved.

## 6.2. RECOMMENDATIONS

- The validation performed in Ch. 5, based on which ice dynamics were estimated, was limited to the time span of the utilized DMT2 GRACE solutions (to the end of 2011). This is because the high quality of these GRACE solutions and their noise description has been validated in (Farahani et al, 2016). However, an extended time series analysis would provide more accurate results with more insights into the recent geophysical processes. For this, GRACE solutions produced at the Technical University of Graz (Mayer-Gürr et al, 2014) could be used. Since an accurate noise description is essential for reliable patch approach outputs (Ch. 3), the stochastic properties of these solutions would need to be validated first.
- It might be worth investigating whether additional regularization, such as Tikhonov regularization, in Ch. 3 might yield better signal-to-noise ratio of estimated GIA and ice-mass change signals.
- The functional model for the patch approach could be adjusted for describing the geometry of two layers: upper layer for surface processes and lower layer for GIA processes (Eq. 3.8). Altimetry could be used for defining patches for the upper layer and the existing GIA solutions for the lower layer. The GIA signal could be constructed using varying depth profile at which viscosities are low enough for viscous deformation to occur (van der Wal et al, 2015).

The entire system to be solved would be instable and thus, challenging to solve. However, at least for EA, where the height difference between the two layers is believed to be large, such an approach that is explicitly based on gravimetry data only, would directly yield mass change estimates for GIA and surface processes without any need for density assumptions.

- According to [Dmitrieva et al \(2015\)](#), the sources of time-dependent noise in GPS time series are not completely understood. The origin of flicker noise is less clear, but time-variable satellite geometry, long-term orbit mismodeling, and multipath have been suggested as possible contributors. It should be investigated whether some of the observed power in the GPS time series at the low frequencies is due to unmodeled stochastic seasonal processes and inter-annual variations. The latter map into the time-varying rate estimates (Ch. 4). The comparison performed in Ch. 5 can help deciding about the origin of the power at the low frequencies. Furthermore, [Davis et al, 2012](#) has shown that noise analyses that do not allow for stochastic seasonal processes run the risk of absorbing some of the seasonal power into the estimates of the non-seasonal noise, thereby significantly overestimating the rate uncertainties. As such, it is clear there is still plenty of space for research on the topic.
- The state vector in Ch. 4 is very long (especially for GPS time series) causing a trade-off between its components. The hyperparameters govern the estimates of the state vector and need to be estimated as well. The lower the dimension of the hyperparameters vector, the faster an optimization algorithm might converge. However, this does not guarantee that the optimal solution will be found if the problem is non-convex. What exactly causes the non-convexity and to which extent (data; definition of the transition matrix; or of the state vector; or of the hyperparameters vector; or most likely the interaction of all aforementioned components) is a challenging topic that needs to be investigated.
- Instead of deriving ice dynamics at the level of drainage systems as in Ch. 5, it could be performed on a grid. For this, the state space framework described in Ch. 4 would need to be extended to account for spatial correlations. This would provide more insights into the similarities/differences between SMB and GRACE, as well as into small-scale processes.
- Combining different altimetry missions, such as ENVISAT, Cryosat, and ICESat-2, will not only allow the combination in Ch. 3 to be performed for an extended time period, but might also provide a better understanding about the geophysical processes if incorporated into the validation/comparison of time-varying trends in Ch. 5.
- Having time series for all data involved into the combination in Ch. 3 would allow GIA and ice mass changes to be estimated on a monthly basis. In this case GIA would need to be constrained to be secular. The patch approach

on a monthly basis together with the time-varying trend analysis on a grid, would increase spatio-temporal resolution of the derived ice mass changes.

- Based on the inter-comparison performed in Ch. 5, secular trends, possibly originating from different sources, manifest themselves as a systematic bias between the GIA-corrected GRACE and elastics-corrected GPS trends. Separating those constant trends is a challenging task that requires further research. For this, the ability of different degree-1 and  $C_{20}$  solutions to minimize this bias could be investigated. A global GIA model could be utilized to mimic non-Antarctic leakage.
- After having identified the different sources with their contribution to the systematic bias between the GIA-corrected GRACE and elastic-corrected GPS trends, the GPS trends could be corrected for elastic deformation and used to redefine the spatial pattern of the derived GIA in Ch. 3.



# REFERENCES

- Anderssen R, Bloomfield P (1975) Properties of the random search in global optimization. *Journal of Optimization Theory and Applications* 16(5-6):383–398
- Argus DE, Peltier W, Drummond R, Moore AW (2014) The Antarctica component of postglacial rebound model ICE-6G\_C (VM5a) based on GPS positioning, exposure age dating of ice thicknesses, and relative sea level histories. *Geophysical Journal International* 198(1):537–563
- Bamber J, Riva R (2010) The sea level fingerprint of recent ice mass fluxes. *The Cryosphere* 4(4):621
- Baur O (2012) On the computation of mass-change trends from GRACE gravity field time-series. *Journal of Geodynamics* 61:120–128
- Baur O, Sneeuw N (2011) Assessing Greenland ice mass loss by means of point-mass modeling: a viable methodology. *Journal of geodesy* 85(9):607–615
- Bettadpur S (2007) CSR Level-2 Processing Standards Document for Product Release 04 GRACE 327-742. Center for Space Research, 3rd edn, URL <http://podaac.jpl.nasa.gov/grace/documentation.html>
- Borsa A, Moholdt G, Fricker H, Brunt K (2013) A range correction for ICESat and its potential impact on ice sheet mass balance studies. *The Cryosphere Discuss* 7:4287–4319
- Boyd S, Vandenberghe L (2004) *Convex optimization*. Cambridge University Press
- Bryson A, Johansen D (1965) Linear filtering for time-varying systems using measurements containing colored noise. *IEEE Transactions on Automatic Control* 10(1):4–10
- Byrd RH, Hribar ME, Jorge N (1999) An interior point algorithm for large-scale nonlinear programming. *SIAM J Optim* 9(4):877–900
- Chambers DP, Bonin JA (2012) Evaluation of Release-05 GRACE time-variable gravity coefficients over the ocean. *Ocean Science Discussions* 9(3):2187–2214, DOI 10.5194/osd-9-2187-2012
- Chen J, Wilson C, Blankenship D, Tapley B (2006) Antarctic mass rates from GRACE. *Geophysical research letters* 33(11)
- Chen J, Wilson C, Li J, Zhang Z (2015) Reducing leakage error in GRACE-observed long-term ice mass change: a case study in West Antarctica. *Journal of Geodesy* 89(9):925–940

- Cheng M, Tapley BD (2004) Variations in the earth's oblateness during the past 28 years. *Journal of Geophysical Research: Solid Earth* 109(B9)
- Cheng M, Ries JC, Tapley BD (2011) Variations of the earth's figure axis from satellite laser ranging and GRACE. *Journal of Geophysical Research: Solid Earth* 116(B1)
- Clarke PJ, Lavallée DA, Blewitt G, Van Dam T, Wahr J (2005) Effect of gravitational consistency and mass conservation on seasonal surface mass loading models. *Geophysical Research Letters* 32(8)
- Colombo OL (1981) Numerical methods for harmonic analysis on the sphere. Tech. rep., OHIO STATE UNIV COLUMBUS DEPT OF GEODETIC SCIENCE AND SURVEYING
- Davis JL, Wernicke BP, Tamisiea ME (2012) On seasonal signals in geodetic time series. *J Geophys Res* 117(B01403)
- Didova O, Gunter B, Riva R, Klees R, Roese-Koerner L (2016) An approach for estimating time-variable rates from geodetic time series. *Journal of Geodesy* pp 1–15
- Dmitrieva K, Segall P, DeMets C (2015) Network-based estimation of time-dependent noise in GPS position time series. *Journal of Geodesy* 89(6):591–606
- Durbin J, Koopman SJ (2012) *Time Series Analysis by State Space Methods*. Oxford University Press
- Ewert H, Popov SV, Richter A, Schwabe J, Scheinert M, Dietrich R (2012) Precise analysis of ICESat altimetry data and assessment of the hydrostatic equilibrium for subglacial Lake Vostok, East Antarctica. *Geophysical Journal International* 191(2):557–568, DOI 10.1111/j.1365-246X.2012.05649.x
- Farahani H (2013) Modelling the Earth's static and time-varying gravity field using a combination of GRACE and GOCE data. PhD thesis, TU Delft, Delft University of Technology
- Farahani HH, Ditmar P, Inácio P, Didova O, Gunter B, Klees R, Guo X, Guo J, Sun Y, Liu X, et al (2016) A high resolution model of linear trend in mass variations from DMT-2: added value of accounting for coloured noise in GRACE data. *Journal of Geodynamics*
- Farhang-Boroujeny B (1998) *Adaptive filters: Theory and applications*.
- Farrell W, Clark JT (1976) On postglacial sea level. *Geophys J R Astron Soc* 46:647–667
- Felikson D, Urban T, Gunter BC, Pie N, Pritchard HD, Harpold R, Schutz BE (2017) Comparison of elevation change detection methods from ICESat altimetry over the Greenland Ice Sheet. *IEEE Trans on Geoscience and Remote Sensing*

- Ferguson AC, Davis CH, Cavanaugh JE (2004) An autoregressive model for analysis of ice sheet elevation change time series. *IEEE transactions on geoscience and remote sensing* 42(11):2426–2436
- Flechtner F (2007) GRACE 327-750: AOD1B product description document for product release 01 to 04. Tech. rep., GeoForschungsZentrum Potsdam, Germany
- Forsberg R, Sørensen L, Simonsen S (2017) Greenland and Antarctica Ice Sheet Mass Changes and Effects on Global Sea Level. *Surveys in Geophysics* pp 1–16
- Gazeaux J, Williams S, King M, Bos M, Dach R, Deo M, Moore AW, Ostini L, Petrie E, Roggero M, et al (2013) Detecting offsets in GPS time series: First results from the detection of offsets in GPS experiment. *Journal of Geophysical Research: Solid Earth* 118(5):2397–2407
- González Á (2010) Measurement of areas on a sphere using fibonacci and latitude–longitude lattices. *Mathematical Geosciences* 42(1):49–64
- Greene WH (1993) *Econometric analysis*, 2nd edn. New York: Prentice-Hall
- Groh A, Ewert H, Scheinert M, Fritsche M, Rülke A, Richter A, Rosenau R, Dietrich R (2012) An investigation of Glacial Isostatic Adjustment over the Amundsen Sea sector, West Antarctica. *Global and Planetary Change* 98-99(0):45 – 53, DOI 10.1016/j.gloplacha.2012.08.001
- Groh A, Ewert H, Rosenau R, Fagiolini E, Gruber C, Floricioiu D, Jaber WA, Linow S, Flechtner F, Eineder M, et al (2014) Mass, volume and velocity of the Antarctic ice sheet: present-day changes and error effects. *Surveys in Geophysics* 35(6):1481–1505
- Gunter B, Urban T, Riva R, Helsen M, Harpold R, Poole S, Nagel P, Schutz B, Tapley B (2009) A comparison of coincident GRACE and ICESat data over Antarctica. *Journal of Geodesy* 83:1051–1060, DOI 10.1007/s00190-009-0323-4
- Gunter B, Riva R, Urban T, Harpold R, Schutz B, Nagel P, Helsen M (2010) Evaluation of GRACE and ICESat Mass Change Estimates over Antarctica. In: Mertikas SP (ed) *Gravity, Geoid and Earth Observation*, International Association of Geodesy Symposia, vol 135, Springer Berlin Heidelberg, pp 563–569, DOI 10.1007/978-3-642-10634-7\_75
- Gunter B, Didova O, Riva R, Ligtenberg S, Lenaerts J, King M, Van den Broeke M, Urban T (2014) Empirical estimation of present-day antarctic glacial isostatic adjustment and ice mass change. *The Cryosphere* 8(2):743–760
- Harvey AC (1989) *Forecasting, structural time series models and the Kalman filter*. Cambridge: Cambridge University Press
- Helsen MM, Van Den Broeke MR, Van De Wal RS, Van De Berg WJ, Van Meijgaard E, Davis CH, Li Y, Goodwin I (2008) Elevation changes in Antarctica mainly determined by accumulation variability. *Science* 320(5883):1626–1629

- Horst R, Pardalos PM, Thoai NV (2000) Introduction to global optimization, non-convex optimization and its applications, vol. 48
- Horwath M, Legrésy B, Rémy F, Blarel F, Lemoine JM (2012) Consistent patterns of Antarctic ice sheet interannual variations from ENVISAT radar altimetry and GRACE satellite gravimetry. *Geophysical Journal International* 189(2):863–876
- Hosking JR (1981) Fractional differencing. *Biometrika* 68(1):165–176
- Hughes GB, Chraïbi M (2011) Calculating Ellipse Overlap Areas. URL <http://arxiv.org/abs/1106.3787>
- Ivins ER, James TS (2005) Antarctic glacial isostatic adjustment: a new assessment. *Antarctic Science* 17(4):541–553
- Ivins ER, James TS, Wahr J, Schrama EJO, Landerer FW, Simon KM (2013) Antarctic contribution to sea level rise observed by GRACE with improved GIA correction. *J Geophys Res* 118:1–16
- Jacob T, Wahr J, Pfeffer W, Swenson S (2012) Recent contributions of glaciers and ice caps to sea level rise. *Nature* 482(7386):514–518
- Kaspers KA, van de Wal R, van den Broeke MR, Schwander J, van Lipzig NPM, Brenninkmeijer CAM (2004) Model calculations of the age of firn air across the Antarctic continent. *Atmos Chem Phys* 4
- King MA, Bingham RJ, Moore P, Whitehouse PL, Bentley MJ, Milne GA (2012) Lower satellite-gravimetry estimates of Antarctic sea-level contribution. *Nature* 491(7425):586–589, DOI 10.1038/nature11621
- Klees R, Ditmar P, Broersen P (2003) How to handle colored observation noise in large least-squares problems. *Journal of Geodesy* 76:629–640
- Klees R, Revtova EA, Gunter BC, Ditmar P, Oudman E, Winsemius HC, Savenije HHG (2008) The design of an optimal filter for monthly GRACE gravity models. *Geophysical Journal International* 175(2):417–432, DOI 10.1111/j.1365-246X.2008.03922.x
- Klemann V, Martinec Z (2011) Contribution of glacial-isostatic adjustment to the geocenter motion. *Tectonophysics* 511(3):99–108
- Kusche J (2007) Approximate decorrelation and non-isotropic smoothing of time-variable GRACE-type gravity field models. *Journal of Geodesy* 81:733–749, DOI 10.1007/s00190-007-0143-3
- Kusche J, Schrama EJO (2005) Surface mass redistribution inversion from global GPS deformation and Gravity Recovery and Climate Experiment (GRACE) gravity data. *J Geophys Res* 110(B09409)
- Langbein J (2004) Noise in two-color electronic distance meter measurements revisited. *Journal of Geophysical Research: Solid Earth* (1978–2012) 109(B4)

- Lemke P, Ren J, Alley R, Allison I, Carrasco J, Flato G, Fujii Y, Kaser G, Mote P, Thomas R, et al (2007) Observations: changes in snow, ice and frozen ground. *Climate Change 2007: The Physical Science Basis Contribution of Working Group I to the Fourth Assessment Report of the Intergovernmental Panel on Climate Change*
- Lenaerts J, Meijgaard E, Broeke MR, Ligtenberg SR, Horwath M, Isaksson E (2013) Recent snowfall anomalies in Dronning Maud Land, East Antarctica, in a historical and future climate perspective. *Geophysical Research Letters* 40(11):2684–2688
- Lenaerts JTM, van den Broeke MR, van de Berg WJ, van Meijgaard E, Kuipers Munneke P (2012) A new, high-resolution surface mass balance map of Antarctica (1979–2010) based on regional atmospheric climate modeling. *Geophysical Research Letters* 39(4):n/a–n/a, DOI 10.1029/2011GL050713
- Liebling TM, Pournin L (2012) Voronoi diagrams and delaunay triangulations: Ubiquitous siamese twins. *Documenta Mathematica*, ISMP pp 419–431
- Ligtenberg S, Horwath M, den Broeke M, Legréy B (2012) Quantifying the seasonal “breathing” of the Antarctic ice sheet. *Geophysical Research Letters* 39(23)
- Ligtenberg SRM, Helsen MM, van den Broeke MR (2011) An improved semi-empirical model for the densification of Antarctic firn. *The Cryosphere* 5(4):809–819, DOI 10.5194/tc-5-809-2011
- Liu X, Ditmar P, Siemes C, Slobbe D, Revtova E, Klees R, Riva R, Zhao Q (2010) DEOS Mass Transport model (DMT-1) based on GRACE satellite data: methodology, validation, and application to estimating the ice mass balance of Greenland. *Geophysical Journal International* 181(2):769–788
- Luthcke SB, Sabaka T, Loomis B, Arendt A, McCarthy J, Camp J (2013) Antarctica, Greenland and Gulf of Alaska land-ice evolution from an iterated GRACE global mascon solution. *Journal of Glaciology* 59(216):613–631
- Martín-Español A, King MA, Zammit-Mangion A, Andrews SB, Moore P, Bamber JL (2016a) An assessment of forward and inverse GIA solutions for Antarctica. *Journal of Geophysical Research: Solid Earth* 121(9):6947–6965
- Martín-Español A, Zammit-Mangion A, Clarke PJ, Flament T, Helm V, King MA, Luthcke SB, Petrie E, Rémy F, Schön N, et al (2016b) Spatial and temporal Antarctic Ice Sheet mass trends, glacio-isostatic adjustment, and surface processes from a joint inversion of satellite altimeter, gravity, and GPS data. *Journal of Geophysical Research: Earth Surface*
- Martín-Español A, Bamber JL, Zammit-Mangion A (2017) Constraining the mass balance of East Antarctica. *Geophysical Research Letters*
- Mayer-Gürr T, Zehentner N, Klinger B, Kvas A (2014) ITSGRACE2014: A new GRACE gravity field release computed in Graz, GRACE Sci. Team Meet, Potsdam

- Nield GA, Whitehouse PL, King MA, Clarke PJ, Bentley MJ (2012) Increased ice loading in the Antarctic Peninsula since the 1850s and its effect on glacial isostatic adjustment. *Geophysical Research Letters* 39(17)
- Nield GA, Barletta VR, Bordoni A, King MA, Whitehouse PL, Clarke PJ, Domack E, Scambos TA, Berthier E (2014) Rapid bedrock uplift in the Antarctic Peninsula explained by viscoelastic response to recent ice unloading. *Earth and Planetary Science Letters* 397:32–41
- Nield GA, Whitehouse PL, King MA, Clarke PJ (2016) Glacial isostatic adjustment in response to changing Late Holocene behaviour of ice streams on the Siple Coast, West Antarctica. *Geophysical Journal International* 205(1):1–21
- Nocedal J, Wright S (2006) *Numerical Optimization*, series in operations research and financial engineering. Springer, New York, USA
- Pearson R (2011) *Exploring Data in Engineering, the Sciences, and Medicine*. Oxford University Press
- Peltier W (2004) Global glacial isostasy and the surface of the ice-age Earth: The ICE-5G (VM2) model and GRACE. *Annual Review of Earth and Planetary Science* 32:111–149
- Peltier W, Argus D, Drummond R (2015) Space geodesy constrains ice age terminal deglaciation: The global ICE-6G\_C (VM5a) model. *Journal of Geophysical Research: Solid Earth* 120(1):450–487
- Peng JY, Aston JA (2011) The state space models toolbox for MATLAB. *Journal of Statistical Software* 41(6):1–26
- Plaszczynski S (2007) Generating long streams of  $1/\alpha$  noise. *Fluctuation and Noise Letters* 7(01):R1–R13
- Pritchard HD, Arthern RJ, Vaughan DG, Edwards LA (2009) Extensive dynamic thinning on the margins of the Greenland and Antarctic ice sheets. *Nature* 461(7266):971–975
- Ran J (2017) *Analysis of mass variations in Greenland by a novel variant of the mascon approach*. PhD thesis, Delft University of Technology
- Ray J (1999) *IERS Analysis Campaign to Investigate Motions of the Geocenter. With a special session at the Fall 1997 AGU Meeting, San Francisco, CA (USA)*. IERS Technical Note 25
- Rignot E, Bamber J, van den Broeke M, Davis C, Li Y, van de Berg W, van Meijgaard E (2008) Recent Antarctic ice mass loss from radar interferometry and regional climate modelling. *Nature Geosciences* 1:106–110, DOI doi:10.1038/ngeo102

- Riva REM, Gunter BC, Urban TJ, Vermeersen BLA, Lindenberg RC, Helsen MM, Bamber JL, van den Broeke MR, Schutz BE (2009) Glacial Isostatic Adjustment over Antarctica from combined ICESat and GRACE satellite data. *Earth and Planetary Science Letters* 288:516–523, DOI 10.1016/j.epsl.2009.10.013
- Roese-Koerner L, Devaraju B, Sneeuw N, Schuh WD (2012) A stochastic framework for inequality constrained estimation. *Journal of Geodesy* 86(11):1005–1018
- Sasgen I, Dobslaw H, Martinec Z, Thomas M (2010) Satellite gravimetry observation of Antarctic snow accumulation related to ENSO. *Earth and Planetary Science Letters* 299(3):352–358
- Sasgen I, Konrad H, Ivins ER, van den Broeke MR, Bamber JL, Martinec Z, Klemann V (2013) Antarctic ice-mass balance 2003 to 2012: regional reanalysis of GRACE satellite gravimetry measurements with improved estimate of glacial-isostatic adjustment based on GPS uplift rates. *The Cryosphere* 7(1499–1512)
- Save H, Bettadpur S, Tapley B (2012) Reducing errors in the GRACE gravity solutions using regularization. *Journal of Geodesy* 86:695–711, DOI 10.1007/s00190-012-0548-5
- Scambos TA, Bohlander JA, Shuman CA, Skvarca P (2004) Glacier acceleration and thinning after ice shelf collapse in the Larsen B embayment, Antarctica. *Geophysical Research Letters* 31(18):n/a–n/a, DOI 10.1029/2004GL020670
- Schoen N, Zammit-Mangion A, Rougier J, Flament T, Rémy F, Luthcke S, Bamber J (2015) Simultaneous solution for mass trends on the West Antarctic Ice Sheet. *The Cryosphere* 9(2):805–819
- Seo KW, Wilson CR, Chen J, Waliser DE (2008) Grace's spatial aliasing error. *Geophysical Journal International* 172(1):41–48, DOI 10.1111/j.1365-246X.2007.03611.x
- Shepherd A, Ivins ER, Geruo A, Barletta VR, Bentley MJ, Bettadpur S, Briggs KH, Bromwich DH, Forsberg R, Galin N, et al (2012) A reconciled estimate of ice-sheet mass balance. *Science* 338(6111):1183–1189
- Siegfried M, Hawley R, Burkhart J (2011) High-Resolution Ground-Based GPS Measurements Show Intercampaign Bias in ICESat Elevation Data Near Summit, Greenland. *Geoscience and Remote Sensing, IEEE Transactions on* 49(9):3393–3400, DOI 10.1109/TGRS.2011.2127483
- Siemes C, Ditmar P, Riva R, Slobbe D, Liu X, Farahani H (2013) Estimation of mass change trends in the Earth's system on the basis of GRACE satellite data, with application to Greenland. *Journal of Geodesy* 87:69–87, DOI 10.1007/s00190-012-0580-5
- Simon K, James T, Ivins E (2010) Ocean loading effects on the prediction of Antarctic glacial isostatic uplift and gravity rates. *Journal of Geodesy* 84(5):305–317, DOI 10.1007/s00190-010-0368-4

- Slobbe D, Lindenberg R, Ditmar P (2008) Estimation of volume change rates of Greenland's ice sheet from ICESat data using overlapping footprints. *Remote Sensing of Environment* 112(12):4204 – 4213, DOI 10.1016/j.rse.2008.07.004
- Sneeuw N (1994) Global spherical harmonic analysis by least-squares and numerical quadrature methods in historical perspective. *Geophysical Journal International* 118(3):707–716
- Strang G, Borre K (1997) *Linear algebra, geodesy, and GPS*. Siam
- Sun Y, Riva R, Ditmar P (2016) Optimizing estimates of annual variations and trends in geocenter motion and J2 from a combination of GRACE data and geophysical models. *Journal of Geophysical Research: Solid Earth*
- Sutterley TC, Velicogna I, Rignot E, Mougintot J, Flament T, Van Den Broeke MR, Van Wessem JM, Reijmer CH (2014) Mass loss of the Amundsen Sea Embayment of West Antarctica from four independent techniques. *Geophysical Research Letters* 41(23):8421–8428
- Swenson S, Wahr J (2006) Post-processing removal of correlated errors in GRACE data. *Geophysical Research Letters* 33(8)
- Swenson S, Chambers D, Wahr J (2008) Estimating geocenter variations from a combination of GRACE and ocean model output. *Journal of Geophysical Research: Solid Earth* 113(B8)
- Teixeira Encarnação J (2015) Next-generation satellite gravimetry for measuring mass transport in the Earth system. PhD thesis, TU Delft, Delft University of Technology
- Tesmer V, Steigenberger P, van Dam T, Mayer-Gürr T (2011) Vertical deformations from homogeneously processed GRACE and global GPS long-term series. *Joge* 85:291–310
- Thomas ID, King MA, Bentley MJ, Whitehouse PL, Penna NT, Williams SDP, Riva REM, Lavalée DA, Clarke PJ, King EC, Hindmarsh RCA, Koivula H (2011) Widespread low rates of Antarctic glacial isostatic adjustment revealed by GPS observations. *Geophysical Research Letters* 38(22), DOI 10.1029/2011GL049277
- Urban T, Schutz BE (2005) ICESat sea level comparisons. *Geophysical research letters* 32(L23S10), DOI doi:10.1029/10.1029/2005GL024306
- Van Wessem J, Reijmer C, Morlighem M, Mougintot J, Rignot E, Medley B, Joughin I, Wouters B, Depoorter M, Bamber J, et al (2014) Improved representation of East Antarctic surface mass balance in a regional atmospheric climate model. *Journal of Glaciology* 60(222):761–770
- Velicogna I, Wahr J (2002) A method for separating Antarctic postglacial rebound and ice mass balance using future ICESat Geoscience Laser Altimeter System, Gravity Recovery and Climate Experiment, and GPS satellite data. *Journal of*

- Geophysical Research: Solid Earth 107(B10):ETG 20–1–ETG 20–11, DOI 10.1029/2001JB000708
- Velicogna I, Wahr J (2006) Measurements of time-variable gravity show mass loss in Antarctica. *Science* 311(1754), doi:10.1126/science.1123785
- Velicogna I, Sutterley T, van den Broeke M (2014) Regional acceleration in ice mass loss from Greenland and Antarctica using GRACE time-variable gravity data. *Geophysical Research Letters* 41(22):8130–8137
- Wahr J, Molenaar M, Bryan F (1998) Time variability of the Earth's gravity field: Hydrological and oceanic effects and their possible detection using GRACE. *Journal of Geophysical Research: Solid Earth* 103(B12):30,205–30,229
- Wahr J, Wingham D, Bentley C (2000) A method of combining icesat and grace satellite data to constrain antarctic mass balance. *Journal of Geophysical Research: Solid Earth* 105(B7):16,279–16,294
- van der Wal W, Whitehouse PL, Schrama E (2015) Effect of GIA models with 3D composite mantle viscosity on GRACE mass balance estimates for Antarctica. *Earth and Planetary Science Letters*
- Watkins MM, Wiese DN, Yuan DN, Boening C, Landerer FW (2015) Improved methods for observing Earth's time variable mass distribution with GRACE using spherical cap mascons. *Journal of Geophysical Research: Solid Earth* 120(4):2648–2671
- Whitehouse PL, Bentley MJ, Milne GA, King MA, Thomas ID (2012) A new glacial isostatic adjustment model for Antarctica: calibrated and tested using observations of relative sea-level change and present-day uplift rates. *Geophysical Journal International* 190(3):1464–1482, DOI 10.1111/j.1365-246X.2012.05557.x
- Wilks SS (1938) The large-sample distribution of the likelihood ratio for testing composite hypotheses. *The Annals of Mathematical Statistics* 9:60–62
- Williams S (2003a) The effect of coloured noise on the uncertainties of rates estimated from geodetic time series. *Journal of Geodesy* 76(9–10):483–494
- Williams SD (2003b) Offsets in global positioning system time series. *Journal of Geophysical Research: Solid Earth* (1978–2012) 108(B6)
- Williams SD (2008) CATS: GPS coordinate time series analysis software. *GPS solutions* 12(2):147–153
- Williams SD, Bock Y, Fang P, Jamason P, Nikolaidis RM, Prawirodirdjo L, Miller M, Johnson DJ (2004) Error analysis of continuous GPS position time series. *Journal of Geophysical Research: Solid Earth* (1978–2012) 109(B3)
- Williams SD, Moore P, King MA, Whitehouse PL (2014) Revisiting GRACE Antarctic ice mass trends and accelerations considering autocorrelation. *Earth and Planetary Science Letters* 385:12–21

- Wolstencroft M, King MA, Whitehouse PL, Bentley MJ, Nield GA, King EC, McMillan M, Shepherd A, Barletta V, Bordoni A, et al (2015) Uplift rates from a new high-density GPS network in Palmer Land indicate significant late Holocene ice loss in the southwestern Weddell Sea. *Geophysical Journal International* 203(1):737–754
- Wong L, Buechler G, Downs W, Sjogren W, Muller P, Gottlieb P (1971) A surface-layer representation of the lunar gravitational field. *Journal of Geophysical Research* 76(26):6220–6236
- Wouters B, Bamber J, Van den Broeke M, Lenaerts J, Sasgen I (2013) Limits in detecting acceleration of ice sheet mass loss due to climate variability. *Nature Geoscience* 6(8):613–616
- Zammit-Mangion A, Bamber JL, Schoen NW, Rougier JC (2015) A data-driven approach for assessing ice-sheet mass balance in space and time. *Annals of Glaciology* 56(70):175–183
- Zwally H, Schutz R, Bentley C, Bufton J, Herring T, Minster J, Spinhirne J, Thomas R (2011) GLAS/ICESat l2 global land surface altimetry data. Version 33:27
- Zwally HJ, Li J, Robbins JW, Saba JL, Yi D, Brenner AC (2015) Mass gains of the Antarctic ice sheet exceed losses. *Journal of Glaciology* 61(230):1019–1036
- Zwally JH, Giovinetto MB, Beckley MA, Saba JL (2012) Antarctic and Greenland Drainage Systems. GSFC Cryospheric Sciences Laboratory, URL [http://icesat4.gsfc.nasa.gov/cryo\\_data/ant\\_grn\\_drainage\\_systems.php](http://icesat4.gsfc.nasa.gov/cryo_data/ant_grn_drainage_systems.php)

# A

## TREATMENT OF COLOURED NOISE IN GPS TIME SERIES

### A.1. INTRODUCTION

The coloured noise in the GPS time series was co-estimated along with signal constituents, such as trend and harmonic terms, within the Kalman filter (KF) framework that was used to solve the defined state space model. The state space model was defined in the way that all components in the state vector were allowed to vary in time (except the intercept). The coloured noise was modeled using a general autoregressive moving average (ARMA) process. This supplement is meant to explain the practical implementation of the ARMA model. It is presented here as one potential method to treat coloured noise in a time series. Other methods may be possible; however, the goal was to show that if geodetic time series contain coloured noise, it can be handled within the suggested approach and GPS data were used as a perfect example for such a data type.

Note that, when not modeling the coloured noise we found that the solutions for the noise parameters were outside a reasonable range (e.g., zero noise variance or noise variance exceeding a reasonable limit). This emphasizes the need to model coloured noise in GPS time series.

An alternate approach for modeling noise in GPS time series can be found in the literature, and makes use of a power law model (Langbein (2004), Williams (2008), Dmitrieva et al (2015)). Power law noise  $\frac{1}{f^\alpha}$  is a stochastic process with a spectral density having a power exponent  $0 < \alpha \leq 2$  (Plaszczynski, 2007). For GPS time series analysis, flicker or random walk noise are usually used, which corresponds to  $\alpha = 1$  and  $\alpha = 2$ , respectively. Which of these two noise models is preferred is still a topic of active research. In the recent study of Dmitrieva et al (2015) for instance a non-negligible random walk was found contrary to some previous studies such as Williams et al (2004).

Random walk noise (so-called Brownian motion process) with  $\alpha = 2$  is an ana-

logue of the Gaussian random walk we employed to model time-varying signal constituents. Random walk is usually used within the state space model formalism when the observations are not equally spaced. In this case all variances will be scaled by a time step  $dt$ . If the observations are close together it is advisable to set up an autocorrelated model for the observational noise; the coefficients (or parameters) of this have to be put into the state space vector and the resulting noise model would not be a time-dependent one (Durbin and Koopman, 2012, chap. 3.8.1). That means that the observational noise  $\epsilon_t$  is parameterized in the way that the process noise matrix consists of a time-independent noise (input required by KF), but the output (state vector forming  $\epsilon_t$ ) is time-dependent. That is the main idea behind the 50-year old "shaping filter" which was designed by Bryson and Johansen (1965) exactly for purposes of modeling temporally correlated noise and which is still used for analyzing GPS time series (e.g., Dmitrieva et al (2015)).

Flicker noise with  $\alpha = 1$  is difficult to represent in a state space model. That is why for instance Dmitrieva et al (2015) approximated flicker noise by a linear combination of independent first-order Gauss-Markov processes. In general, flicker and random walk noise are low-frequency noise models - they describe a long-range dependency (have a long memory). ARMA models are known to describe a short-range dependency (have a short memory). The question is whether it is possible to represent a long-range dependency using a short-range one. Before we answer this question, we must 1) provide a mathematical description of an ARMA process; 2) describe how we synthetically generate low-frequency noise, which is necessary to answer the above posed question, and, 3) explain in detail the procedure of parameterizing coloured noise.

## A.2. ARMA MODEL

An ARMA model of order  $(p, q)$  is defined as

$$\epsilon_t = \sum_{j=1}^l \phi_j \epsilon_{t-j} + \kappa_t + \sum_{j=1}^{l-1} \theta_j \kappa_{t-j}, \quad t = 1, \dots, n, \quad (\text{A.1})$$

where  $\phi_1, \dots, \phi_p$  are the autoregressive parameters,  $\theta_1, \dots, \theta_q$  are the moving average parameters and  $\kappa_t$  is a serially independent series of  $N(0, \sigma_\kappa^2)$  disturbances and  $l = \max(p, q + 1)$ . Some parameters of an ARMA model can be zero, which yields two special cases: if  $q = 0$ , the process is autoregressive (AR) of order  $p$ ; if  $p = 0$ , the process is a moving-average (MA) process of order  $q$ . Generally, an ARMA model subsumes AR and MA models.

## A.3. GENERATING $\frac{1}{f^\alpha}$

To generate flicker and random walk noise we first generate the coefficients of the so-called fractional differencing according to Hosking (1981) and multiply them with the white noise in the frequency domain. Performing inverse Fourier transform provides us with the time series of flicker noise for  $\alpha = 1$  and random walk noise for  $\alpha = 2$ . The white noise is generated using a Gaussian distribution with

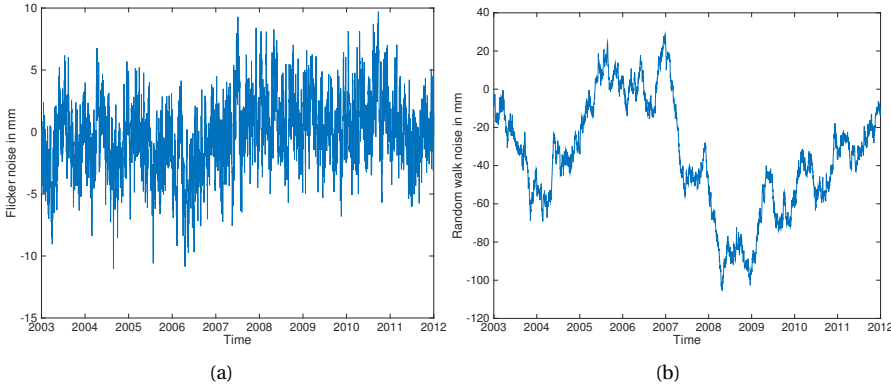


Figure A.1: Synthetically generated time series of the (a) flicker noise ( $\alpha = 1$ ) and (b) random walk noise ( $\alpha = 2$ );  $\sigma_{wt} = 2$  mm in both cases.

$N(0, \sigma_{wt}^2)$ , where the standard deviation of the white noise  $\sigma_{wt}$  was set equal to 2 mm. Synthetically generated time series of the flicker and random walk noise are shown in the Fig. A.1.

#### A.4. DETECTING AN APPROPRIATE ORDER FOR ARMA( $p, q$ )

We model synthetically generated noise time series shown in Fig. A.1 using an ARMA( $p, q$ ) process. Before we put the coefficients  $\phi_1, \dots, \phi_p$  and  $\theta_1, \dots, \theta_q$  into the state space vector, we first need to get an idea about how the order  $p$  and  $q$  should be chosen. For this, we compute the power spectral density (PSD) of the generated noise, which is shown in black in Fig. A.2. Using this PSD function we estimate the pure recursive part of the filter (MA) and non-recursive part of the filter (AR) by applying the standard Levinson-Durbin algorithm (Farhang-Boroujeny, 1998). The parameters (or coefficients) of the MA and AR models are computed using a defined  $p$  and  $q$ , which are then used to compute the PSD function of the combined ARMA( $p, q$ ) solution. To control the dimension of the state vector  $\alpha_t$  we limit the maximum order of the ARMA process to 5, which means we compute PSD for ARMA( $p, q$ ) generated for  $p, q \in \{0, \dots, 5\}$  (including two special cases AR( $p$ ) and MA( $q$ )). We then use GIC (Generalized Information Criterion) order selection criterion to select the PSD of the ARMA model that best fits the PSD of the generated noise. The  $(p, q)$  of this ARMA model define the amount of  $\phi$  and  $\theta$  coefficients used to parameterize coloured noise  $\varepsilon_t$

$$\alpha_t^{[e]} = \begin{bmatrix} \varepsilon_t \\ \phi_2 \varepsilon_{t-1} + \dots + \phi_1 \varepsilon_{t-l+1} + \theta_1 \kappa_t + \dots + \theta_{l-1} \kappa_{t-l+2} \\ \phi_3 \varepsilon_{t-1} + \dots + \phi_1 \varepsilon_{t-l+2} + \theta_2 \kappa_t + \dots + \theta_{l-1} \kappa_{t-l+3} \\ \vdots \\ \phi_l \varepsilon_{t-1} + \theta_{l-1} \kappa_t \end{bmatrix}. \quad (\text{A.2})$$

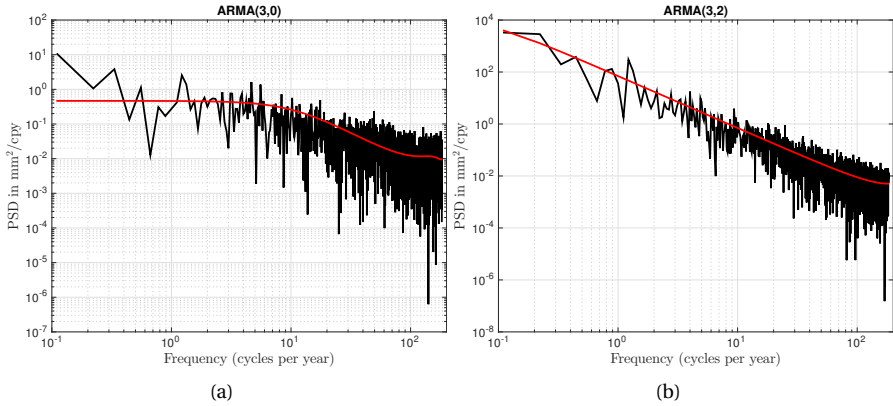


Figure A.2: The PSD (power spectral density) function of the ARMA model (red) that best fits the PSD of synthetically generated time series (black) of the (a) flicker noise and (b) random walk noise.

## A.5. RANDOM WALK NOISE AND ARMA( $p, q$ )

Plaszczynski (2007) has shown that ARMA models can be used to generate  $\frac{1}{f^\alpha}$  noise for  $\alpha = 2$ . The link between ARMA and  $\frac{1}{f^\alpha}$  can be immediately seen from the mathematical description of the random walk process

$$\varepsilon_t = \varepsilon_{t-1} + \kappa_t, \quad (\text{A.3})$$

where  $\varepsilon_t$  denotes the value of the observation at time  $t$ . If  $q = 0$ ,  $p = 1$  and  $\phi_1 = 1$ , Eq. (A.1) is equivalent to Eq. (A.3). That means that we can easily represent random walk using AR(1). To maintain this statement for an ARMA process, we synthetically generated random walk noise and applied the same procedure as to the real GPS data to determine how the noise might be parameterized (how many  $p$  and  $q$  should be estimated). As can be seen from Fig. A.2, random walk noise will be modelled by ARMA(3,2) for the synthetically generated noise time series shown in Fig. A.1b. Using the Kalman filter framework described in the main paper, likelihood function is maximized (MLE) to estimate the hyperparameters. Note that to keep the computational time for the experiments conducted in the supplement low, the simplest and fastest optimization routine for MLE was used (not the one described in the main paper and used for the real data). Zero was used as a single initial guess for all hyperparameters. The hyperparameters are estimated to be:  $\phi_1 = 0.02$ ,  $\phi_2 = 0.44$ ,  $\phi_3 = 0.54$ ,  $\theta_1 = 0.99$ ,  $\theta_2 = 0.54$  and  $\sigma_\kappa = 1.94$  mm instead of the 2 mm originally used to generate the noise model. When we use AR(1) instead of ARMA(3,2),  $\phi_1 = 0.997$  and  $\sigma_\kappa = 1.94$ . Theoretically, we could also use AR(3,0) that yields the hyperparameters:  $\phi_1 = 1$ ,  $\phi_2 = -0.03$ ,  $\phi_3 = 0.03$  and  $\sigma_\kappa = 1.94$  mm. We conducted this experiment for 100 trials. For this, 100 realizations of the white noise with  $\sigma_{w_t} = 2$  mm were used to generate random walk noise; ARMA( $p, q$ ) were then determined based on the PSD approach described above. Based on the determined ( $p, q$ ) the generated noise was parameterized within the state space

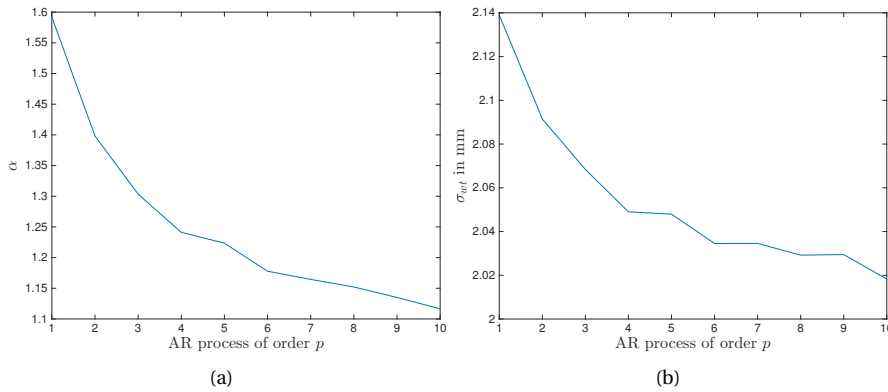


Figure A.3: Approximating synthetically generated time series of the flicker noise ( $\alpha = 1, \sigma_{wt} = 2$  mm) using AR( $p$ ) process. The results are based on 100 realizations of the white noise that is used to generate the flicker noise.

model. The corresponding hyperparameters were estimated by maximizing the likelihood that was computed from KF output. In this way, we get 100 estimates for  $\sigma_{wt}$  which when averaged should ideally be equal 2 mm. The average  $\sigma_{wt} = 2.003$  mm, illustrating that ARMA can effectively model the input noise. The preferred ARMA model for these 100 trials was AR(1,0).

## A.6. FLICKER NOISE AND ARMA( $p, q$ )

ARMA models can be used to approximate flicker noise. After generating flicker noise time series (Fig. A.1a), our PSD approach suggested using an AR(3) model to approximate it. Using the Kalman filter framework, the likelihood function is maximized to estimate the hyperparameters. For the generated flicker noise, the hyperparameters are estimated as:  $\phi_1 = 0.57, \phi_2 = 0.13, \phi_3 = 0.10$  and  $\sigma_{\kappa} = 2.01$  mm instead of the 2 mm originally used to generate the noise model.

To show that ARMA models can sufficiently approximate flicker noise, we use a special ARMA case - AR( $p$ ). Using 100 realizations of the white noise ( $\sigma_{wt} = 2$  mm) to generate flicker noise, we approximate  $\frac{1}{f}$  with an autoregressive model of ten different orders  $p = 1 \dots 10$ . The results are summarized in Fig. A.3. This Figure shows estimated  $\alpha$  and  $\sigma_{wt}$  (average over 100 trials) depending on the order  $p$ . The results yield two conclusions. First, one would need an infinite number of parameters  $p$  to exactly describe flicker noise, since even if  $p = 10$ ,  $\alpha = 1.12$  instead of being 1 and  $\sigma_{wt} = 2.02$  instead of being 2 mm. Second, for real cases we limit the maximum order  $p$  to 5 in order to control the dimension of the state vector  $\alpha_t^{[e]}$ , since only a negligible improvement of the estimated  $\alpha$  and  $\sigma_{wt}$  can be observed for  $p > 5$ . For  $p = 5$ , the average  $\alpha = 1.22$  and  $\sigma_{wt} = 2.05$ .

## A.7. DISCUSSION

We use a general ARMA( $p, q$ ) model that subsumes two special cases (AR and MA) to handle coloured noise in GPS time series while simultaneously estimating trend and harmonic terms that are allowed to vary in time. ARMA models can accurately represent random walk noise and additionally, they can handle short-range dependency, which is their recognized merit. Because our goal is not separating coloured noise into possible constituents, but co-estimating it, we used ARMA models up to order 5 that can be easily represented in the state space formalism for equally spaced data. This was also shown to reasonably approximate flicker noise, although alternative methods for approximating flicker noise in a state space model can be found in the literature ([Dmitrieva et al, 2015](#)).

# CURRICULUM VITÆ

## Olga Andriiwna Didova

21-11-1984 Born in Dnipropetrovsk, Ukraine.

### EDUCATION

- 1991–2000 Comprehensive High School, Dnipropetrovsk, Ukraine
- 2000–2002 Realschule, Gangelt, Germany
- 2002–2005 Bischöfliches Gymnasium St. Ursula, Geilenkirchen, Germany
- 2005–2009 B. Sc. in Geodesy and Geoinformation, University of Bonn, Germany  
*Thesis:* Relative motion of the satellites of the GNSS based on local horizon systems  
*Promotor:* Prof. Dr-Ing. KH. Ilk
- 2009–2011 M. Sc. in Geodesy and Geoinformation, University of Bonn, Germany  
*Thesis:* Analysis of atmospheric data products for the reduction of satellite gravity measurements  
*Promotor:* Prof. Dr-Ing. J. Kusche
- 2012–2017 PhD candidate in Department Geoscience and Remote Sensing, Delft University of Technology, The Netherlands  
*Thesis:* Separating GIA and ice-mass change signals in Antarctica using satellite data  
*Promotor:* Prof. Dr-Ing. R. Klees

### AWARDS

- 2015 General Fall Meeting Student Travel Grant, American Geophysical Union (AGU)
- 2017 Young Authors Award 2016, International Association of Geodesy (IAG)



# LIST OF PUBLICATIONS

1. B. C. Gunter, **O. Didova**, R. E. M. Riva, S. R. M. Ligtenberg, J. T. M. Lenaerts, M. A. King, M. R. van den Broeke, and T. Urban (2014). Empirical estimation of present-day antarctic glacial isostatic adjustment and ice mass change. *The Cryosphere*, 8(2):743-760.
2. M. Wolstencroft, M. A. King, P. L. Whitehouse, M. J. Bentley, G. A. Nield, E. C. King, M. McMillan, A. Shepherd, V. Barletta, A. Bordon, R. E. M. Riva, **O. Didova**, and B. C. Gunter (2015). Uplift rates from a new high-density GPS network in Palmer Land indicate significant late Holocene ice loss in the southwestern Weddell Sea. *Geophysical Journal International*. 203, 1, p. 737-754 18 p.
3. **O. Didova**, B. C. Gunter, R. E. M. Riva, R. Klees, and L. Roese-Koerner (2016). An approach for estimating time-variable rates from geodetic time series. *Journal of Geodesy* pp 1-15
4. H. Farahani, P. Ditmar, P. Inacio, **O. Didova**, B. C. Gunter, R. Klees, X. Guo, J. Guo, Y. Sun, and X. Liu (2016). A high-resolution model of linear trend in mass variations from DMT-2: added value of accounting for coloured noise in GRACE data. *Journal of Geodynamics*
5. **O. Didova**, B. C. Gunter, R. E. M. Riva, and R. Klees. Unprecedented high spatial resolution of the derived GIA and ice mass changes in Antarctica using GRACE, ICESat, RACMO, and GPS data (in prep.)